1-1-1980

Electron microscopy and x-ray diffraction studies of high modulus solid state extruded polyethylene.

Edward S. Sherman
University of Massachusetts Amherst

ELECTRON MICROSCOPY AND X-RAY DIFFRACTION STUDIES OF HIGH MODULUS SOLID STATE EXTRUDED POLYETHYLENE

A Dissertation Presented

By

EDWARD S. SHERMAN

Submitted to the Graduate School of the
University of Massachusetts in partial fulfillment
of the requirements for the degree of

DOCTOR OF PHILOSOPHY

September 1980

Polymer Science and Engineering

ELECTRON MICROSCOPY AND X-RAY DIFFRACTION STUDIES OF HIGH MODULUS SOLID STATE EXTRUDED POLYETHYLENE

A Dissertation Presented

By

Edward S. Sherman

Approved as to style and content by:

Roger S. Porter, Co-Chairperson of Committee

Edwin L. Thomas, Co-Chairperson of Committee

Richard S. Stein, Member

William J. MacKnight,
Department Head
Department of Polymer Science
and Engineering

ACKNOWLEDGMENTS

I wish to acknowledge the assistance, advice and challenges posed by my co-advisors, Professors Roger S. Porter and Edwin L. Thomas. I also wish to thank Professor Richard S. Stein for serving on my committee and for his thoughtful advice and criticism.

I gratefully acknowledge the useful discussions and experimental assistance of Drs. R.W. Hendricks, J.S. Lin and G.D. Wignall of Oak Ridge National Laboratories, Solid state Division, in obtaining the small-angle x-ray scattering results.

I wish to thank Drs. T. Kanamoto, M.P.C. Watts and A.E. Zachariades for the preparation and mechanical testing of the extruded samples.

The assistance of Mr. Gary Price at the University of Dayton Research Institute, in obtaining quantitative microdensitometry of wide angle x-ray film patterns, and of Ms. Carolyn Peschek at the University of Minnesota for the wide angle x-ray diffraction line broadening studies is gratefully acknowledged.

ABSTRACT

Electron Microscopy and X-Ray Diffraction
Studies of High Modulus Solid State
Extruded Polyethylene

(September 1980)

Edward S. Sherman, B.S., Northwestern University
M.S., Ph.D., University of Massachusetts
Directed by: Professors Roger S. Porter
and Edwin L. Thomas

The structure of high-modulus, solid-state-extruded polyethylene (PE) and conventionally drawn PE were studied by conventional and scanning transmission electron microscopy (STEM), wide and small angle x-ray scattering (SAXS) to determine how the morphology and properties change with processing conditions and the role of annealing during the extrusion process.

Electron microscopy techniques were developed for examining the structure of these fibrous samples and other semicrystalline polymer morphologies. STEM has been suggested to have advantages over conventional transmission electron microscopy (CTEM) for the observation of diffraction contrast features and diffraction patterns from radiation sensitive crystalline polymers. For many

applications it is desirable to obtain successive diffraction patterns from very small adjacent areas. The most useful technique is scanning microarea diffraction used in conjunction with dark field (DF) imaging. Using this technique we have obtained diffraction patterns from regions as small as 1000 Å x 1000 Å for a 120 Å thick PE crystal. Adjacent microarea diffraction patterns can be obtained while only radiation damaging the diffraction region. This allows mapping of the specimen crystallography on a very fine scale as well as allowing one to obtain a diffraction pattern for selecting various STEM DF conditions while only damaging a small portion of the specimen before the DF image is recorded. A STEM annular DF detector is used to form images of crystals with more than one reflection resulting in increased DF image intensity and resolution. Annular DF with a single powder ring is very suitable for studying the rotation and orientation of lamellae during deformation.

SAXS experiments were performed at Oak Ridge National Laboratories using the 10-meter instrument with pin-hole collimation and a two dimensional position sensitive detector.

Two solid state extrudates of different molecular weight PE resulted in different extrusion rates and tensile moduli when extruded at 120°C to extrusion draw ratio

(EDR) 24. Both samples had a microfibriller morphology where the microfibrils consisted of alternating crystalline and non-crystalline regions. The higher molecular weight sample, which extruded slower, had a tail of long crystals (6% over 500 Å long and up to 3,800 Å) and a smaller SAXS invariant which correlated with its higher tensile modulus (46 vs. 27 GPa).

Samples extruded to draw ratios of 12, 24 and 36 X showed an increase in crystal length with increasing EDR with the development of a tail of long crystals at EDR 36. The SAXS peak meridional breadth increased with EDR indicating that the microfibrils become thinner during drawing. The SAXS invariant and density difference between the crystalline and non-crystalline regions decreases with EDR as more oriented and tightly packed tie molecules are produced increasing the tensile modulus.

Solid state extruded, hot drawn, cold drawn and cold drawn and annealed samples of draw ratio 9 were compared to determine the role of annealing during processing. The crystal length and long period are a function of processing or annealing temperature. Annealing the cold drawn sample with fixed ends made the taut tie molecules stable to thermal shrinkage as for the solid state extruded sample without decreasing the tensile modulus. For this group

of 9 X drawn samples the solid state extruded sample had the smallest density difference between the crystalline and non-crystalline regions.

TABLE OF CONTENTS

LIST OF TABLES

LIST OF FIGURES

FORWARD

Introduction

The use of deformation to improve the properties of polymeric materials is an old technique. The realization that polymers could be deformed to form strong fibers dates from the early part of this century: the first commercial use being the introduction of Nylon 66 by the duPont Company.

Oriented fibrous polyethylene (PE) has been produced by numerous methods that give a product with a wide range of mechanical properties. These methods can be grouped as cold drawing, hot drawing, crystallization from flowing solutions, melt extrusion, and hydrostatic and solid state extrusion. The fibrous products of all these techniques have a considerably higher tensile modulus than unoriented PE.

Thesis Problem

A goal of research in high modulus fibers is to optimize processing conditions to produce the highest tensile modulus and strength both quickly and inexpensively.

This material would approach an idealized morphology where every molecule is fully extended and uniaxially aligned. Such an achievement would require an understanding of how deformation processes affect properties. This understanding can only come from a detailed knowledge of morphology and how it affects physical properties.

The goal of this thesis is to determine the morphology of high modulus polyethylene produced by solid state extrusion. We address the question of how the morphology and properties change with processing conditions and the role of annealing during the extrusion process. Results on solid state extruded fibers are compared with several conventionally drawn fibers.

Thesis Organization

Chapter I is a review of the various deformation techniques that have been used to transform unoriented solid polyethylene into high tensile modulus fibers. The emphasis of this chapter is on the type of fiber morphology associated with cold drawing, hot drawing and hydrostatic and solid state extrusion, and how different fiber structures formed from the various processing conditions affect resulting fiber mechanical properties.

Chapter II is a description of the experimental techniques used in this study.

Chapter III is about the application of the relatively new technique of scanning transmission electron microscopy (STEM) to the morphology of semicrystalline polymers. Meaningful achievements in understanding the structure of materials always requires the best and most recent experimental techniques. The microscopy techniques that were developed in this portion of my thesis work were later applied towards obtaining the most detailed information about the structure of the solid state extruded fibers in Chapters IV, V, and VI.

Chapter IV is a comparison of the morphologies of two samples of the highest modulus that can be obtained reproducibly by solid state extrusion in this laboratory. These two samples were produced by nearly identical processing conditions but differ in molecular weight of the starting polymer.

Chapter V is a study of the morphological changes that occur with increasing draw ratio. Since the tensile modulus increases proportionately with draw ratio, changes in morphology should correlate with the source of the high modulus for these fibers. This chapter also investigates the deformation mechanism(s) of polyethylene during the solid state extrusion process. Previous work in this area has concentrated on conventional fiber drawing where sample necking occurs.

Chapter VI is a comparison of cold drawing and solid state extrusion. In this chapter the question of whether solid state extrusion can be viewed as the combination of cold drawing with annealing affects is addressed. This involves a study of basically four types of samples of the same draw ratio (9X): 1) solid state extruded at 120°C, 2) cold drawn (i.e., room temperature), 3) cold drawn and annealed with free ends at 120°C and 4) cold drawn and annealed at 120°C with fixed ends.

Chapter VII is a summary of conclusions and contains suggestions for extensions of this work.

Appendices I and II are the computer program for calculating the SAXS invariant and a calculation of sample residence time in the extrusion die. Appendix III is an estimation of the void content in these samples.

C H A P T E R I

LITERATURE REVIEW

1.1. Introduction

In this chapter relevant literature on the solid state deformation of polyethylene (PE) to a fibrous morphology is reviewed. The processes of cold drawing, hot drawing, solid state and hydrostatic extrusion are discussed with particular emphasis on the structures and resultant properties obtained during deformation.

1.2. Cold Drawing

Cold drawing refers to the tensile deformation performed at ambient temperature where annealing does not influence the drawing behavior. When tensile bars of PE, having an initially spherulitic morphology, are cold drawn a macroscopic neck usually forms. The neck propagates consuming untransformed material. The transformed material continues to draw slightly since it is still plastically deformable.

The structure of cold drawn PE fibers has been investigated primarily by electron microscopy, wide and

small angle x-ray scattering. Transmission electron microscopy of surface replicas of drawn films showed long thin fibrils oriented in the tensile direction (1). The smallest units of these fibrils are termed microfibrils and are typically 200 to 300 Å in width. Dark field microscopy and selected area electron diffraction showed that the polymer chains are oriented in the fiber direction and that there are small crystallite blocks aligned along the microfibers (2). Cold drawn PE fibers show a small angle scattering maximum (3). Peterlin and Meinel found a 4 point pattern within the necked zone. When the material is completely transformed to fiber a two point pattern is obtained. Wide angle x-ray diffraction indicates that the c-axis (chain axis in PE) orientation increases with increasing draw.

Similar microfibrils have been observed by electron microscopy (4) when dilute solution grown PE single crystals were deformed on Mylar® substrates. These observations have led to the model shown in Figure 1 for the deformation of spherulitic PE to form a fibrous structure (5). The transformation shown in Figure 1 has the following stages:

1. The lamellar crystals slip past each other. Most of the strain is in the amorphous regions and is anisotropic due to the spherical

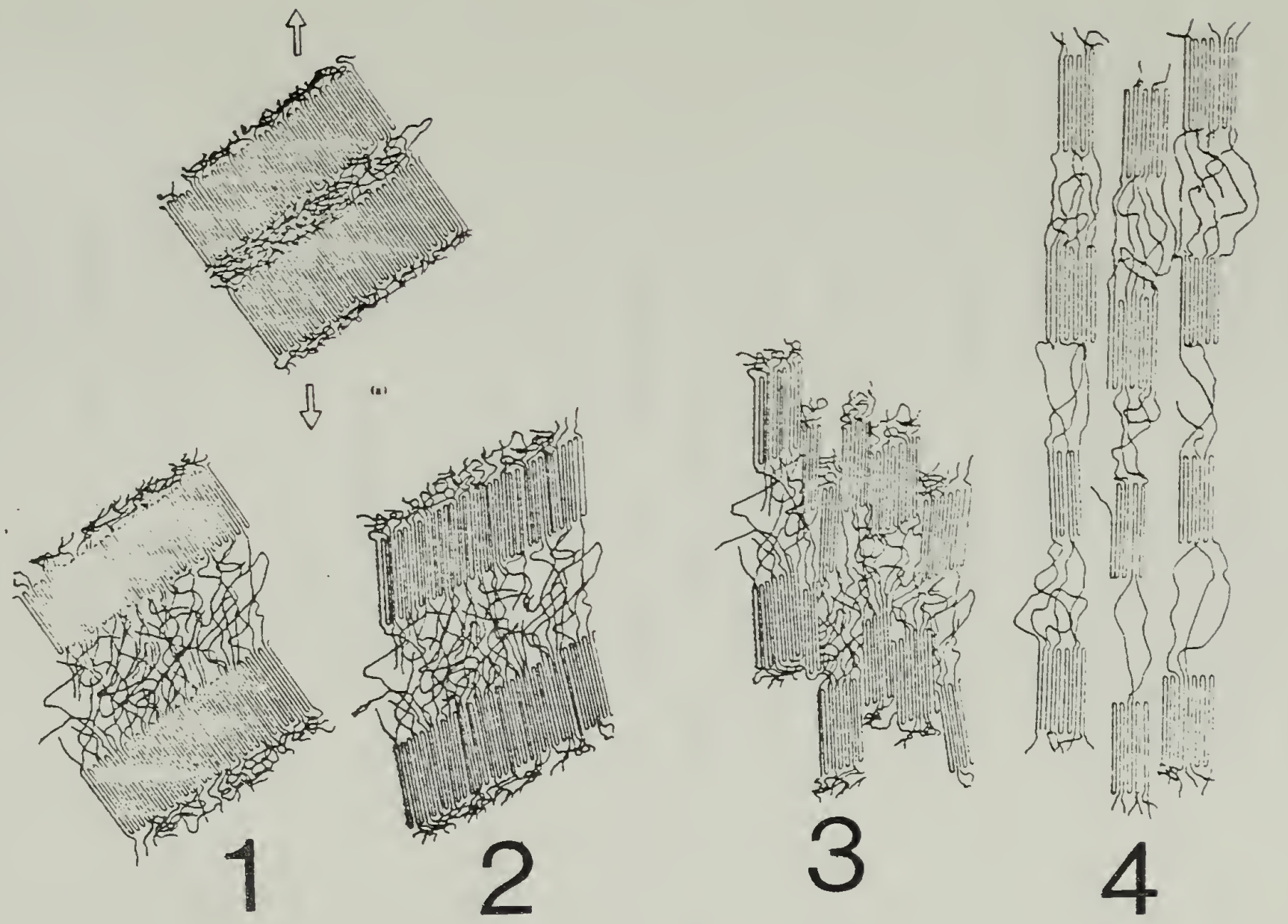

Figure 1.1. Stages in the lamellar deformation mechanism (Reference 4).

symmetry of the lamellae in spherulites.

2. The tie chains which connect adjacent crystals become highly extended and the lamellar crystals deform plastically by slip-tilt mechanisms. These deformations have been reviewed in detail by Bowden and Young (6).
3. Blocks of small crystals are pulled out of the lamellar crystals. These crystal blocks are connected by various types of tie chains. This occurs at different positions of the elongated spherulite in what are called micronecking zones. The details of this stage of the deformation process are at present not completely understood. Two recent publications by Tarin and Thomas have investigated the role of the inter and intralinks between lamellae in initiating the transformation (7) and microfibril deformation (8).
4. The crystalline blocks become aligned along the tensile axis and discrete microfibers are formed.

Steps 2 through 4 occur over a distance as small as 1000 Å in the micronecking zones. The microscopic draw ratio in the macroscopic neck varies greatly from point to point since the deformation of spherulitic structure is

extremely inhomogenous.

Figure 2 is Peterlin's model for the structure of the microfibers formed during cold drawing. The alternating crystalline and non-crystalline regions account for the small angle 2-point x-ray pattern and the crystal blocks observed alternating along the fiber by dark field (DF) transmission electron microscopy (9). The microfibers are roughly 200 Å wide and 15 to 20 μm long. The modulus depends on the amount of axial interconnections, tie molecules, crossing the non-crystalline regions to connect adjacent crystallites. It has been proposed that the modulus depends solely on the number of the taut (e.g. load bearing) tie molecules (TTM). Takayanagi (10) proposed the following equation for the relationship between the volume fraction of TTM's in the non-crystalline layer, β, and the sample modulus, E, when the load is uniformly distributed over the cross section and the strain in the non-crystalline layer is the same for TTM's and amorphous material:

$$E = E_c \frac{\beta+(1-\beta)E_a/E_c}{1-(D/L)(1-\beta)(1-E_a/E_c)} \qquad (1.1)$$

where E_a and E_c are axial elastic moduli of amorphous and crystalline components respectively. D and L-D are the

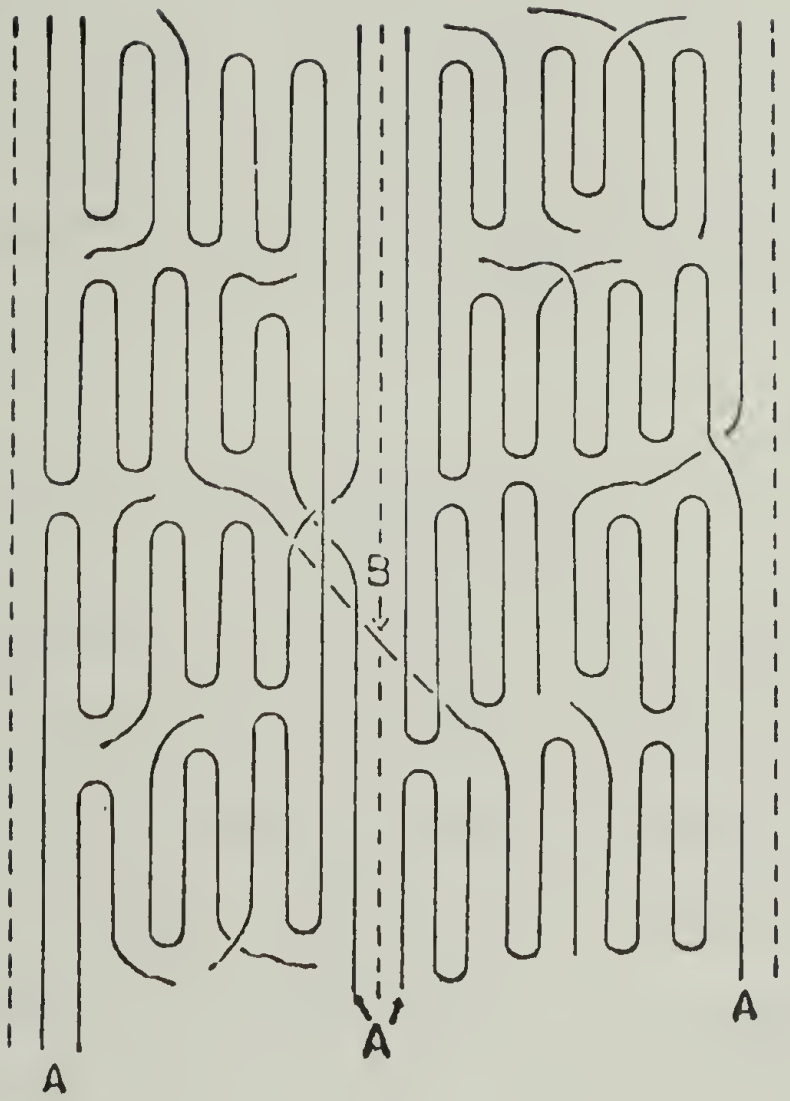

Figure 1.2. Peterlin's microfibrillar model of the fibrous structure with a great many intrafibrillar (A) and a few interfibrillar (B) tie molecules (Reference 5).

thickness of crystal block and non-crystalline layer respectively. This model predicts a β of about 1% for a typical modulus of 15GPa for a cold drawn sample when L = 250 Å, D = 200 Å, E_c = 320 GPa (11) and E_a = 0.5 GPa (12). If the TTM's are located on the outer surface of the microfibril, then the following equation is applicable (13):

$$E = E_c\left(\beta + \frac{1-\beta}{1+(D/L)(E_c/E_a-1)}\right) \qquad (1.2)$$

This limiting case in which only the edges of the crystal might bear any load still gives a moderately small β of only 4.5% using the previously stated parameters. A recent study using finite element analysis (14) has shown that the effective modulus of such interlinks as TTM's may be only 25 to 70 percent of E_c due to ineffective stress transmission.

The most convincing (but indirect) evidence for TTM's is the large shrinkage of cold drawn fibers when they are annealed with free ends. If the annealing temperature, T_a, is sufficiently high, the TTM's exert retractive forces of entropic origin on the crystal blocks they are anchored in. This causes a macroscopic sample shrinkage (15) of up to 97% depending on T_a and a partial retransformation to the initial sample morphology (16,17) with a concurrent drop in

tensile modulus (11). The decrease in modulus is probably due to the relaxation of the TTM's and the change from the microfibrillar to a more lamellar morphology.

1.3. Hot Drawing

Hot drawing covers the range of drawing temperature where annealing has substantial affects. Thus for polyethylene the transition in temperature between hot and cold drawing is gradual and occurs between 75 and 100°C. This temperature range is associated with the crystalline dispersion temperature, α_c, or alpha transition. At temperatures much higher than α_c polymers deform easily but the c-axis orientation is poor and the modulus reduced (18).

Several research groups have established that the tensile modulus of hot drawn PE is a linear function of draw ratio (19, 20, 21). A plot of the collected data of several groups is shown in Figure 3. Cold drawn PE also shows the same linear increase of tensile modulus with draw ratio. However, hot drawing allows higher draw ratio to be achieved with correspondingly higher tensile moduli (approximately 30X to obtain a 70 GPa tensile modulus). Barham and Keller (19) showed that the initial sample morphology plays a large role in obtaining high draw ratios.

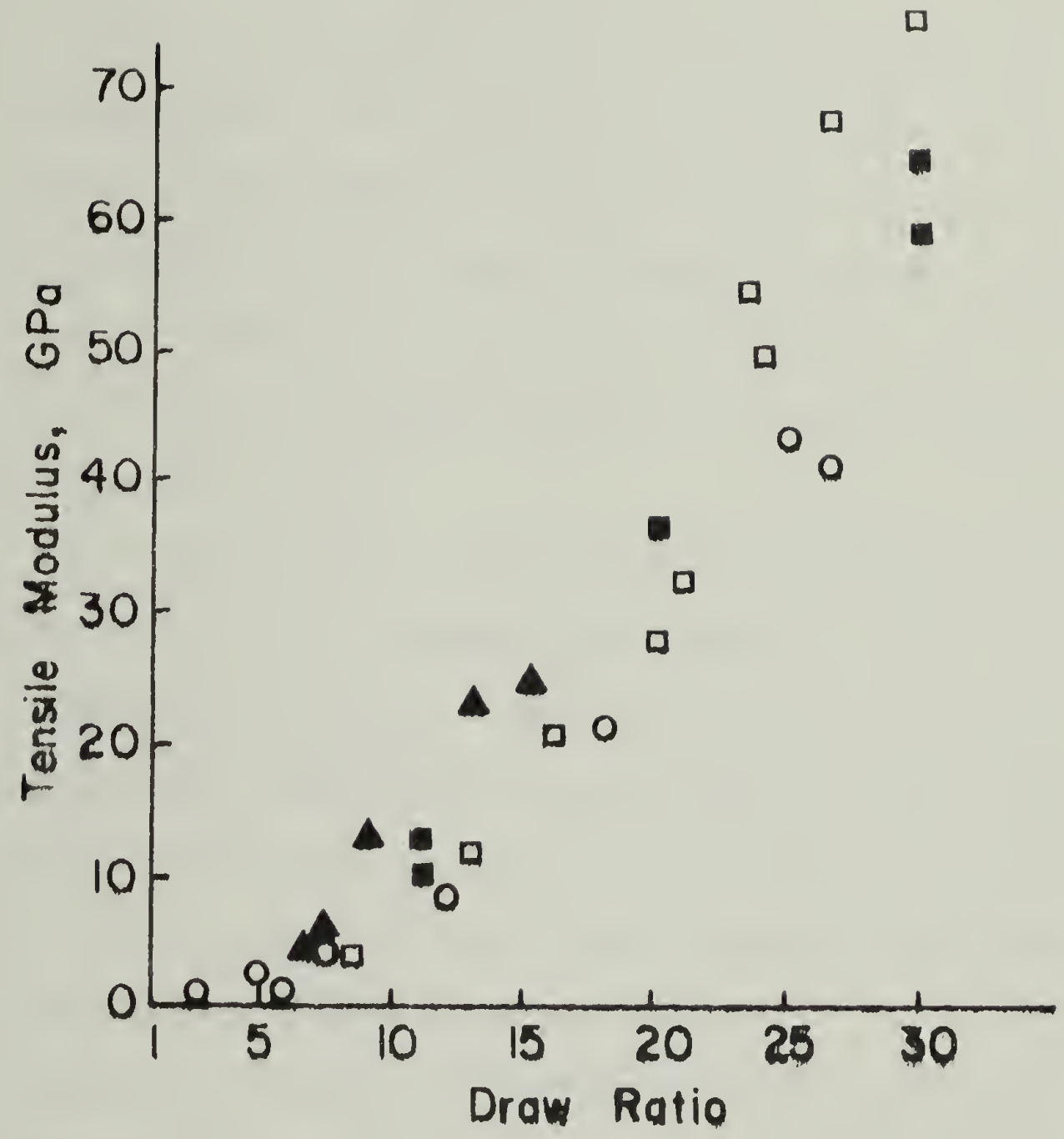

Figure 1.3. Tensile modulus of hot drawn polyethylene as a function of draw ratio from the data of: (□) Barham and Keller (19), (▲) Andrews and Ward (20), (■) Capaccio and Ward (21) and (O) Wu, Simpson and Black (43).

Using broad molecular weight distribution samples they obtained the highest draw ratios with slow cooling rates where the very low molecular weight material segregated between spherulites. The segregation of low molecular weight material was found to be a prerequisite for obtaining the highest draw ratios. Capaccio and Ward (21) found that low molecular weight (M_w = 67,800 and M_n = 13,300) and quenched samples yielded the highest draw ratio, 36X, when drawn at 75°C.

Meier and Jarecki (22) studied the effect of drawing temperature on the formation of internal voids over a range of molecular weights. They found that increasing draw temperatures decreased the draw ratio at which both longitudinal separation at fibrils and perpendicular cracks occurred. This allowed higher draw ratios to be reached before the sample failed during drawing.

Capaccio and Ward have suggested 120°C as the optimum drawing temperature for PE (21). Samples drawn above this temperature achieved higher draw ratios but the tensile modulus dropped below the maximum (43 GPa) achieved at 120°C. Drawing above 120°C resulted in a higher draw ratio but lower modulus since more relaxation is occurring than molecular extension.

Ward, Clement and Jakeways have used small angle and

wide angle x-ray scattering to study the structure of quenched PE films drawn at 75°C (23). They found that the small angle long period remained relatively constant (circa 200 Å) over a range of draw ratios from 5.2 to 30X while the crystal coherence length in the chain direction (measured by applying the Scherrer equation to the width of the 002 reflection) increased from 230 Å to 465 Å. They interpreted this data to support a crystalline bridge model shown in Figure 4. A problem with this approach is that each scattering technique measures a different moment of the distribution of crystalline lengths in the fiber and the observed difference in the crystal size may be due to either intercrystalline bridges or a broad distribution of crystal sizes.

A recent study by the same group using dark field transmission electron microscopy to directly image the crystallites shows that the crystal length distribution broadens considerably with increasing draw ratio for samples drawn at 120°C (24).

Arridge, Barham and Keller studied how annealing changed the properties of PE drawn at 75°C (25). Annealing the initially formed fibers with constrained ends dropped the tensile modulus to 14% of its original value (65 GPa). However, after aging at room temperature (1000 min.) the

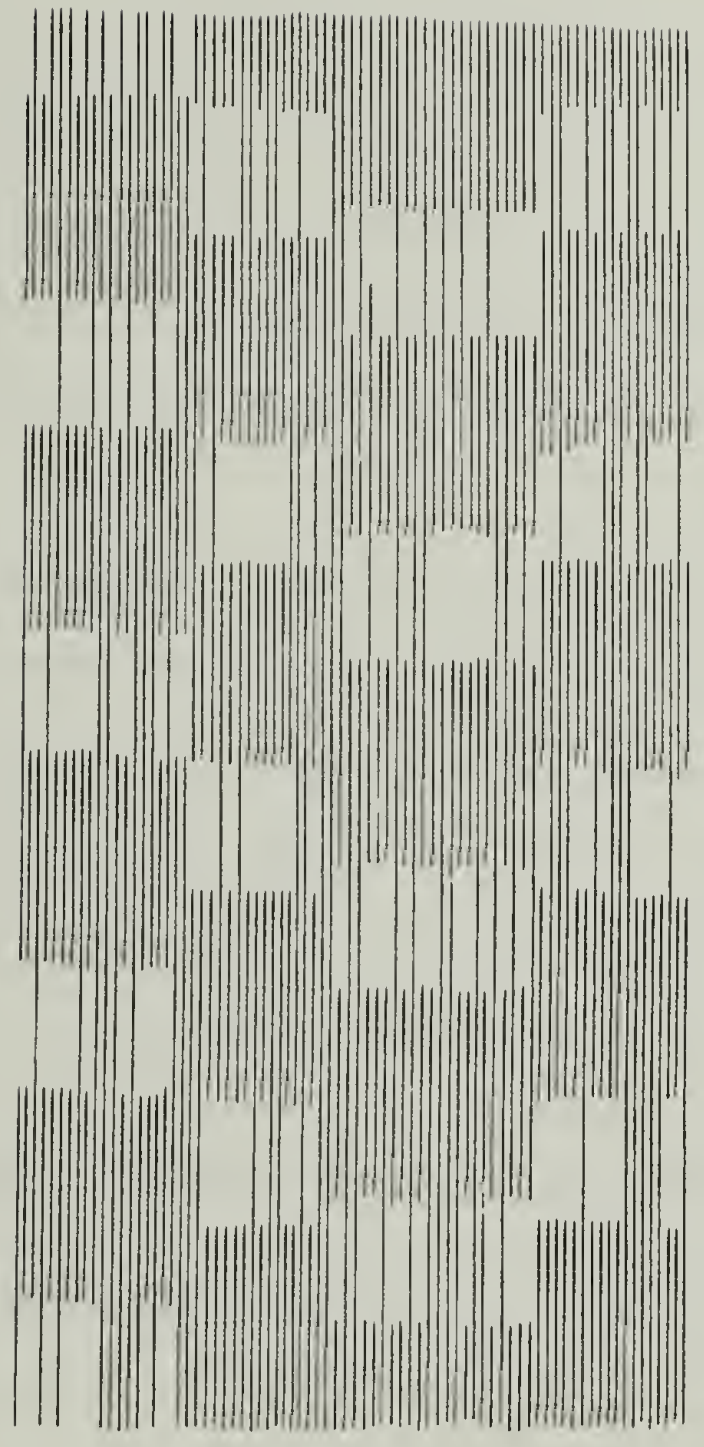

Figure 1.4. Crystalline bridge model for the microfibrils in hot drawn polyethylene (References 23 and 26).

tensile modulus (remarkably!) increases to 70% of its initial value. This interesting effect was later studied by Ward and coworkers using wide and small angle x-ray scattering (26). They found a similar self-hardening behavior as Arridge et al with the crystal coherence length in the chain direction increasing with storage time after annealing, correlating with the increase in tensile modulus.

This study supports the crystalline bridge model since the crystallization of taut tie molecules to crystalline bridges caused by annealing would increase both the tensile modulus by providing new or more effective "tie molecules" and the crystal coherence length by increasing the number of crystal blocks in registry.

1.4. Solid State and Hydrostatic Extrusion

In solid state and hydrostatic extrusion a cylinder of polymer is forced by pressure to flow through a converging conical die. The term "solid state extrusion" is used when the force is applied to the solid polymer via a ram. In hydrostatic extrusion a high pressure fluid exerts the force and is extruded as a thin film between the polymer extrudate and the die, hence lubricating the extrudate. Figure 5 shows a typical die geometry. The extrusion draw

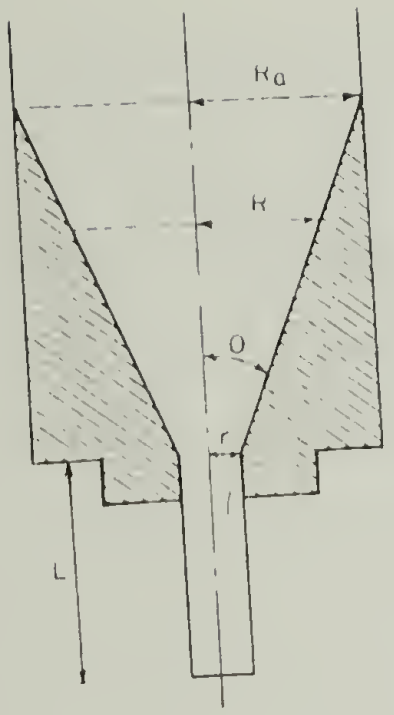

MAXIMUM EXTRUSION DRAW RATIO

$$DR_M = \left(\frac{R_a}{r}\right)^2$$

CONICAL DIE, $DR(R) < DR_M$

$$DR(R) = \left(\frac{R_a}{R}\right)^2 = \left(1 - \frac{3r^2 L \tan\theta}{R_a^3}\right)^{-2/3}$$

$$= \left[1 - \frac{(DR(r)^{3/2} - 1)}{DR_M^{3/2}}\right]^{-2/3}$$

FIBRE, $DR(r) \leq DR_M$

$$DR(r) = \left(\frac{R}{r}\right)^2 = \left(1 + \frac{3L \tan\theta}{r}\right)^{2/3}$$

Figure 1.5. Solid state extrusion die geometry and extrusion draw ratio variation (Reference 35).

ratio (EDR) of the extrudate is determined by the ratio of entrance and exit areas of the die:

$$EDR = \left(\frac{R_a}{r}\right)^2 \qquad (1.3)$$

Therefore, the draw ratio is not limited by the necking process as in tensile drawing experiments. Fibrillation and voiding during deformation are suppressed by the compressive forces of the die. This allows higher draw ratios (up to 45X for PE [27]) to be obtained than are possible by conventional hot or cold drawing.

The polymer is deformed under elongational flow as in drawing but with an additional shear flow component (28). Extruded samples have a different strain rate history as a function of EDR than drawn samples (29,30). In drawing most of the deformation occurs in the neck. This behavior is shown schematically in Figure 6a.

However, with extrusion through a conical die the strain rate is highest at the die exit where the extrusion draw ratio is at its maximum. The strain rate varies inversely as the cube of the distance from the die exit as shown in Figure 6b.

Imada et al (31) performed the first study on solid state extrusion and the properties of PE extrudate. They

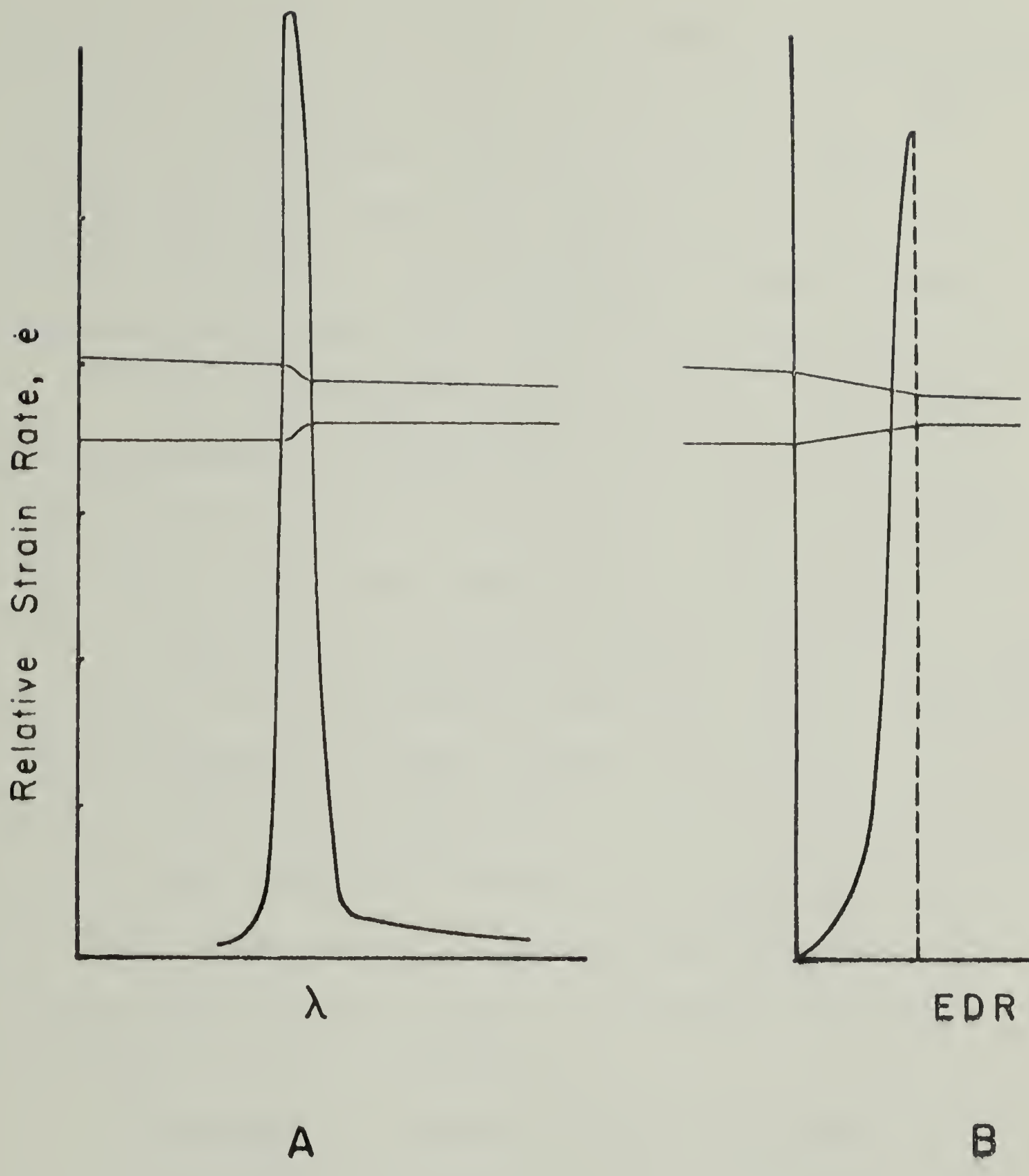

Figure 1.6 Relative strain rate vs. draw ratio for; (a) drawing (b) extrusion. The shape of the sample is superimposed on the figure. In drawing the draw ratio increases after the maximum strain rate is reached in the neck while for extrusion through a conical die the maximum is at the die exit where the final EDR is reached (References 29 and 30).

extruded PE up to draw ratio of 16X at 100°C. This extrudate had a room temperature tensile modulus of 30 GPa. Wide angle x-ray diffraction indicated an almost perfect orientation of the crystalline chains (c-axis) in the extrusion direction. Preferential orientation of the a-axis parallel to the radial direction was also found.

A two point small angle pattern was found using slit collimation and photographic film. The small angle long period was found to increase with increasing annealing temperature as has been reported for drawn samples.

Transmission electron microscopy showed microfibers 300 Å wide. The 16X extrusion draw ratio sample showed a very high degree of thermal dimensional stability on heating. Shrinkage started only 10 to 15°C from the sample melting point (Tm~133°C) and the final shrinkage was only 2%. This thermal stability compared very favorably with a sample drawn at 80°C to 10X. It started to shrink at ~50°C and shrank ~7% before melting.

Nakayama and Kanetsuna (32,33) extensively studied the morphology and properties of hydrostatically extruded PE. They studied the deformation that occurred within the conical die up to draw ratio 9X. Small and wide angle x-ray patterns recorded as a function of position (hence EDR) down the flow line of the die showed the same lamellae tilt and

slip deformation mechanism as in conventional tensile drawing (3). The c-axis orientation function (f_c) was measured by wide angle x-ray diffraction as a function of extrusion temperature for EDR's of 3, 6.4 and 9. For the highest draw ratio f_c was independent of extrusion temperature. For the lower draw ratios (3 and 6.4) it increased slightly with increasing extrusion temperature. Amorphous orientation (f_{am}) was calculated by measuring the sample birefringence, Δn_t, and using the well known Hermans-Stein equation (34):

$$\Delta n_t = \Delta n_c X_c + \Delta n_{am}(1-X_c) \qquad (1.4)$$

where $\Delta n_c = \Delta n_c^{\circ} f_c$

and $\Delta n_{am} = \Delta n_{am}^{\circ} f_{am}$

Assuming $\Delta n_c = \Delta n_{am}$ and neglecting form and distortional birefringence f_{am} increased with extrusion draw ratio reaching approximately 0.8 between 3 to 8X. f_{am} decreased with increasing extrusion temperature. However, this method of measuring amorphous orientation has a high error for well oriented, highly crystalline specimens since it involves subtracting two terms close in value, Δn_t and $\Delta n_c X_c$. The decreases in amorphous orientation with increasing temperature represents the entropic retraction of taut tie molecules during the solid state deformation.

Solid state extrusion to achieve the highest molecular extension has been pursued extensively in this laboratory. This work has recently been summarized in reference 35. Extrusion draw ratios of up to 40 have been obtained resulting in tensile moduli of about 60 to 65 GPa. Figure 7 shows a plot of tensile modulus as a function of extrusion draw ratio. Tensile modulus seems to be a monotonic function of draw ratio just as in hot and cold drawing.

If the extrusion process can achieve the ultimate goal of ultra-drawing each polymer molecule an ideal continuous crystal morphology would be produced where every molecule is fully extended. This ideal morphology is shown in Figure 8 (36). Chain ends and random chain folds act as defects in this model.

Assuming PE of molecular weight 200,000 and initial lamellae fold period 200 Å a molecular draw of about 80X is required to completely unfold the polymer molecular from its conformation in the lamellae crystal. This idealized morphology should have a tensile modulus close to 320 GPa., the theoretical modulus of PE (11).

A method of experimentally measuring the molecular draw ratio has recently been developed (37). By rapidly melting thin films at 160°C and observing shrinkage all the

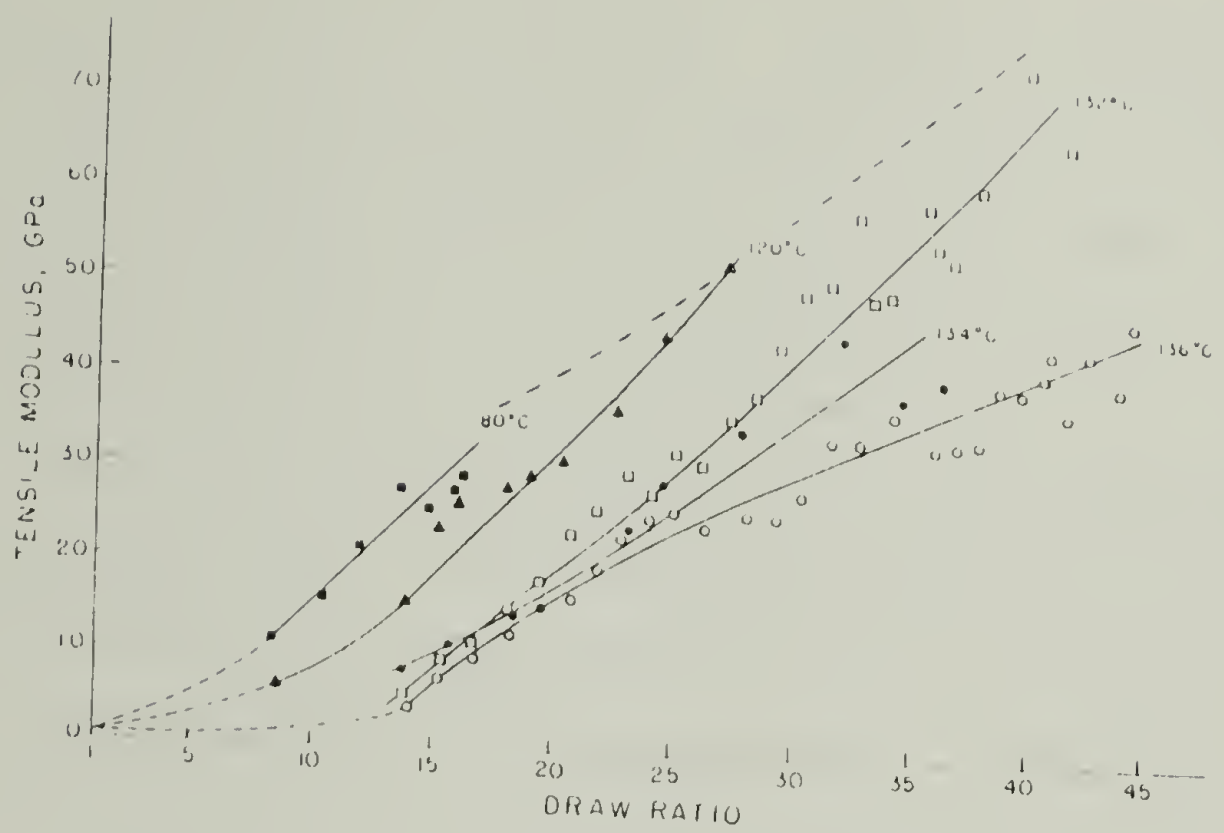

Figure 1.7. Tensile modulus as a function of extrusion draw ratio for various extrusion temperatures (Reference 35).

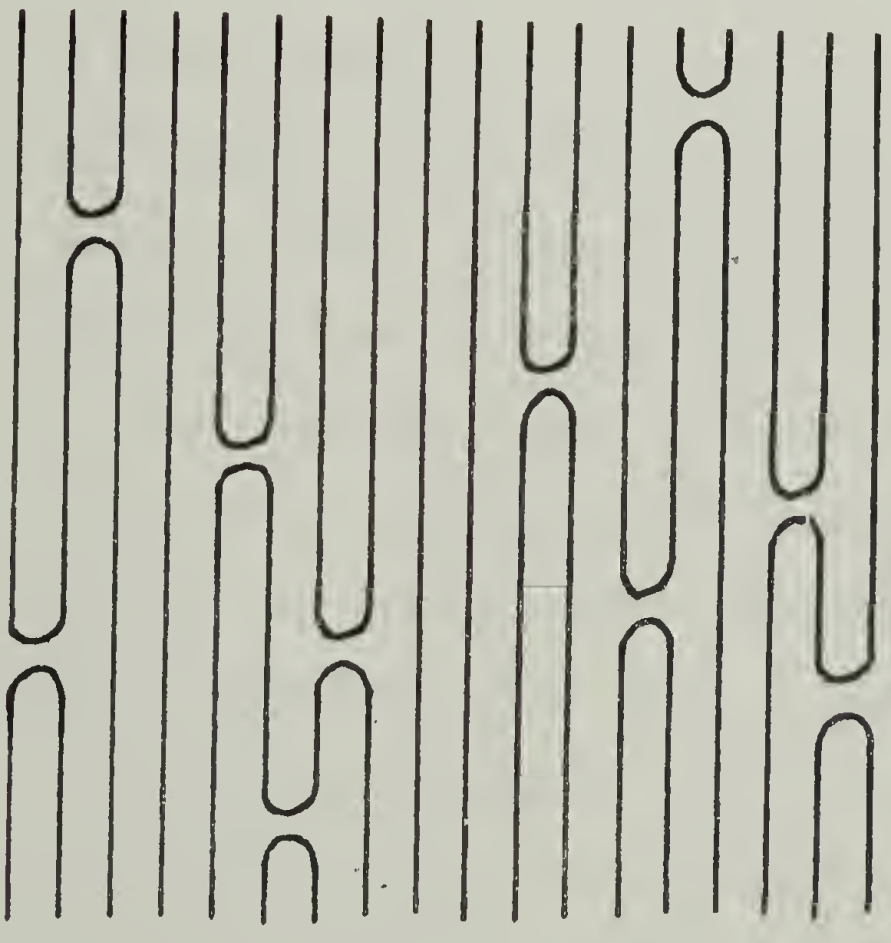

Figure 1.8. Clark's idealized continuous crystal model (36).

molecular extension is recovered. Samples of different tensile modulus but equivalent sample extrusion draw ratio, which were produced from different molecular weight PE's and extrusion conditions, fell on a master curve of tensile modulus versus molecular draw ratio.

Several indirect methods such as gel permeation chromatography (GPC) (38) and thermal expansion (32,40) indicate some "continuous crystal" structure present in this class of samples of high extrusion draw ratio. GPC was performed on samples etched at 60°C in red fuming nitric acid for several weeks. Since nitric acid preferentially degrades amorphous PE chains, a GPC analysis of the remaining polymer yields the chain length distribution in the remaining crystallites. A high molecular weight tail that remained after 14 weeks of etching was attributed to approximately 20% continuous crystal phase. Since these fibers are very resistant to degradation the high molecular tail could be a combination of long crystals and/or undegraded tie molecules. Thermal expansion coefficients were measured on solid state extrudates of draw ratio 50 prepared at 136°C under an extrusion pressure of 2100 atm. A negative thermal expansion coefficient was measured (i.e., reversible shrinkage on heating). Since the thermal expansion of PE crystals is negative in the chain direction, this suggests "crystal

continuity" exists throughout the macroscopic sample. The thermal expansion data was later combined with tensile properties to calculate the area fraction of the continuous crystal phase using a series-parallel model (40). This model did not include the presence of taut tie molecules in the non-crystalline regions. The non-crystalline regions were also assumed to be completely amorphous with a positive thermal expansion coefficient. If a theoretical tensile modulus of 320 GPa (11) is used for the crystallites and tie molecules the equations in reference 37 yield an area fraction of the continuous load bearing crystals of 13%.

Solid state extruded PE, cold and hot drawn samples all exhibit x-ray scattering maxima at small angles. All these fibers show a 2-point pattern of intensity peaks on the meridian, caused by periodic electron density fluctuations along the microfiber corresponding to the crystalline and non-crystalline regions. The long period has been found to increase with extrusion temperature at the constant extrusion draw ratio of 10 (35). This corresponds with the work of Peterlin on hot drawing which he interpreted as annealing to a new fold period (41). A large decrease in the SAXS peak intensity is also reported for solid state extrudates produced at 134°C and 2,300 atm. as the extrusion draw ratio increases from 5 to 40. This was

interpreted as being caused by an increase in fiber perfection as the fold concentration decreased and became distributed throughout the fiber as local defects.

Small angle diffraction peaks can weaken in intensity for 4 reasons: increasing macrolattice distortion, decreasing macrolattice size, decrease in the density difference between the phases, and a change in phase volume fractions. The macrolattice order within the fiber can be studied unambiguously by SAXS only when 3 orders of reflection are observable (42). This is unfortunately almost never the case in polymeric systems. Wu, Simpson and Black have qualitatively correlated a decrease in scattered intensity with increasing tensile modulus and strength for hot drawn PE fibers (43). The density difference between the phases can be measured by calculating the invariant from the scattering intensity. For oriented samples the calculation should be done over 2 dimensions using point collimated radiation. The invariant analysis has been done only for a few systems, by Crist for oriented PET (44) and Nylon 6 (45). The SAXS intensity decreases with increasing draw for PE (41), which is interpreted as resulting from an increase in the amorphous phase density as the non-crystalline orientation increases with draw.

What is remarkable about these high modulus fibers

that have been reported to contain some continuous crystalline phase is that the initial microfiber structure formed at the low natural draw ratio still remains with further significant drawing. An essential question that remains is if this continuous crystal phase exists where it is in relation to the more conventional microfiber structure and how does it form from it. It is a primary goal of this thesis to resolve these important questions.

C H A P T E R I I

EXPERIMENTAL TECHNIQUES

2.1 Specimens

Drawn and extruded samples were prepared from two commercial linear high density polyethylenes, Alathon® 7050 of DuPont Co. and Marlex®6003 of Phillips Petroleum Co. The molecular weights of these polyethylenes are M_N = 59,000 with M_w/M_N = 3 and M_N = 200,000 with M_w/M_N = 7 to 13 respectively. These polymers will be designated L and H for low and high molecular weight.

Solid state extrusion was performed at 120°C through conical brass dies of 20° entrance angle. Polyethylenes L and H were extruded at 2400 atm pressure to extrusion draw ratio (EDR) 24 using a die of exit diameter 1.8 mm and entrance diameter 8.8 mm. The extrusion rates were 20 mm/min. and 0.6 mm/min. respectively. Sample L was also extruded to draw ratios of 12, 24 and 36 using exit dies of 2.9, 2.0 and 1.8 mm diameter. The extrusion pressure of 2400 atm resulted in extrusion rates of 45, 20 and 1.4 mm/min.

The comparison of solid state extrusion to cold drawing with post-draw annealing was performed using sample H at draw ratio 9. Sheets were hot pressed from pellets at 160°C. The sheets were then quenched in ice water after

being held at the pressing temperature 5 min. without pressure to allow stresses to relax. Strips 5 mm wide were cut from these sheets and drawn in an Instron at 2 mm/min. at room temperature. The draw ratio was measured by the separation of fiducial marks drawn on the undeformed sample at 10 mm intervals. Films of draw ratio 9 were used. These samples will be referred to as cold drawn. Solid state extruded samples of extrusion draw ratio 9 were prepared by coextrusion of the cut strips in a polyethylene "sandwich" (46). The extrusion was performed at 120°C at an extrusion rate of 18 mm/min.

Cold drawn films were annealed in a silicone oil bath at 120°C. Samples were annealed with the ends free and with both ends fixed by clamps to prevent shrinkage during annealing. Annealing was performed for 5 minutes. This corresponds to the total residence time of the solid state extruded sample in the extrusion die as it was deformed from EDR 1 to 9, while the other samples were annealed after drawing to 9X. Samples were also annealed with free ends for the 1 min. during which all the shrinkage occurred. Hot drawn 9X samples were also prepared at 120°C and drawing rate of 2 mm/min.

2.2 Mechanical Testing

The modulus measurements of the extrudates were performed in tension at ambient temperature on an Instron TTM

tensile tester (37). The elastic modulus was determined from the tangent to the stress-strain curve at 0.1% strain. The strain was measured using an extensometer. The strain rate was 3×10^{-5} sec^{-1}.

The modulus measurements of the film samples were performed in tension at ambient temperature on a Toyo table model Instron. The elastic modulus was determined from the tangent to the stress strain curve at 0.1% strain on 30 mm gauge length samples. Machine compliance was accounted for in measuring the strain. The strain rate was 3×10^{-5} sec^{-1}.

2.3 Differential Scanning Calorimetry (DSC)

DSC scans were performed at a heating rate of 10°C/min. using a Perkin-Elmer DSC-2. An indium sample was used to calibrate melting point and heat of fusion. The degree of crystallinity was calculated assuming 68 cal/gm for the heat of fusion of PE crystals (47).

2.4 Density

Sample densities were measured in an ethylene glycol-isopropanol density gradient column by ASTM procedure D1505-68 using glass calibration beads. Measurements were reproducible to .0005 gm/cm^3.

2.5 Shrinkage

Shrinkage measurements were performed on the film

samples of draw ratio 9 in a silicone oil bath between 60° and 136°C. 10 mm strips approximately 2 mm wide and .3 mm thick were submerged in the constant temperature bath for 1 min. then quenched in water and the final length, l_f, was measured. The 1 min. immersion time was chosen since the shrinkage was complete after this time for all samples. The percent shrinkage, S, was calculated as:

$$S = \frac{\ell_o - \ell_f}{\ell_o} \times 100 \qquad (2.1)$$

where ℓ_o is the initial length of the strip.

2.6.1 Sample preparation for electron microscopy. Thin specimens for transmission electron microscopy (TEM) were obtained by two independent methods. Detachment replication (48,49) required freeze-fracturing the sample longitudinally at liquid nitrogen temperature to expose the interior morphology (see Figure 1). This internal fracture surface was then carbon-platinum shadowed at 30° followed by carbon at 90°. Polyacrylic acid (PAA) solution was then painted on the surface, allowed to dry and then stripped off detaching the C-Pt/C replica and most importantly, thin polymer fibrils which adhere well to the replica. The replica was then cut into small pieces and thoroughly washed in distilled water to remove the PAA and then mounted on grids for microscopy.

The second method involved etching the extruded sample in red nitric acid (50,51) for two weeks at 70°C.

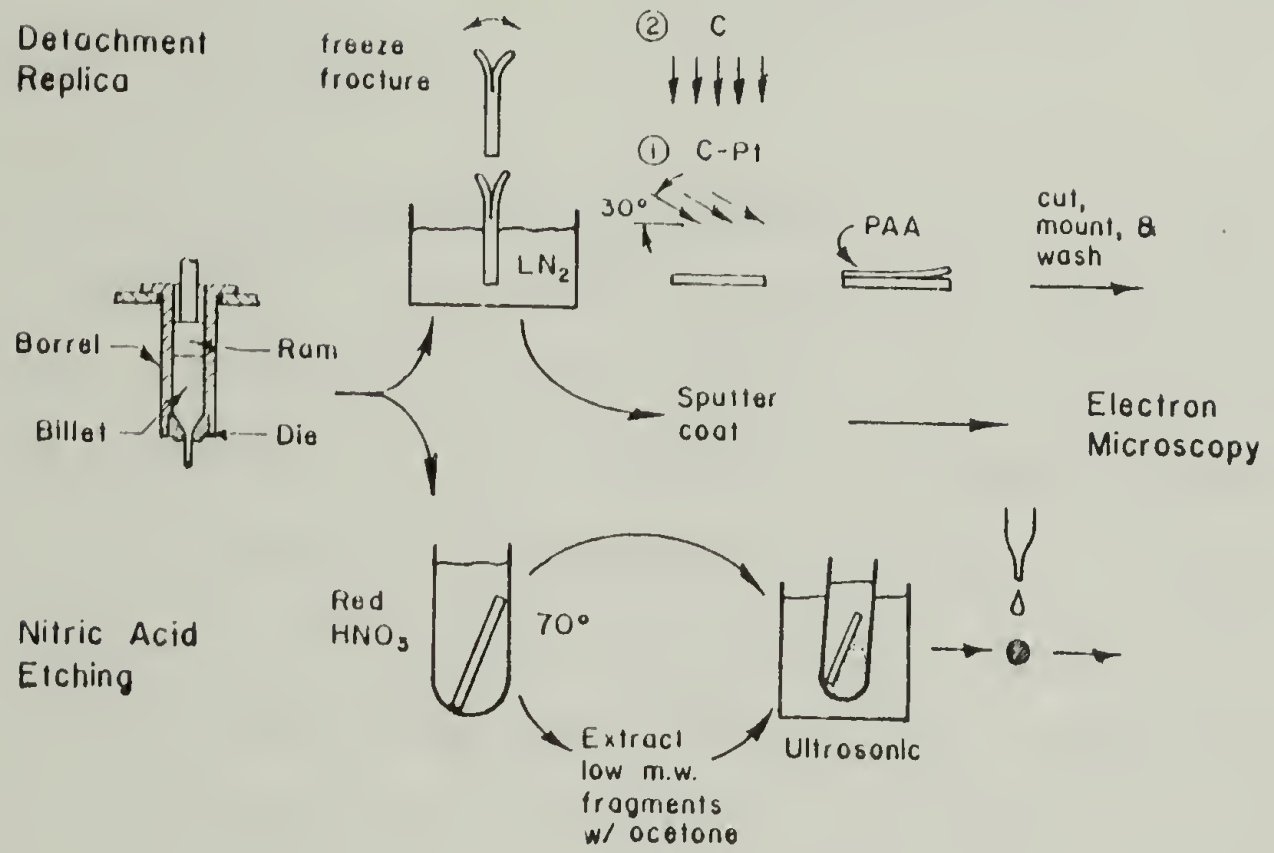

Figure 2.1. Schematic showing the detachment replication and nitric acid etching specimen preparation procedures.

The samples were then washed with water, and low molecular weight fragments were removed by extraction with hot acetone vapors. Fibrous etch fragments were dispersed by mild ultrasonication in ethanol. The suspension of fragments was then simply allowed to dry on a carbon support film mounted on a TEM grid.

2.6.2 Electron microscopy techniques. Electron beam radiation damage to our samples limits the obtainable information. Ionization events caused by the incident electrons create free radicals and their subsequent reactions cause the polyethylene molecules to crosslink and degrade. These changes in molecular structure lead to loss of crystallinity and dimensional changes (52). Because we operate the microscope in conditions of low electron flux on the sample and detached fibers generally have good thermal contact with the substrate, beam heating effects are minor. Since the diffracted intensity used to form the DF image decreases as the crystal is transformed to the amorphous state only the diffracted intensity up to the crystal life time, τ, (which is a function of the radiation chemistry and physics of the polymer) is available to form a useful image. This limits the resolution of DF images. Also, it is known that for PE single crystals damage occuring during the exposure of the DF image can lead to radiation damage artifacts (53).

Bright field (BF) and dark field (DF) electron microscopy were performed using a JEOL 100CX "TEMSCAN" as both a conventional transmission electron microscope (CTEM) and as a scanning transmission electron microscope (STEM). Minimum exposure in CTEM was accomplished by using a low dose rate, damaging only the area under observation at the low magnification of 3,300X and focusing on adjacent areas and then recording the DF image using approximately 60% of the available τ. Low dose rates were achieved by using the #3 condenser aperture, spot size between 2 and 3 (intermediate conditions were obtained using the free lens control) and reducing the filament bias. These conditions resulted in an electron flux of $\sim 3 \times 10^{-4} A/cm^2$ on the sample and a beam divergence of between 1×10^{-3} and 1×10^{-5} radians such that the PE diffraction pattern lasted approximately 60 seconds.

DF images were recorded with tilted beam illumination using the 110 and 200 reflections and the #4 objective aperture (radius of $0.067 \mathring{A}^{-1}$ at 100 kv). The procedure was to first focus in BF with the aid of the image wobbler then to translate to an undamaged area that had thin fibrils. Specimen motion due to thermal drift was minimized by avoiding large fibrils and the grid support bars. The DF image was then recorded with a 45 sec. exposure using Kodak Electron Image Film 4463 or duPont "low-

dose" x-ray film.

Electron diffraction patterns were obtained from relatively large areas ~50 μm in diameter, as defined by the incident beam diameter, to achieve sufficient peak signal to noise at a low dose. All patterns were obtained from previously undamaged areas at doses less than 10% of τ with a beam divergence less than 1×10^{-5} radians. This low divergence permits crystals up to 3,000Å to be measured by line breadth analysis. The peak profiles were determined with a Joyce-Loebel microdensitometer from the Kodak Electron Image Film type 4463.

Further details of the relatively new technique of STEM as applied to polymer morphology is the subject of Chapter III.

2.6.3 Comparison of techniques. The DF images from the samples prepared by detachment replication and nitric acid etching were compared to eliminate the possibility of artifacts caused by specimen preparation. Figure 2a is a composite of several regions from combined 110-200 CTEM DF showing crystalline regions along the detached microfibrils (L polymer, EDR 36). The crystallites average approximately 250Å in width (e.g., the full width of the microfibril) and have a range of thicknesses from 125 to 450Å along the fibril direction. The crystallites appear both singly and in short regular sequences. The shortest intervening

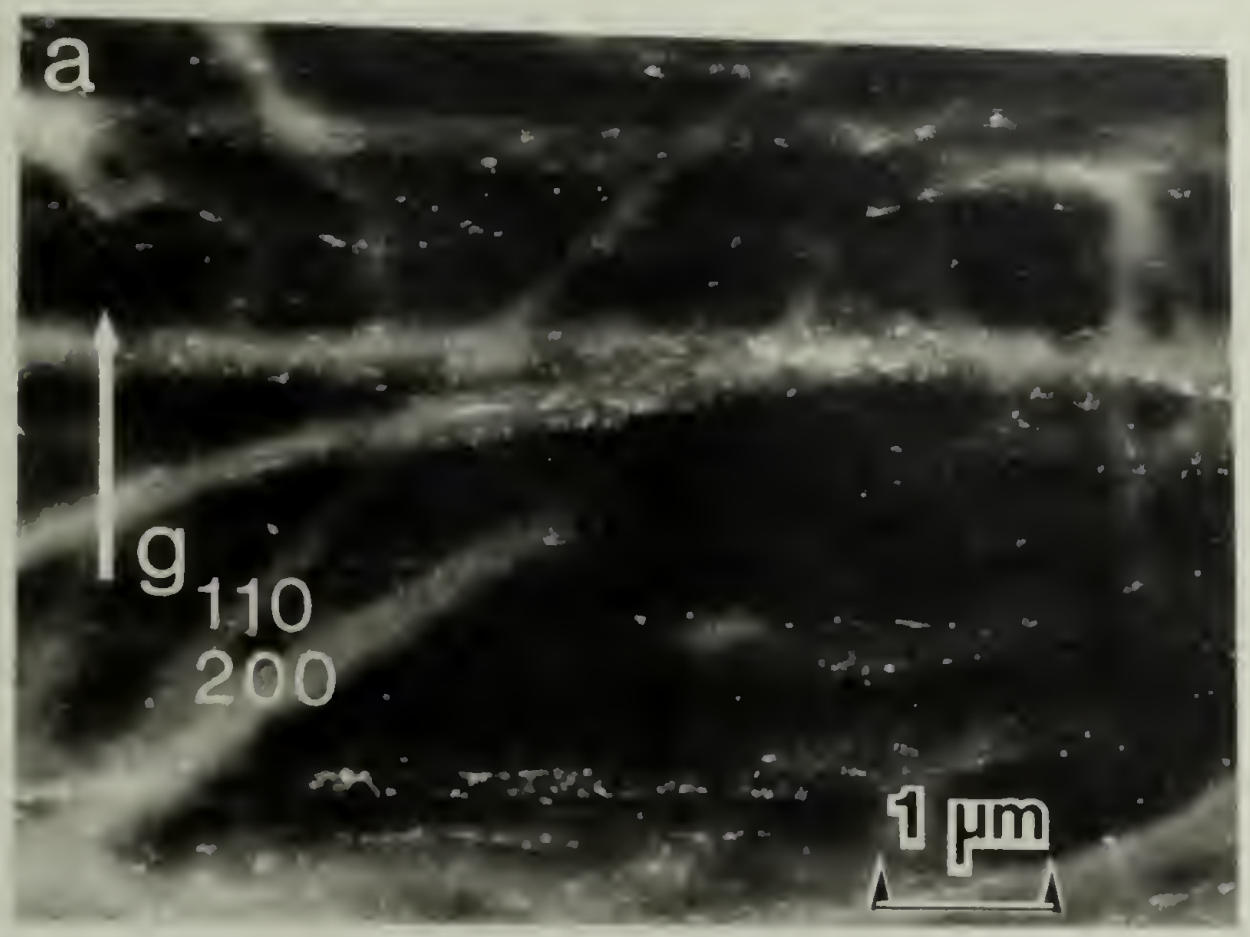

Figure 2.2. Comparison of the results of the specimen preparation procedures: (a) CTEM-DF of the detachment replica using the combined 110 and 200 reflections; (b) STEM annular DF of the nitric acid etch fragments.

dark nondiffracting regions are about 70Å long. Figure 2b is a STEM annular DF image of the fibrous etch fragments of the same sample. The crystallites imaged are more numerous since more diffracted beams (approximately 36 reflections) contribute to the dark field image, but the crystallite size and orientation along the microfibrils is essentially the same as observed in CTEM DF of detachment replicas.

A further approach to elucidate microfibril substructure is the use of gold decoration. Gold particles have been shown to preferentially nucleate on crystal edges and amorphous regions in semicrystalline polymers (54). This gold decoration provides another technique to distinguish the crystalline and amorphous regions in these fibers. Individual gold particles are about 50Å in diameter. Figure 3 is a CTEM BF image of a gold decorated etch fragment. The gold particles cluster to form short, meandering rows separated by denuded (presumably crystalline) regions. A somewhat regular spacing of the gold particles along the fiber axis is evident. Optical diffraction from the micrograph negative yields a textured, broad scattering pattern with a maximum along the meridian corresponding to an average spacing of approximately 150Å. A discrepancy between the long period determined by gold particle spacing and SAXS was noted by Shimamura (55). He attributed this to the gold particles depositing on all types of disordered and defect regions on the surface resulting in

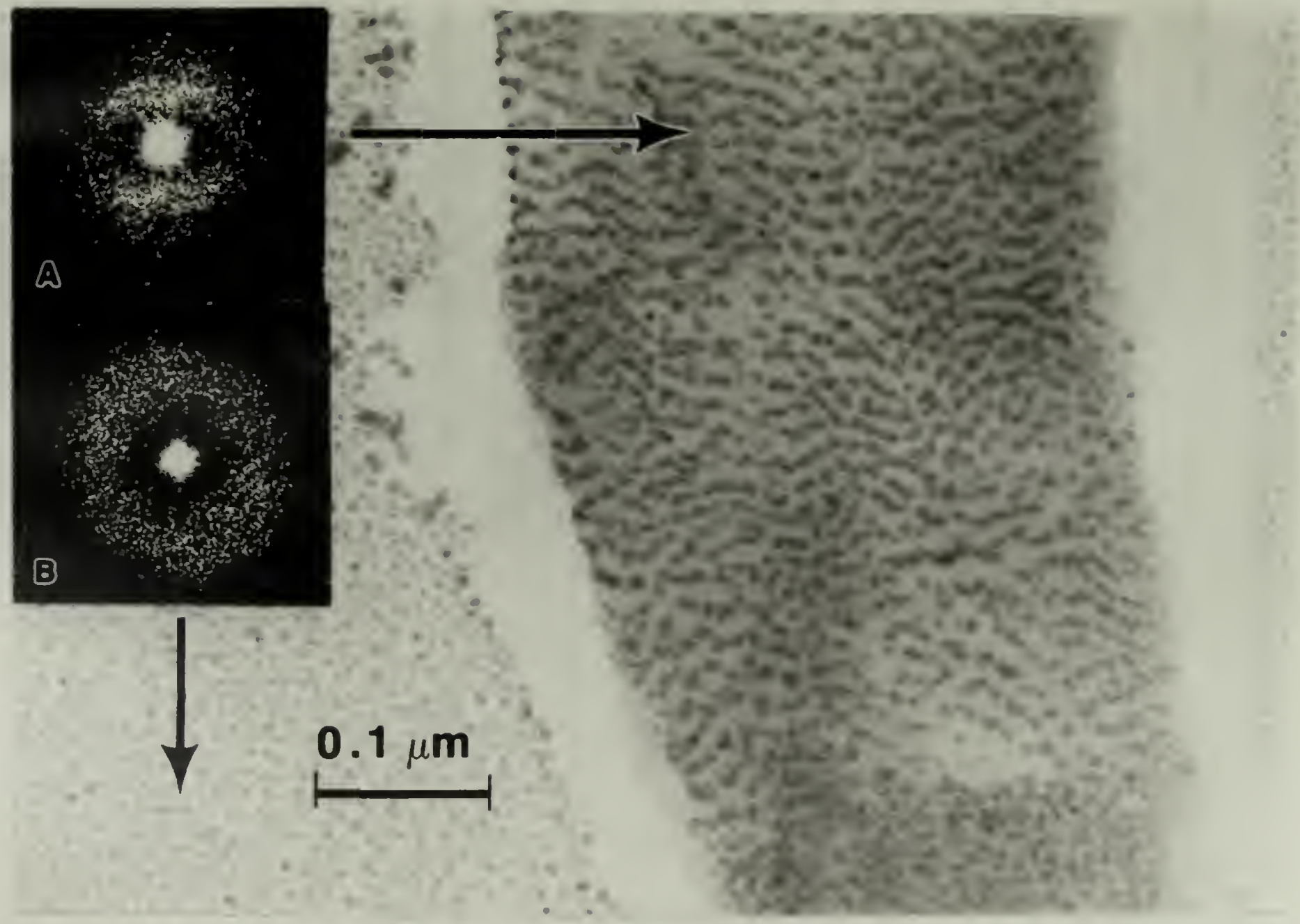

Figure 2.3. CTEM-BF of a gold decorated etch fragment. Insets are optical transforms obtained from: (a) fiber; (b) substrate, as indicated by the arrows.

a lower average particle separation compared to the SAXS peak position determined long period which results only from contributions of the regularly-stacked crystalline regions.

The detachment replica procedure was also applied to high pressure crystallized PE (242°C and 5000 atm.). This sample of Alathon® 7040 (M_w = 90,000, M_w/M_n = 7) was kindly supplied by Dr. H. Hoehn of DuPont and is described as sample #2 in his publication (56). Since this sample has a well characterized extended chain morphology it was used to determine if the sample preparation and microscopy techniques were indeed sufficient to identify long extended chain crystals. A CTEM-BF image of a detachment replica of this high pressure crystallized material is shown in Figure 4a. In this micrograph the replicated extended chain crystal blocks extend about 1 μm in length in the chain direction. Darker block like regions are also observed. These are detached extended chain PE regions that adhered to the replica. Figure 4b shows detached regions from a typical area imaged in CTEM-DF using the 110 and 200 reflections. The white arrows point to detached PE that is diffracting (bright) over regions 2,000 to 8,000 Å in length indicating that a substantial part of the crystal lattice has been imaged.

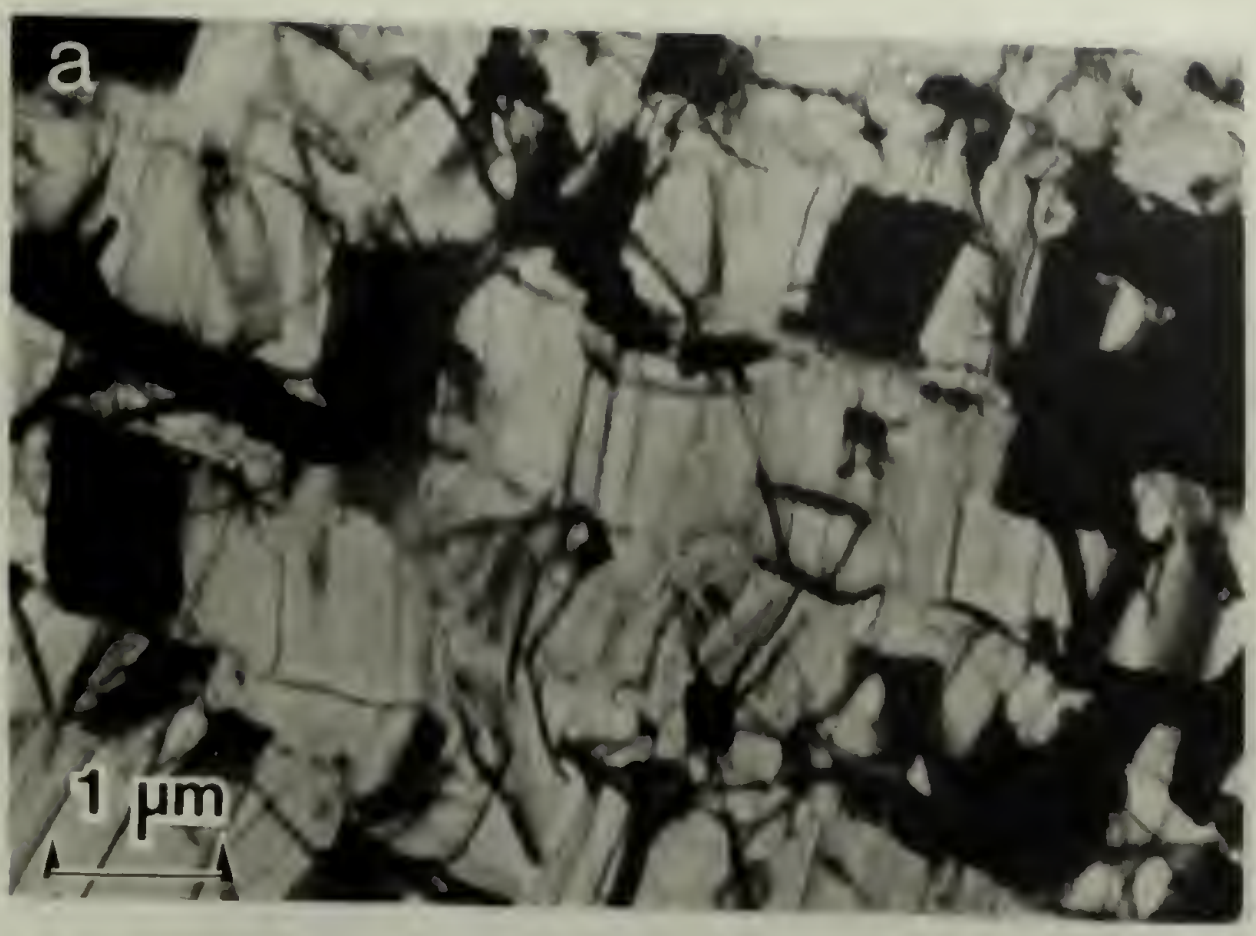

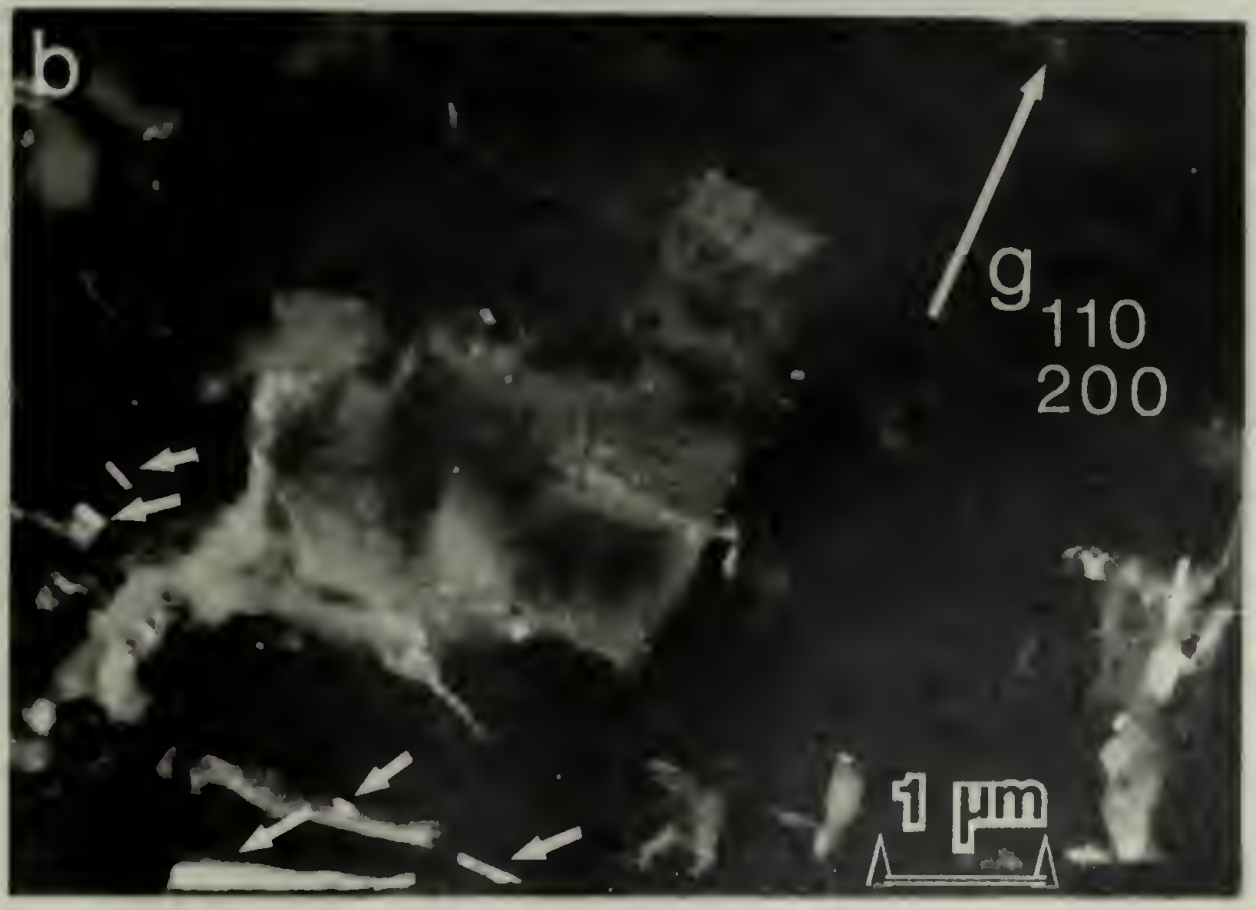

Figure 2.4. Detachment replica of high pressure crystallized polyethylene. (a) CTEM-BF image. (b) CTEM-DF image using 110 and 200 reflections.

2.7 Small Angle X-ray Scattering (SAXS)

Small angle x-ray scattering was performed at Oak Ridge National Laboratory, Oak Ridge, Tennessee, using the 10-meter camera (complete details of this facility are given in reference 57). The pinhole collimation and two dimensional position sensitive detector made this instrument the ideal choice for studying the anisotropic scattering from these fibers. The CuKα x-ray source was monocromated by pyrolitic graphite in the incident beam. The incident beam intensity on the sample was 4.7×10^5 counts/sec. It was measured using a series of multiple nickel foils (58). Specimen transmittance, T_s, was measured by comparing the small angle scattering of the sample with a glassy carbon standard, which scatters strongly at small angles, to the scattering from the glassy carbon alone (57).

Solid state extruded samples that were intially cylindrical, were trimmed on both sides to flat slabs approximately 1.0 mm thick using a rotary microtome with a glass knife. Film samples were stacked to achieve approximately 1.0 mm total thickness. All samples were wider than 1.0 mm so that the incident 1 mm x 1 mm x-ray beam was completely covered by sample. Data was collected at specimen to detector distances of 412 cm and 220 cm to cover angular ranges of 24 mrad. and 45 mrad., respectively.

The SAXS invariant, Q, was determined by integrating the scattered intensity recorded by the two-dimensional detector assuming fiber rotational symmetry according to:

$$Q = 4\pi \int_0^\infty \int_0^\infty I(S_1,S_2)\, S_2 dS_1 dS_2 \qquad (2.2)$$

where $S = (2\sin\theta)/\lambda$, 2θ is the scattering angle and S_1 and S_2 are vectors parallel and perpendicular to the fiber axis respectively (59).

Exclusion of void scattering and zero order scatter near the origin reduced Q by only about 10% and was used as the criteria to determine the uncertainty in Q. Background contributions from slits, parasitic scattering, dark current and thermal diffuse scattering were subtracted from $I(S_1,S_2)$. The thermal diffuse scattering was determined from the constant value that $I(S_1,S_2)$ reached at the high angle tail (45 mrad.) of the SAXS.

2.8 Wide Angle X-ray Scattering

Profiles of the (002) reflection were also recorded from the extrudates using a Siemens D500 wide angle diffractometer employed in the symmetric transmission mode with Ni filtered CuKα radiation. The beam divergence was minimized for line broadening measurements with 0.1° incident beam slits and a 0.018° receiving slit so that a 1.5 mm thick hexamethylene tetramine standard had an inte-

gral breadth of 0.131° for a reflection at 76.73° 2θ.

The PE sample profiles were recorded over a 5°2θ angular range starting from 73° at a rate of 0.1°/min. The count rate was typically 150 counts/sec. at the main peak. The background was found to be a constant (~3-5 counts/sec) on both sides of the peak. The Rachinger correction (60) was applied to remove the $CuK\alpha_{II}$ peak from the (002) profile. Integral breadths, $\Delta\beta_{obs}$, were calculated from the corrected profiles by

$$\Delta\beta_{obs} = \frac{1}{I_{max}} \int I(2\theta)d(2\theta) \qquad (2.3)$$

where I_{max} is the maximum peak intensity.

The correction of the observed integral breadths for instrumental broadening depends on whether the peak shapes are Cauchy or Gaussian (61). If the profiles are Cauchy:

$$\Delta\beta_{obs} = \Delta\beta_{L} + \Delta\beta_{instr.} \qquad (2.4)$$

while for Gaussian profiles:

$$\Delta\beta_{obs}^{2} = \Delta\beta_{L}^{2} + \Delta\beta_{instr.}^{2} \qquad (2.5)$$

where $\Delta\beta_{L}$ is the broadening from the sample. Since observed peaks can be combinations of Cauchy and Gaussian shapes we have calculated the mean crystal length for both cases using the Scherrer equation:

$$L^{WAXD} = \frac{K\lambda}{\Delta\beta_L \cos\theta} \qquad (2.6)$$

where K = 1.0 for 00ℓ reflections (62).

The crystal size determined from electron and x-ray diffraction will be a minimum bound on crystal coherence length since paracrystal distortion, lattice defects and lattice strain give additional peak broadening contributions.

2.9 Birefringence

The birefringence of the flat film samples of draw ratio 9 was measured using an Ehringhaus calcite rotary compensator with a Zeiss polarizing microscope and a white light source. The extruded samples of circular cross section were not sufficiently transparent to accurately measure the birefringence.

C H A P T E R I I I

SCANNING TRANSMISSION ELECTRON MICROSCOPY (STEM) OF POLYETHYLENE

3.1. Introduction

The chief limitation to the use of electron microscopy for the study of crystalline polymers is the radiation damage produced in the polymer by the electron beam. Early workers were quick to discover that polyethylene crystals changed contrast and their diffraction patterns faded in a fraction of a second when viewed under an intense electron beam (63). Observations of diffraction contrast features (such as dislocations and fold domain boundaries) and recording of diffraction patterns are possible but are severely limited due to the damage of the crystalline lattice by the electron beam (52,64). Scanning transmission electron microscopy (STEM) has been suggested to have an advantage over conventional transmission electron microscopy (CTEM) for two principal reasons: (1) the collection efficiency of scattered electrons is higher for STEM than for CTEM [which results in higher S/N ratios in the image for a given incident electron dose (or equivalently a reduced specimen dose is possible for the same quality image)] and (2) microarea diffraction patterns may be obtained without

cumulative radiation damage to adjacent areas.

In this chapter advantages and applications of STEM for radiation sensitive semicrystalline polymers are examined. The minimum scattering volume for obtaining scanning microdiffraction patterns for polyethylene is determined. Various modes of STEM dark field imaging are discussed and applied to polymer morphologies.

3.2. Operation of STEM for Radiation Sensitive Polymers

Figure 1 shows schematically the basic components of a STEM. The central feature is a highly focused beam of small diameter (10 to 60 Å for CTEM with scanning attachment and as low as 2 Å for dedicated STEM) which is sequentially scanned over the thin specimen. The beam is focused onto the specimen by the strong prefield of the objective lens and the transmitted electrons are detected by a photomultiplier tube (PMT). In order to form the image, the amplified signal is displayed on a cathode ray tube (CRT) which is synchronized with the scan coil of the incident illumination. Image contrast arises from variations of the transmitted intensity. The magnification is set by the ratio of the area of the scan on the CRT to the area of the scan on the specimen. The bright field (BF) image is recorded by an on-axis disc detector. A second annular detector outside the BF disc detector may be used with a

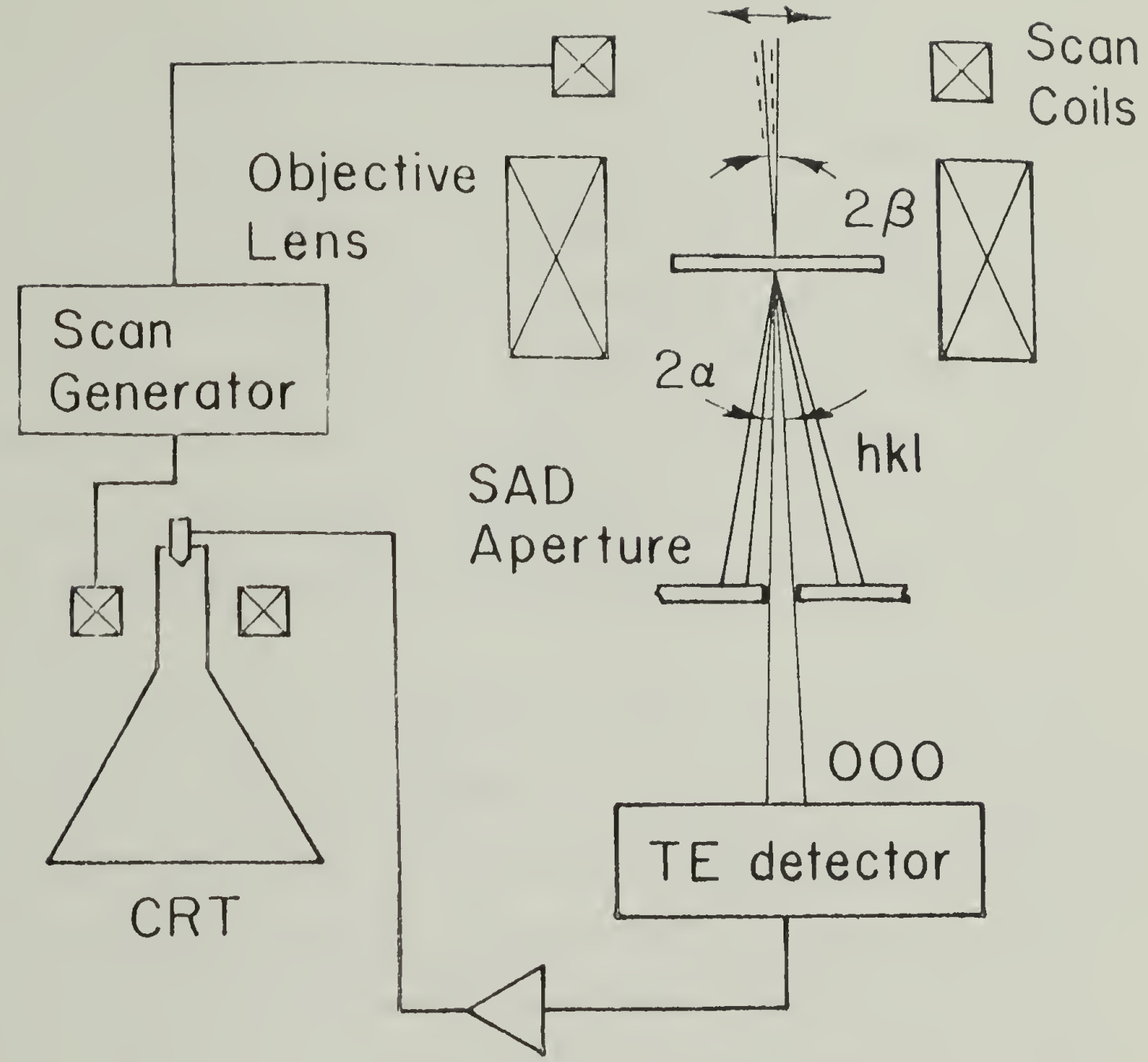

Figure 3.1 Schematic illustrating the basic components of a STEM.

second viewing CRT to provide simultaneous BF and DF images (see Figure 2). Also, the BF disc detector may be made effectively into an annular detector by blocking out the main transmitted beam with, for example, the diffraction beam stop. For crystalline specimens where a specific reflection is desired to form the DF image, the intermediate lens aperture (SAD aperture) can be used to block out all scattered intensity but the reflection of interest. Because the illumination in STEM is conical, the BF disc detector angle α should be equal to the illumination angle β (see Figure 1).

STEM has been suggested to have an advantage over CTEM for two principal reasons: (1) the collection efficiency of scattered electrons is higher for STEM than for CTEM and (2) microarea diffraction patterns may be obtained without cumulative radiation damage to adjacent areas (65,66,67). Specific comparison between STEM and CTEM depends precisely on the type of incident illumination, mode of image formation, type of image contrast and image resolution desired. Because the STEM image is collected point by point, the various kinds of transmitted electron signals can be processed in many possible ways permitting, for example, selected energy loss images for chemical mapping, elastic to inelastic scattering ratio images for atomic number contrast, etc. (68, 69). Our approach in this paper will be

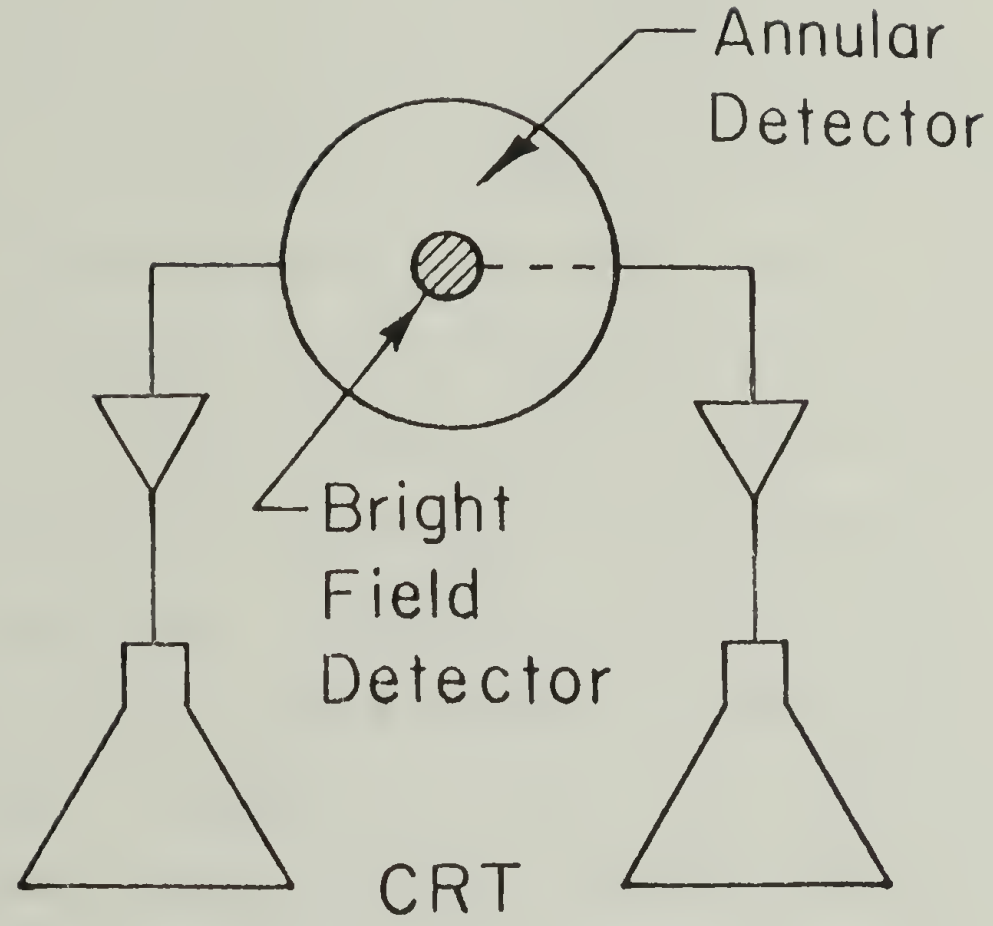

Figure 3.2 Concentric bright field and annular dark field using two amplification and display systems. The bright and dark field images can be observed and recorded simultaneously.

restricted to applications of STEM DF imaging of radiation sensitive crystalline polymers.

Since radiation damage is the limiting factor in electron microscopy of polymers, the main issue is to consider how to minimize the specimen damage to obtain a given amount of information from the specimen (52,64). The electron dose (ϕ_{max}) that can be used to extract information before the sample is severely damaged (thereby making further information more noise than signal) depends only on the radiation physics and chemistry taking place in the sample (52). This maximum level of damage which can be tolerated depends on what type of information is desired from the specimen. Diffraction contrast images and electron diffraction patterns depend on the crystallinity of the specimen. Because the long range crystalline order of the sample is destroyed with increasing electron dose, a limited number of scattered electrons can be used to obtain crystallographic information. By employing higher accelerating voltages (70) or by specimen cooling ϕ_{max} may be increased (71). High voltage does not result in any net improvement because although ϕ_{max} increases, the diffracted intensity per unit incident does decreases by the same amount. Specimen cooling to cryotemperatures (~20°K) results in an approximate 3X improvement of ϕ_{max} over room temperature for polymers which damage by crosslinking by reducing

the mobility and hence the reactivity of the radicals which lead to crosslinking (71). In addition to improving ϕ_{max}, specimen cooling also increases the scattering efficiency by decreasing the loss of diffracted peak intensity due to thermal diffuse scattering (about 10% increase for polyethylene) (72).

The image resolution, δ, is related to ϕ_{max} by the equation:

$$\delta = \frac{SNR}{\left[f\frac{\phi_{max}}{q}\right]^{1/2} C} \qquad (3.1)$$

where SNR is the signal to noise ratio sufficient to detect a signal in a noisy background [it is usually taken as at least 5 (73)], f is the utilization efficiency (i.e., the fraction of the electrons passing through the specimen which contribute to the image), q is the charge of an electron, and C is the contrast (74). Both f and C are imaging mode dependent. Because f and C are coupled as $f^{1/2}C$, the most efficient use of the transmitted electrons (BF) does not necessarily provide the highest resolution (52,64).

The only way of improving resolution at a given specimen temperature is thus to increase f (65). A STEM equipped with an annular detector can collect nearly all

electrons scattered outside of the central beam. Optimum information extraction is achieved if all this signal is transferred without loss to the recording medium and if the information loss in the focusing/area selection/diffraction optics set up steps is negligible in comparison to the radiation damage which occurs during recording. The inherent image intensification, control of illumination location and magnification independent focus capabilities of STEM permit very convenient and precise focusing/area selection/diffraction optics set up without significant radiation damage to the area of interest.

Image intensification is provided by the electronic contrast and brightness controls of the STEM detection system. The electronically manipulated image does not of course contain more information but is merely brighter than the unintensified image (64). The lower limit at which an ideal image intensification system can be used for focusing or area selection is limited by the statistical electron beam noise to about 1×10^{-14} Amp/cm^2. This is a factor 100 - 200 lower than the necessary current density required for minimum microscope phosphor screen brightness for unaided focusing/area selection by the dark adapted eye (75), provided image intensification does not introduce additional noise (commercial systems approach this ideal (76)). Only the specimen region viewed on the CRT is radiation

damaged so that the selected area mode (a variable size reduced raster of the CRT) and variable beam scan speeds are quite useful as discussed in the following example: the specimen is first observed with a rapid scan at low magnification (hence low dose rate) and coarse focus and area selection are accomplished with only slight sample damage. A low quality BF micrograph of the area is taken for reference using the polaroid camera. At this point the selected area mode is used to observe an area from the first selected region that does not contain the precise feature of interest but is sufficiently nearby so focusing on this second region will give adequate focus for the desired area. Now since focus is independent of magnification in STEM (which is not the case for CTEM) the image is focused for high resolution at a high magnification in the selected area mode with a slow scan speed to improve SNR for precise focus, damaging (severely) only a very small area. The magnification is then reduced and full CRT scan is used to record a high resolution image from a nearby undamaged, in focus, selected area. Figure 3 is a BF micrograph taken of a polyethylene single crystal using this method. (Note the nondiffracting area that was damaged during selected area focusing).

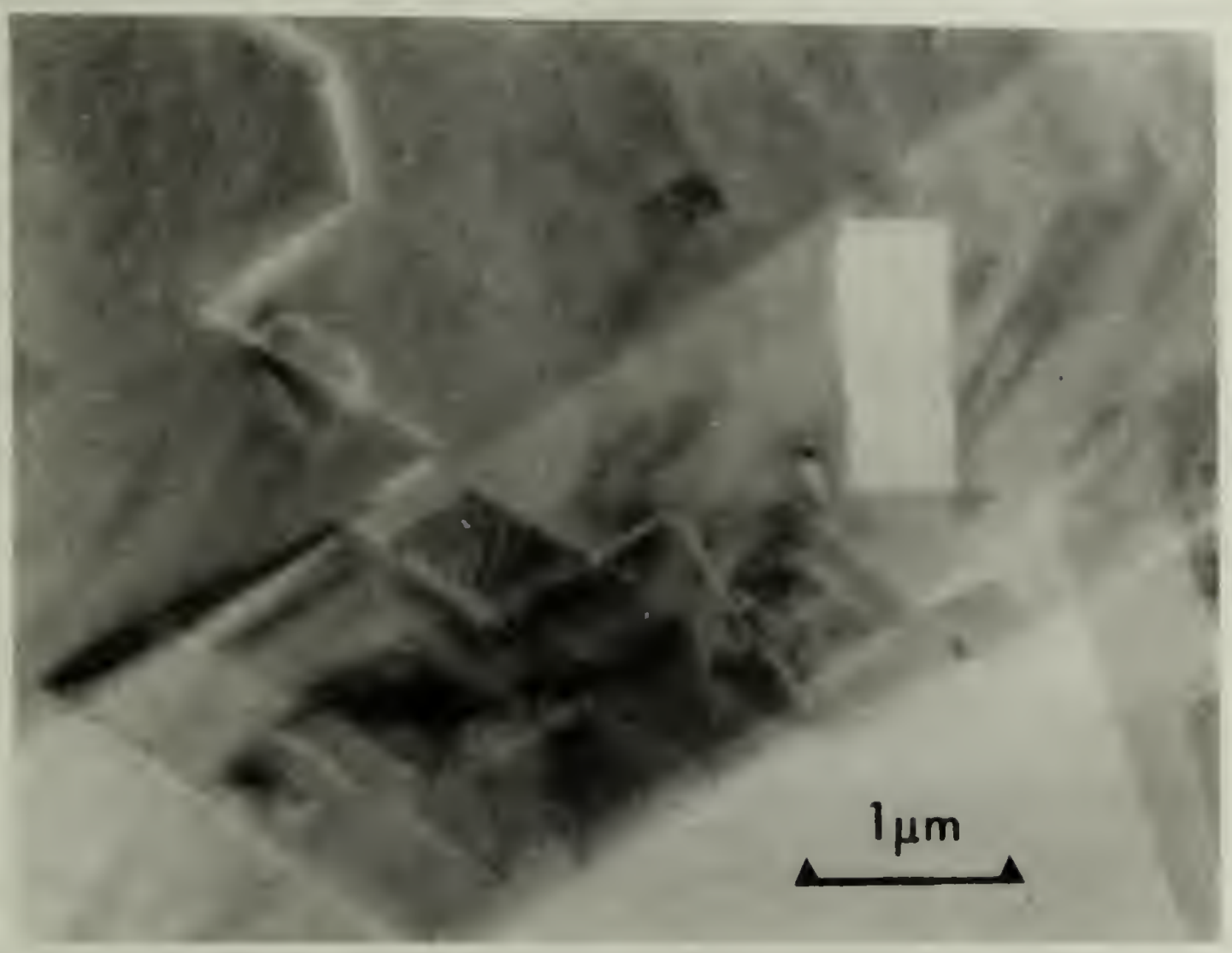

Figure 3.3 Bright field micrograph of overgrown polyethylene single crystals. The rectangular region in the upper right is lighter and lacks contrast because it was radiation damaged during focusing at high magnification.

3.3. Scanning Microdiffraction

For many problems of interest in materials science, it is desirable to know the local crystal structure and orientation and to be able to follow changes in the sample structure and orientation into adjacent areas. Recently, Low et al. (77), have successfully obtained STEM fixed beam microarea diffraction patterns from adjacent areas with beam diameters as small as 0.1 μm in 3000 to 7000 Å thick spherulitic polyethylene films. In this section we demonstrate the usefulness of STEM scanning beam microdiffraction for radiation sensitive polymers and determine the minimum sample volume of polyethylene required for suitable diffraction patterns of single crystals.

3.3.1. Experimental technique. It is informative to briefly review three techniques now available for obtaining diffraction patterns from limited sample areas. The first two techniques are possible with a CTEM; the rocking beam microdiffraction technique requires an STEM.

Conventional selected-area diffraction (SAD) patterns are obtained in CTEM by using a large diameter, parallel beam of incident electrons on the sample with a field limiting aperture (the SAD aperture) placed in the first image plane of the intermediate lens (see Figure 4a). The minimum diffraction area is determined by the size of the

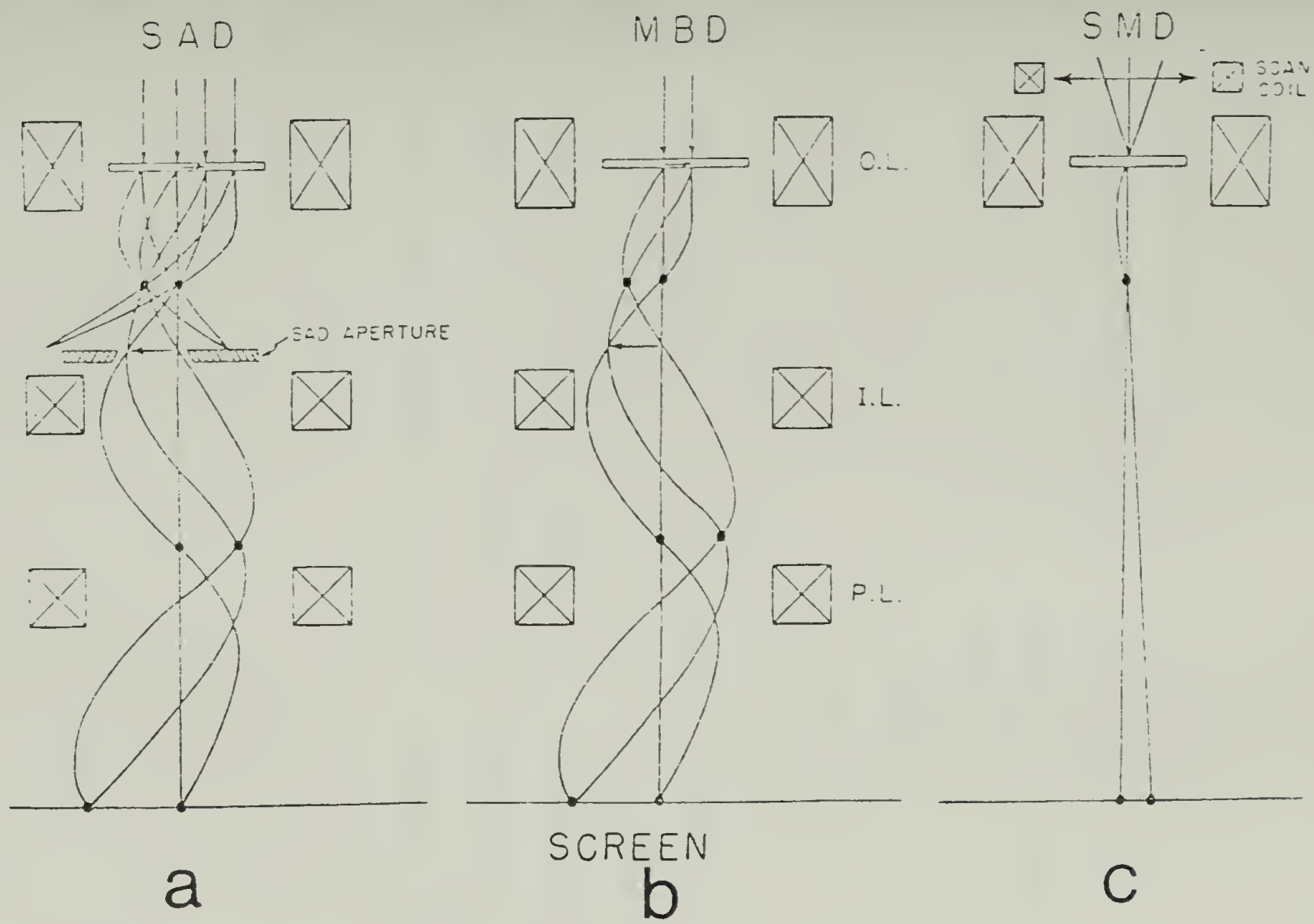

Figure 3.4 Schematic ray diagrams of various diffraction geometries (a) CTEM--selected area diffraction. A large area of the specimen is illuminated with a paraxial beam of electrons. The SAD aperture in the first image plane of the intermediate lens limits the area on the specimen that contributes to the diffraction pattern. (b) CTEM--microbeam diffraction. A small static paraxial beam of electrons is incident on the specimen. The area contributing to the diffraction pattern is determined by the position and size of the microbeam. (c) STEM--convergent beam scanning micro-diffraction. A fine convergent beam of about 200Å diameter is scanned over the sample. The area contributing to the diffraction pattern is determined by the area scanned.

SAD aperture and the spherical aberration of the objective lens (i.e., diffracted electrons from outside the area defined by the SAD aperture contribute to the diffraction pattern). Spherical aberration limits the minimum diffraction area to several hundred nanometers for 100 keV CTEM. Moreover the large incident beam size on the sample eliminates the possibility of recording successive patterns from adjacent areas for radiation sensitive materials.

Microbeam diffraction (MBD) is also possible with a CTEM by using a strongly excited first condenser lens and a very small second condenser lens aperture (typically 20 μm) to illuminate the sample with a fine parallel beam of electrons (see Figure 4b). Since no field-limiting aperture is used, the spherical aberration of the objective lens does not play a role and the minimum diffraction area is the incident beam diameter (c.2500Å). Because the incident beam only illuminates the area of interest, successive patterns may be obtained from adjacent areas. The only drawbacks are the 2500Å size limitation, the non-uniform intensity distribution across the illuminated area (approximately Gaussian), and lack of a precise means of repositioning the beam to an adjacent area of interest.

STEM microdiffraction uses the strongly excited objective lens in a STEM to focus a fine static electron probe on the sample (convergent beam diffraction). The

diffraction pattern formed is then magnified by the lower half of the objective lens. The sample area producing the diffraction pattern is determined again by the incident beam diameter. The beam diameter is fixed by the objective and condenser lens settings and the technique is essentially the same as CTEM-MBD but with much smaller incident beam size due to the strong focusing action of the objective lens. Typical values for a tungsten hairpin filament source operated at 100 keV are 200Å probe size with angular aperture of the convergent beam about 1×10^{-3} rad.

Recently, a second STEM microdiffraction method has been developed employing a rocking incident beam. The sample is positioned midway between the objective lens pole pieces such that a nearly parallel incident beam can be rocked about a point lying in the specimen plane. In this manner diffraction patterns have been obtained from 30Å diameter metal crystals (78). This is approximately the theoretical minimum crystal size for a meaningful diffraction pattern of about 5 times the unit cell size.

3.3.2. Results and discussion. The main obstacle to the successful application of microdiffraction to polymers is, of course, radiation damage. The minimum polymer sample size which can form a useful diffraction pattern is limited by the insufficient S/N statistics in the scattered peaks

at low doses and destruction of the crystal by radiation damage at high doses. Experiments employing the two standard STEM microdiffraction techniques using a JEOL 100 CX "TEMSCAN" with 200Å electron probe and 120Å thick polyethylene single crystals indicated severe radiation damage occurred before a diffraction pattern of the crystal could be obtained. To adopt STEM microdiffraction for radiation sensitive polymers the following procedure was developed (see Figure 4c): the microdiffraction mode of the STEM is selected and the optics are adjusted for the normal convergent beam diffraction pattern at 100,000 X magnification. However, instead of operating in the spot scan mode (stationary beam) the selected-area frame scan mode is used. The selected-area scan is adjusted to scan a square area W cm x W cm on the CRT (corresponding to W x 10^3Å by W x 10^3Å on the sample). A scanning beam microarea diffraction pattern can thus be viewed on the fluorescent screen. By systematically varying the size of the scanned area and recording (using the normal electron image plates) diffraction patterns at fixed incident beam current, we determined that an area approximately 1000Å x 1000Å is the smallest area which yields a "useful" pattern (see Figure 5). The usefulness of a particular diffraction pattern will, or course, depend on what information is required. There will be a sacrifice of signal to noise ratio for

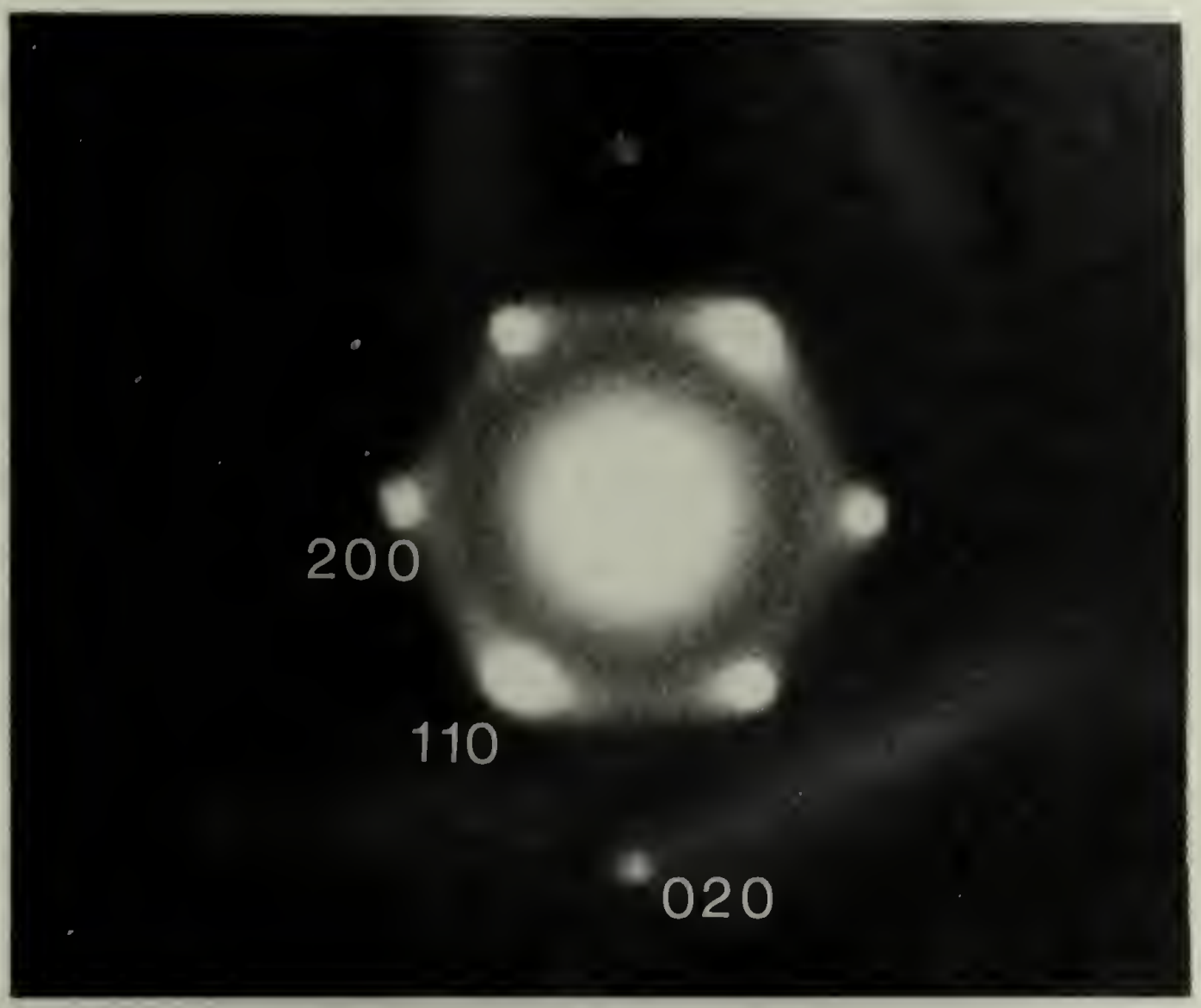

Figure 3.5 Scanning beam microarea diffraction pattern obtained from 1000 Å x 1000 Å area of a polyethylene crystal.

smaller diffraction volumes. The criteria for a useful pattern will also depend on the radiation damage characteristics of the particular reflections of interest. Some reflections simply weaken and disappear as the crystal damages whereas others weaken, shift and broaden, eventually forming an amorphous halo.

The essential differences between microbeam diffraction (MBD) and scanning microbeam diffraction (SMD) are incident beam diameter and beam divergence. To compare MBD and SMD, it is necessary to assess the effect of beam divergence and diameter on the scattered peak intensity and peak width. To resolve a given reflection in an electron diffraction pattern requires a sufficient signal/noise ratio and a sufficiently narrow peak breadth.

The effect of beam divergence will be to decrease the diffracted intensity and to broaden the reflections. Assuming kinematical scattering, the scattered intensity will vary as

$$I(s) \sim \frac{\sin^2 \pi st}{\sin^2 \pi s} \qquad (3.2)$$

where t is the crystal thickness parallel to the electron beam and s is the deviation of the incident beam from the Bragg condition (s=0).

An overestimate of the decrease in the diffracted

intensity due to beam divergence can be made by assuming all incident electrons to have a deviation from the Bragg condition equivalent to the beam divergence (e.g., 1×10^{-3} rad). For the 110 reflection of a 120Å thick polyethylene crystal, this amounts to less than a 1% decrease in the scattered intensity.

Neglecting radiation damage and paracrystalline line-broadening contributions, the observed peak width will be:

$$\delta\beta^2 = \delta\beta_D^2 + \delta\beta^2{}_\phi \qquad (3.3)$$

where $\delta\beta_D$ is the broadening due to the beam diameter (effective crystal size) and $\delta\beta_\phi$ is the broadening due to beam divergence.

Beam divergence and beam diameter are in general inversely related--for our conditions the beam divergence for a 1000Å beam is five times less than for the 200Å beam. The contribution to the line broadening from beam size will usually be negligible in comparison to that from beam divergence.

Therefore, for a given total area illuminated and total incident beam intensity the MBD pattern will exhibit sharper reflections because of the inherently lower divergence of a larger incident beam.

The scanning beam diffraction patterns obtained ex-

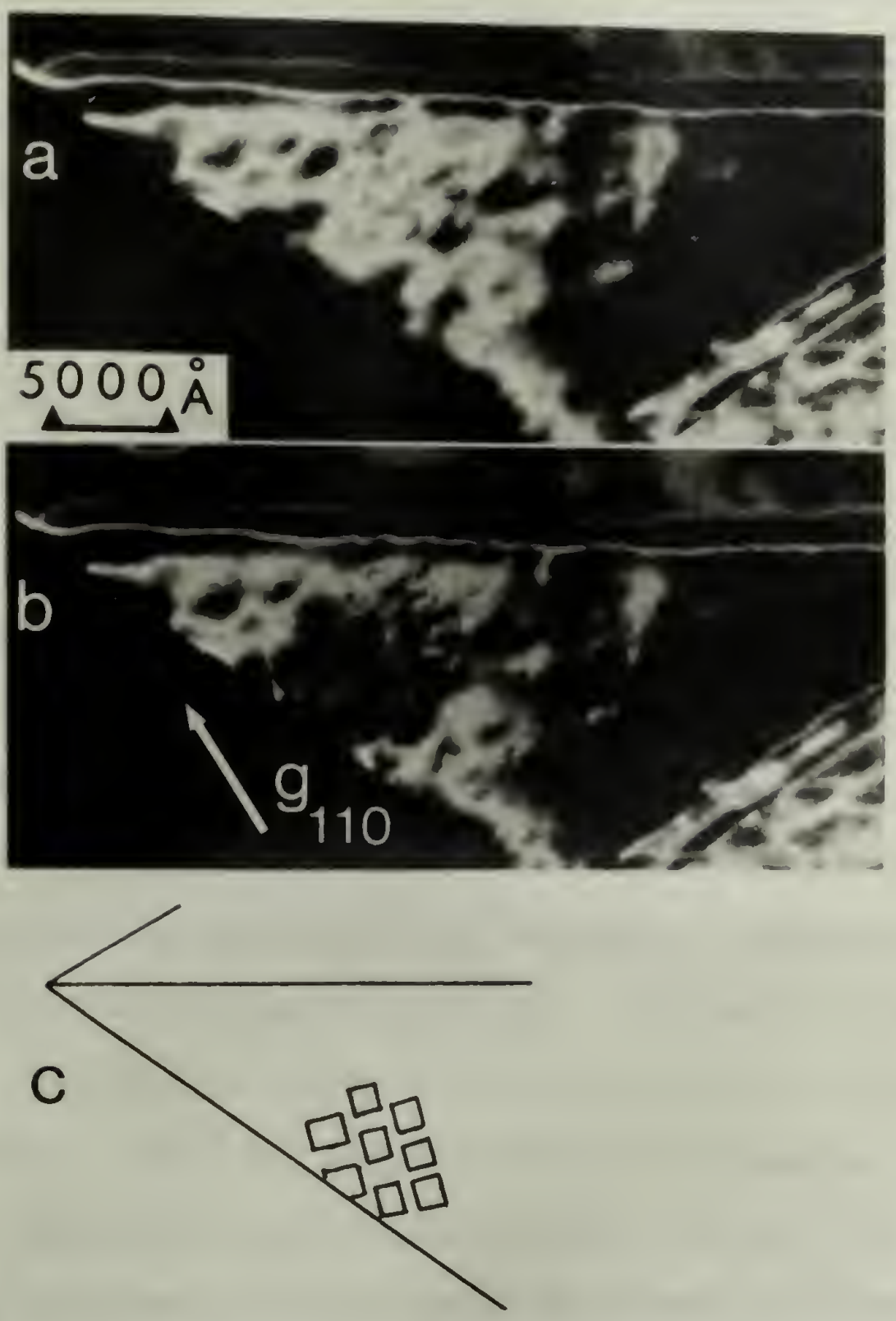

Figure 3.6 110 STEM dark-field micrographs of polyethylene single crystal. (a) Crystal before scanning microarea diffraction. (b) Crystal after eight successive scanning microarea diffraction patterns. Dark regions indicate loss of crystallinity in the regions used for diffraction patterns while the rest of crystal has remained undamaged. (c) Schematic drawing showing location of each 1000 A X 1000 Å region used for forming each scanning microarea diffraction pattern.

hibit broadened diffraction spots typical of the convergent (stationary) beam technique. High order reflections can be observed out to the available limit of 20. The strong 110 and 200 polyethylene reflections are superimposed on an amorphous halo which forms as the crystal becomes damaged during the diffraction pattern exposure. Since the selected scan area can (with the beam off) be electronically adjusted to any rectangular size and shape and as well accurately repositioned in two perpendicular directions on the sample, successive adjacent area scanning microdiffraction patterns can be obtained very routinely.

To demonstrate that such microarea diffraction patterns do, indeed, result from a 1000Å x 1000Å specimen area, we recorded STEM dark-field micrographs of a polyethylene crystal before and after obtaining scanning microdiffraction patterns (see Figure 6). Initially a low dose 110 STEM dark-field micrograph was obtained of a single crystal, then a total of eight successive scanning microdiffraction patterns from adjacent areas of the same fold domain were obtained. The crystal was then re-imaged in 110 dark-field. As can be seen, eight small square regions are dark due to the loss of crystallinity from the local high dose required for each of the diffraction patterns. The dimensions of each region and their corresponding mutual orientation are consistent with that expected from the scan-

ning diffraction geometry. Moreover, the remaining adjacent areas are still quite undamaged.

The conditions we have used for the scanning micro-diffraction are an incident beam diameter of 200Å, incident beam current of approximately 5×10^{-13}A, beam divergence of approximately 1×10^{-3} rad. (20μm second condenser aperture), and the "rapid scan 2" mode which yields a beam velocity on the sample of 5×10^{-3}cm sec^{-1} horizontally and 1×10^{-5}cm sec^{-1} vertically (500 line scans/frame). The diffraction pattern fades in approximately 4 sec. for these conditions. Assuming that the average current density can be approximated by the beam current divided by the area scanned, the total dose/cm^2 is then just the average current density times the exposure time. The calculated value of 2×10^{-2} coulomb cm^{-2} is in reasonable agreement with published values of the crystal lifetime dose for polyethylene at 100k V at room temperature (52,79). Calculations also show that for the beam current density employed (~0.16Acm^{-2}), sample temperature rise due to electron-beam heating should be negligible (80). The only limitations of scanning micro-diffraction are the maximum 2θ allowed by the inner bore of the microscope column (for our JEOL 100 CX, $2\theta_{max} \tilde{=} 3 \times 10^{-2}$rad, e.g., reflections out to about 12Å are obtainable, line broadening due to somewhat larger beam divergence than for MBD and the maximum

scan distance along the sample due to inclination of the incident beam to the specimen surface as the beam scans across the sample.

The minimum sample volume for diffraction from polyethylene at 100keV and room temperature is, therefore, approximately 10^8 Å^3 (e.g., 1000Å x 1000Å x 120Å). This is diffraction from about 4 million carbon atoms. The ultimate spatial resolution would be set by using a single crystal sample of maximum thickness. For polyethylene at 100keV this single scattering thickness is on the order of 1000Å. Thus the minimum area for a useful microdiffraction pattern from a 1000Å thick polyethylene film is 10^5 Å^2.

3.4. Stem Dark Field of Crystalline Polymers

Inherent to all DF imaging is proper selection of the portion of the diffraction pattern which will be used to form the DF image. Such selection is possible by employing relatively low incident beam divergence so that discrete diffraction spots can be resolved in the diffraction pattern (81). For our JEOL 100 CX microscope, a small (~20 m diameter) second condenser aperture with a 60Å electron probe diameter permits the individual reflections of a polyethylene single crystal to be resolved (see Figure 7). For these conditions, the contribution of beam size to the line width of the reflections is small in comparison to

Figure 3.7 STEM microarea diffraction pattern from a polyethylene single crystal with beam stop tip for annular DF in position. The reflections are broad due to the large divergence of the incident beam.

that from beam divergence. The minimum polymer sample size which can form a useful diffraction pattern is limited by the insufficient signal to noise statistics in the scattered peaks at low doses and by destruction of the crystal by radiation damage at high doses. By scanning the beam and systematically varying the size of the scanned area at fixed incident beam current, the smallest area (for a given sample thickness) which yields a "useful" scanning micro-area diffraction pattern can be determined.

There are several methods to obtain STEM DF images. If all but one of the reflections are restricted (by the SAD aperture) from reaching the PMT detector, the conventional single beam DF image is obtained. Various types of multiple beam DF images are possible with STEM. In principle, such images could be obtained in CTEM, i.e., using the strioscopy technique where the main beam is blocked by a fine wire placed across the objective aperture, or by using hollow cone illumination. Besides being a very exacting technique, multiple beam CTEM DF imaging is resolution limited by spherical aberration and objective lens defocus image displacements (82). Because STEM imaging is not so affected, the annular DF detector may be usefully employed to increase the utilization efficiency of the scattered signal. Although beam divergence is not normally important

for CTEM DF imaging the rather large beam divergences encountered in STEM imaging must be considered.

Beam divergence and beam diameter are inversely related. The beam divergence β (defined as half the total angular width of the incident beam) can typically vary from about 1×10^{-3} radians for a 200 Å diameter beam (micro-diffraction mode) to about 5×10^{-2} radians for a 10 Å beam (high resolution imaging mode). The effect of increased beam divergence will be to decrease the diffracted intensity and to broaden the reflections. The DF image efficiency will of course depend on the diffracted intensity. The diffracted intensity is governed by the well known equation for the rocking curve:

$$I(s) \sim |F(hkl)|^2 \frac{\sin^2 \pi st}{\sin^2 \pi s} \qquad (3.4)$$

where F(hkl) is the structure factor for the (hkl) reflection, t is the crystal thickness parallel to the optic axis and s is the deviation of the (hkl) planes to be imaged from the Bragg condition (s=0). The magnitude of s depends on the magnitude of the diffraction vector of the reflection used, g, and the amount of divergence of the beam ($s \tilde{-} g\beta$). Since the STEM illumination is conical, there is a distribution of s. If, as is usual, the second condenser aperture is evenly illuminated, this incident intensity

distribution $\rho(\beta)$ will be

$$\rho(\beta) = \begin{array}{l} 1 \text{ if } |\beta| < \beta^* \\ 0 \text{ if } |\beta| \geq \beta^* \end{array} \tag{3.5}$$

Thus the scattered intensity of a reflection g with an incident beam divergence of β^* will be given by

$$I_g(s^*) \simeq |F_g|^2 \int_{-g\beta^*}^{g\beta^*} \rho(s) \frac{\sin^2 \pi st}{\sin^2 \pi s} ds \tag{3.6}$$

For a perfectly parallel incident beam ($\beta^* = 0$), the scattered intensity will be proportional to t^2. Figure 8 shows calculated curves of the scattering efficiency (defined as $I(s^*)/t^2$) as a function of the maximum deviation parameter s^* for different crystal thicknesses. For the typical beam divergence range ($1 \times 10^{-3} < \beta < 5 \times 10^{-2}$ radians) the maximum deviation parameter varies from approximately 0.2 to 1.0×10^{-3} $\mathring{A}^{-1}$. It is apparent for thick crystals that a significant portion of the possible Bragg scattered intensity could be lost. The beam divergence thus should be kept below about 5×10^{-3} radians. This requires about a 20μm diameter second condenser aperture (instead of the normal 100μm) to yield a low divergence small diameter beam (although now of relatively low brightness--requiring increased gun brightness and decreased beam scan rates).

A large divergence can also be useful. For a very

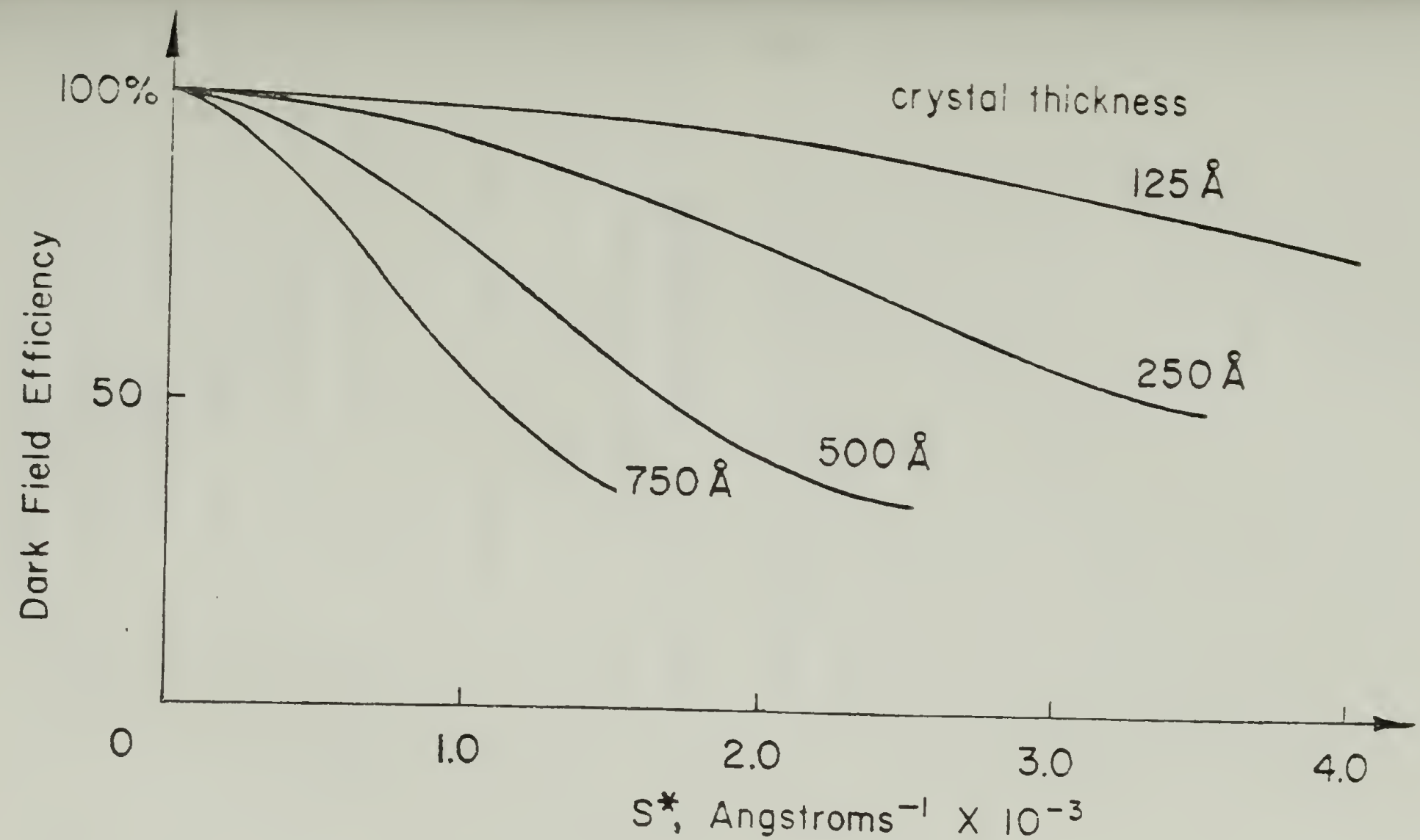

Figure 3.8 Dark field efficiency for various crystal thickness as a function of the maximum deviation parameter.

parallel illuminating beam, as in CTEM, Bragg diffraction is strong for only a limited tilt range of the crystal. STEM will image crystals in DF over a greater tilt range than CTEM, however, the images of the crystals will be somewhat less intense because of the larger beam divergence. On the average more crystals will be imaged per unit area and the image will be less sensitive to tilt of the crystallites. It should be mentioned that when several diffracted beams contribute to the image, diffraction contrast image interpretation is rather complicated. The least efficient, tilted CTEM single beam dark field mode provides the easiest interpretation since both the diffraction vector g and the deviation parameter s are unique.

3.4.1 Applications. We have employed the multiple reflection (n beam) DF technique in several ways. By simply blocking the main beam with the diffraction beam stop tip a DF image employing all excited reflections is produced. This type of DF image is essentially the complement of the BF image. Depending on the orientation, it is possible for several reflections from the same crystal to contribute to that crystal's image, resulting in a higher SNR than for single beam DF. The image intensity of a crystal will be proportional to the crystal thickness along the optic axis, the number of reflections contributing and their respective

structure factors. The resolution improvement attainable depends on the square root of the intensity enhancement. For a polyethylene crystal with the (hk0) reciprocal lattice orientation (a rather favorable situation for n beam imaging) the n beam image (n is about 20 beams) by structure factor calculation (room temperature, 100 KV) should be approximately 9X more intense (83). This would result in a 3X improvement in resolution. Since single beam g_{110} DF resolution is estimated at about 40 Å for a 120 Å thick lamella (52, 64), STEM annular n beam DF for this crystal orientation should yield a resolution of perhaps 15 Å--the same as the practical beam size limited resolution of a tungsten hairpin filament STEM.

An example of the intensity enhancement of an n beam annular DF image compared with a single beam DF image for a polyethylene single crystal is shown in Figure 9. By using the selected area mode for microdiffraction the optics were adjusted so that the left half of the crystal was imaged by the annular DF mode and the right half was imaged using single beam g_{110}DF. Images of both halves were recorded under identical illumination conditions.

In order to demonstrate improved image resolution by STEM DF, some reliably known convenient scale (15-100 Å) high diffraction contrast objects must be present. The crystallite blocks in microfibrils represent such objects.

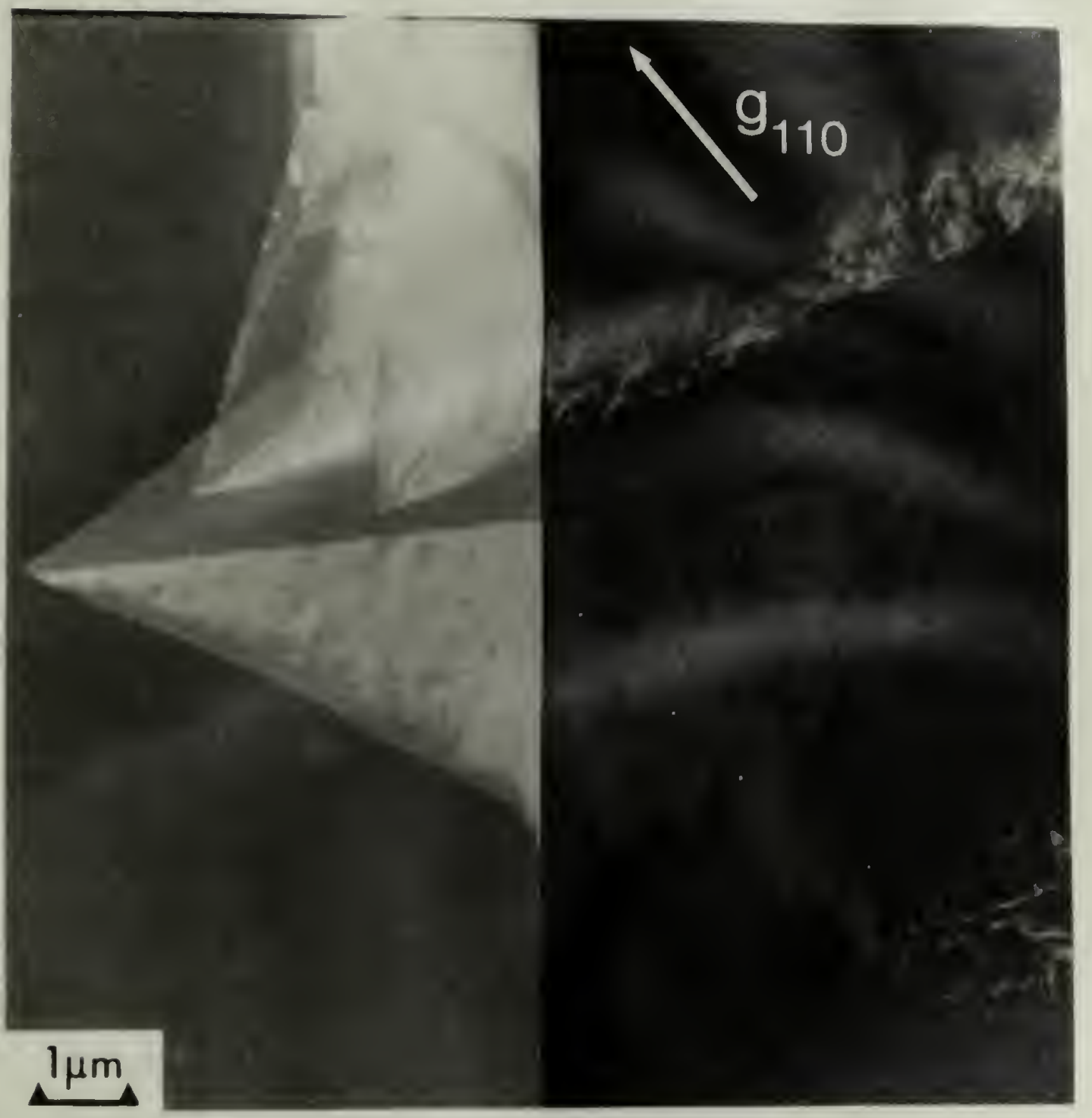

Figure 3.9 N beam annular versus single beam dark field for two halves of the same single crystal. Spot size approximately 60 Å, beam divergence 3.7 x 10^{-3} radians.

Figure 10 is a STEM annular DF image of microfibrils within a microneck zone of a deformed spherulitic polyethylene film. The relatively undeformed regions on either side of the transformation zone are overexposed in this micrograph because of the greater sample thickness. Small 50-200 Å diameter crystallites alternate along the fibril axis with thin nondiffracting regions. In the enlargement (Figure 10) the crystallites appear with rounded corners because of the approximately 15 Å incident beam diameter. Arrows point to adjacent diffracting crystallites separated by 25 Å.

Annular n beam DF imaging is also very useful for detecting various types of crystalline material persent only in a small volume fraction of the sample. Normally reflections from such low volume fraction species would be totally obscured in the diffraction pattern, making it nearly impossible to locate properly (only by trial and error) the reflections of interest in the objective aperture. With STEM annular DF however, all regions which diffract are imaged. Figure 11 shows an example of the DF imaging of intercrystalline links by this method. A sample of polyethylene was co-crystallized with a low molecular weight paraffin and the paraffin subsequently solvent extracted to reveal the intercrystalline links between adjacent lamallae (84). The arrows in the figure indicate the intercrystalline links which appear <u>not</u> to be continuously crystalline along

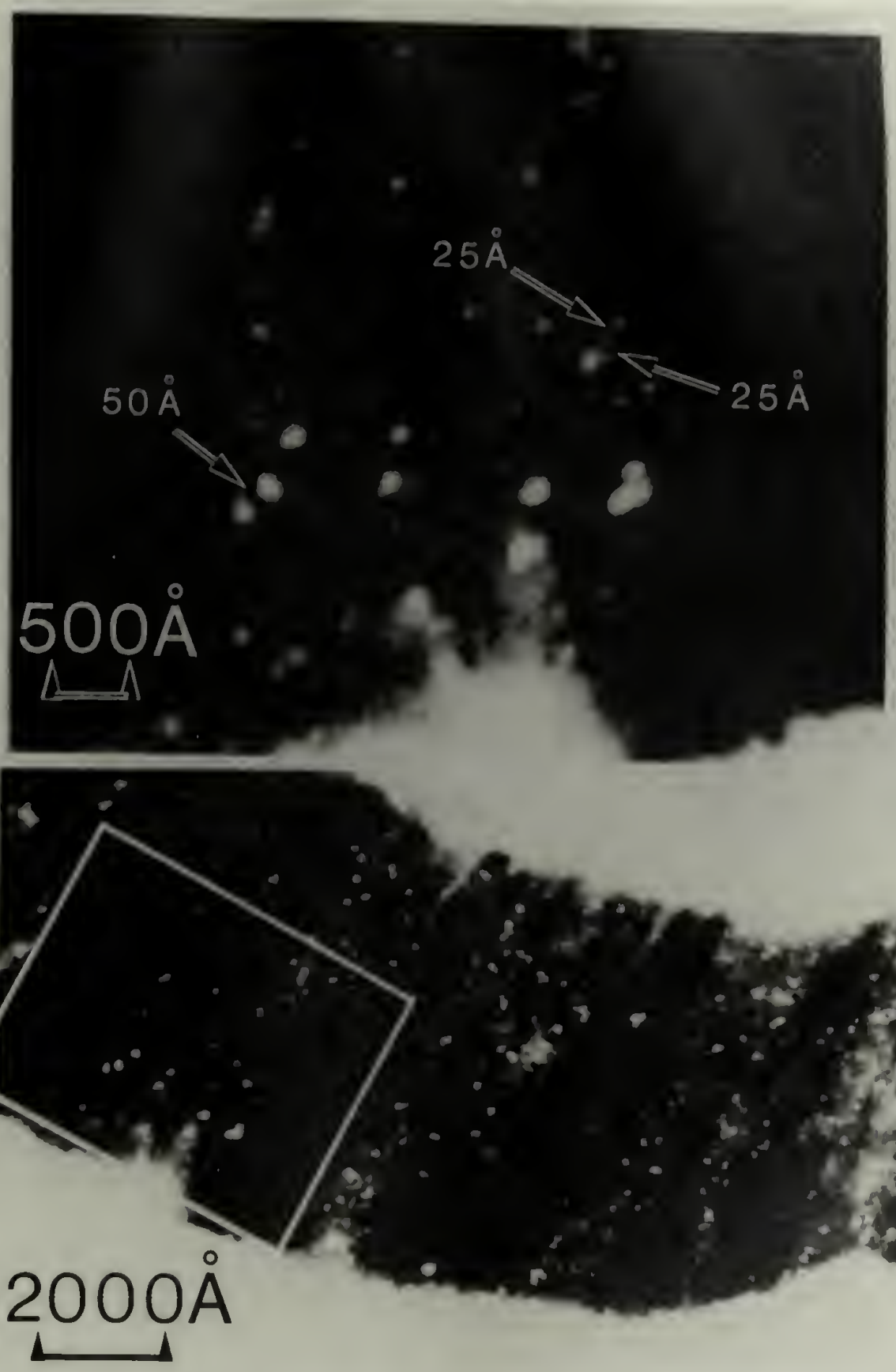

Figure 3.10 STEM n beam annular DF image showing 50-200 Å diameter diffracting microfibril crystallites within the microneck zone of a deformed spherulitic polyethylene film.

Figure 3.11 STEM n beam annular DF image of intercrystalline bridges in spherulitic polyethylene. Arrows indicate the bridges which consist of alternating crystalline and noncrystalline regions.

their length as was previously suggested (84) but appear to be composed of alternating crystalline and noncrystalline regions.

Another annular DF mode is to allow only a single diffraction ring from a sample exhibiting a powder pattern to reach the detector. This may be accomplished by a suitable combination of beam stop size and diffraction pattern size [which may be varied using one of the lenses below the specimen (intermediate lens)]. Such an image will reveal all azimuthal orientation of crystals with the given (hkl) plane at the Bragg angle. Figure 12 shows an example of the single powder reflection annular DF image for a spherulitic polyethylene film employing g_{002}. Figures 11a and 11b are BF and n beam annular DF images of the same area as Figure 11c. Except for slight changes in orientation of the film between exposures, it is apparent that the n beam annular DF image is complementary to the BF image. The single powder reflection annular DF image is much simpler in appearance, making for more straightforward image interpretation as compared to the n beam image since the chain axis reflection image shows only the thin lamellar crystals oriented with their chain axis in the plane of the specimen film. This technique is thus very suitable for studying the rotation and orientation of lamellae during deformation. Furthermore, one obtains direct measure of

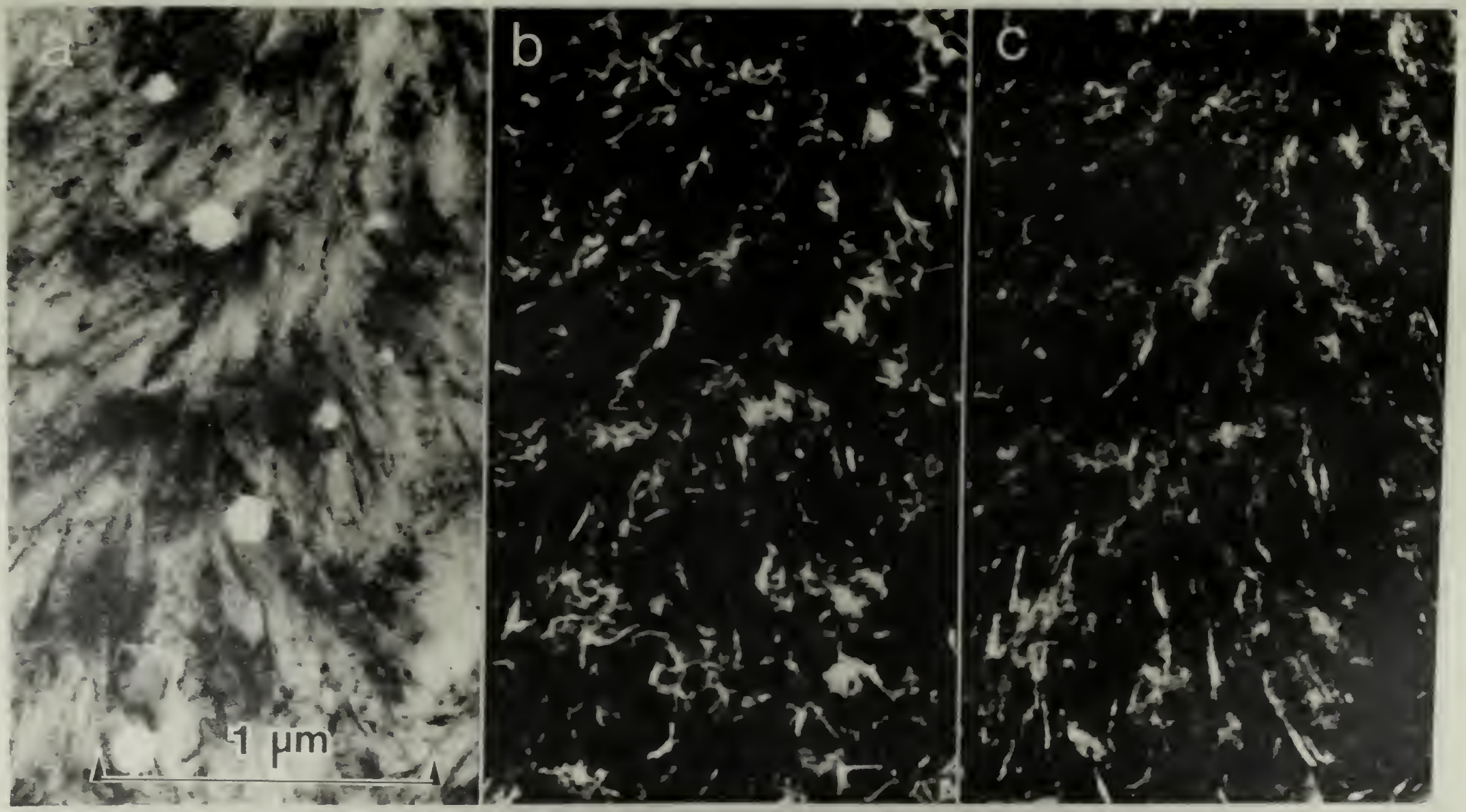

Figure 3.12 (a) STEM BF image of spherulitic polyethylene film.
(b) STEM n beam annular DF image of same region as (a).
(c) STEM 002 annular DF image of same region as (a).

the crystal thickness along the chain direction, which is useful to compare with that determined by small angle x-ray and laser Raman methods.

3.4.2 Summary. The typical approach to CTEM DF imaging of radiation sensitive polymers is to focus in bright field, insert the objective aperture in the diffraction pattern, translate to an adjacent undamaged area and record the (single beam) DF image. The disadvantage of this approach is a low yield of useful micrographs due to focusing errors and blind selection of diffraction optics and specimen areas. This method is clearly difficult for performing systematic studies. Because of image intensification, control of illumination location and magnification independent focus, STEM operation for focusing, area selection and optic set up permits a high yield of systematic data.

STEM DF imaging may be done with one or more reflections. For convergent beam microdiffraction and efficient DF imaging of thin crystals, a small second condenser aperture should be employed so that the beam divergence is less than 5×10^{-3} radians. Use of n beam annular DF allows investigation of crystalline species present only in small volume fractions. N beam annular DF is a high contrast complement to the BF image. Use of the entire azimuthal range of a single powder pattern reflection permits examination of crystal texture--in particular, images produced

by chain axis reflections show the detailed arrangements of lamellae. By using more than one reflection to image a crystal, the DF image intensity and resolution are increased. In the most favorable cases, n beam DF imaging will yield at most a 3X improvement in resolution, or for a given resolution, a 9X increased number of micrographs over single beam DF.

C H A P T E R I V

A COMPARISON OF A LOW AND A HIGH MOLECULAR WEIGHT EXTRUDATE

4.1 Introduction

In this chapter two extrudates of polymers L (Mn= 59,000 M_w/M_n=3) and H (M_n=200,000, M_w/M_n=7 to 13) of the same EDR (24) and produced at the same temperature (120^oC) and pressure (2400 atm.) are compared in structure and properties. The analysis and approach in this chapter is used in the rest of the thesis to gain a better understanding of the actual microstructures present in high modulus polyethylene produced by solid state extrusion.

Sample L was extruded as a whole billet, whereas sample H was extruded as a billet split in half. The details of this technique, have been previously described (35). The split billet extrudes at a much faster rate than the corresponding whole billet under the same extrusion conditions. The second reason is more important for higher molecular weight samples such as M6003. When extruded as a split billet, the H sample has a higher initial tensile modulus than the whole billet extrudate. This is because the split in the extrudate relieves the radial stress component associated

with the tendency for the extrudate to expand (i.e., die swell) (85). The lower molecular weight L sample yields extrudates of equivalent tensile moduli whether it is extruded as a whole or split billet. This is reasonable since the magnitude of the normal force is molecular weight dependent. Samples of L for both split and whole billets at 24X draw ratio show identical flow profiles (86). The L sample extruded at 20 mm/min. while the H sample extruded at 0.6 mm/min. The L and H samples are the same in preparation except for the difference in molecular weight and rate of extrusion.

4.2 Results

4.2.1 Electron microscopy. Figure 1 is a scanning electron micrograph of a gold sputter coated detachment replica of sample L. Fibrils form flat, ribbonlike structures, typically 1-2μm in width with an aspect ratio of approximately 3:1 as determined from twisted regions (see regions A and B).

Detachment replicas also contain much smaller microfibrils than are shown in Figure 1. Figure 2a is a CTEM-BF image with a number of 0.2-0.3μm fibrils and fine microfibrils as small as 250 Å in width. The lower contrast background is from the replica of the longitudinal fracture surface showing a highly aligned microfiber structure. The fibrils and microfibrils which adhered to the replica and were pulled out, are not as well aligned in the extrusion

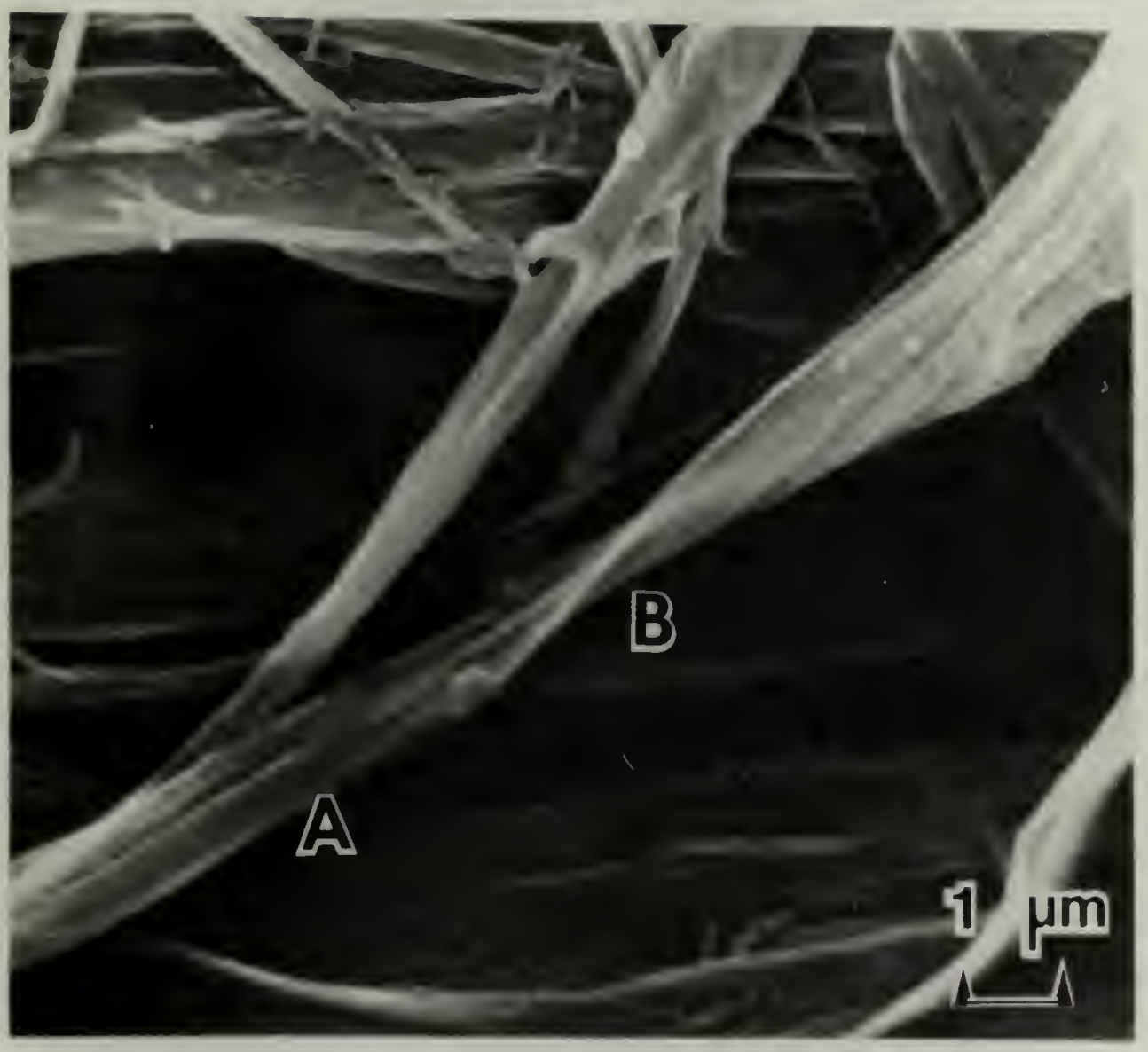

Figure 4.1. Scanning electron micrograph of a gold sputter coated detachment replica of sample L. Twisted regions at A and B indicate the flat ribbonlike structure of the 1-2µm wide fibrils.

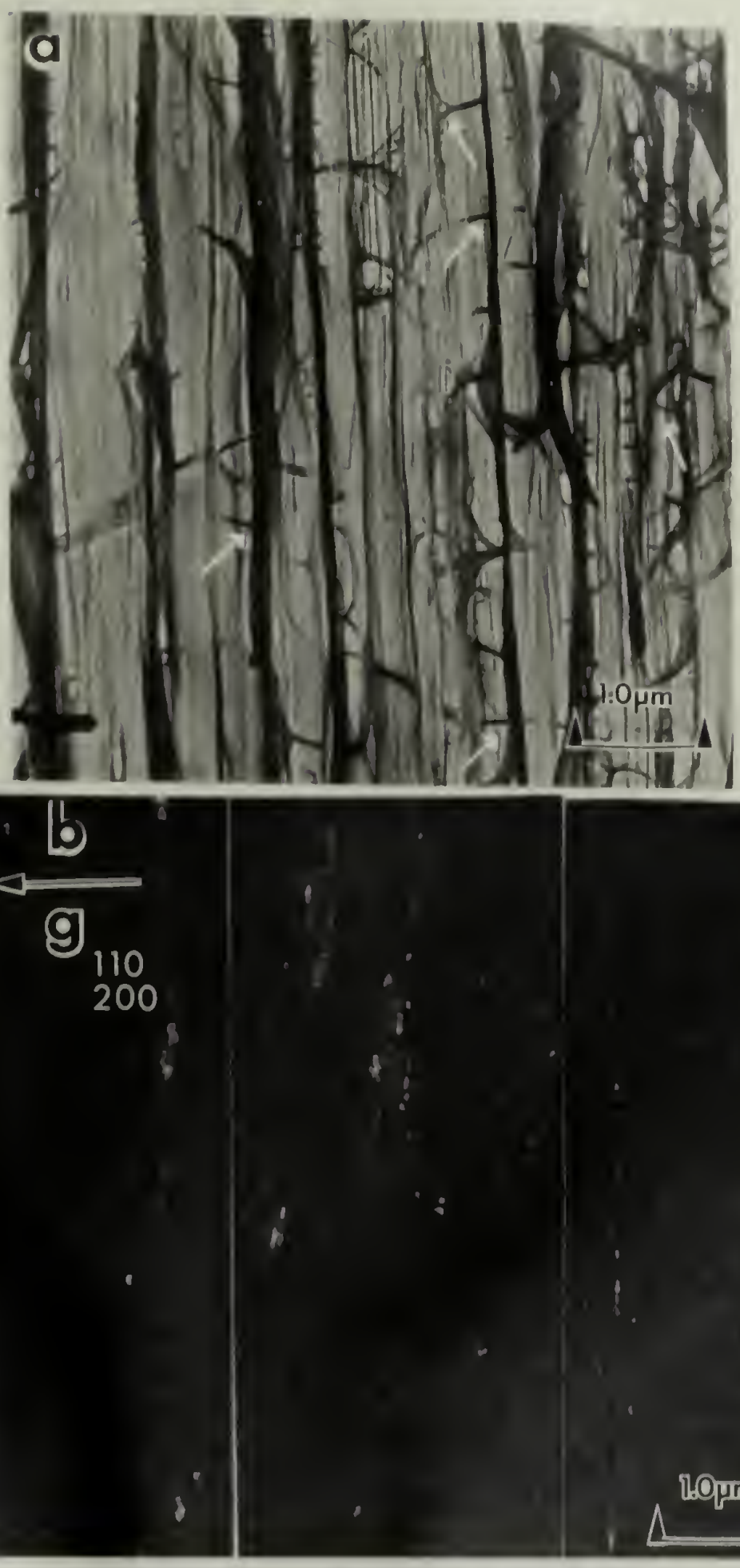

Figure 4.2. CTEM of sample L: (a) Bright field image. Arrows indicate the numerous branches and junctions of the interconnected fibril network. (b) Dark field image using the 110 and 200 reflections.

direction. The fibrils form an interconnected network (see regions indicated by arrows) quite similar to microfibril networks observed in cold drawn PE (7) and reflect the presence of interfibrillar tie molecules in the bulk sample.

Figure 2b is a region of detached fibers imaged in combined 110, 200 CTEM-DF. The crystallites appear both singly and in short sequences along the microfibers. The crystallites average approximately 250 Å in width (i.e., the full width of the microfibril) and have a range of lengths in the fiber direction from 125 to 450 Å. The shortest intervening dark, nondiffracting, regions are about 70 Å. CTEM-DF images exhibit no evidence of extended chain crystals for the L sample. Split films of sample H also consist of ribbons of fine fibrils. There is also the same type of interconnected network as in the L sample. A typical area observed in CTEM-BF is shown in Figure 3.

Figure 4a is a composite of several micrographs of the detached H fibers imaged in CTEM-DF using the combined 110, 200 reflections. Figure 4b is a DF image using the 002 reflection. These micrographs were chosen to illustrate an atypical feature of the morphology. What is in this sample, but not in the L sample, is a small component of long crystals oriented along the microfiber (indicated by white arrows). The domenant structure of the microfibers is, as in the L sample, the approximately 250 Å crystallites appearing singly and in short sequences along the microfibers.

Figure 4.3 CTEM bright field image of Sample H.

Figure 4.4 Composites of several CTEM dark field images of the H sample: (a) 110 and 200 reflections. Arrows point to the long crystals, (b) 002 reflection.

The dark field micrographs of the L and H samples were compared quantitatively by measuring the length of the diffracting crystallites in the fiber direction. Several hundred crystals were counted for each sample. The weight average length, $\bar{\ell}_w^{DF}$, and the number average length, $\bar{\ell}_n^{DF}$, were calculated. The crystal length histograms are shown in Figure 5 and the average sizes are displayed in Table 1. These values are biased toward large crystals since very small crystals, less than about 50 Å, are not resolvable above background in the limited resolution of DF. Sample H has a larger average crystal length than sample L. Figure 6a shows an SAED pattern of sample L. The narrow angular arcing of the 002 reflection indicates that the chain axis is highly oriented in the extrusion direction. The occurrence of the 110 and 200 reflections and the many reflections on the hkO and hkℓ layer lines indicates that the crystallites have fiber symmetry about the chain axis.

Figure 6b is a SAED pattern from the detached high pressure crystallized PE. The rings are not continuous as in a typical powder pattern but are composed of closely spaced discrete spots. Each individual spot originates from a large detached extended chain block. Applying the Scherrer equation to the 002 line widths at half maximum yields crystal sizes along the chain axis of circa 750 Å. This corresponds well with the crystals observed in DF (see Figure 2.4). The SAED patterns from the detached fibrils of

TABLE 4.1

Sample	M_w	Modulus GPa	Crystal Length, Å					SAXS
			Electron Microscopy			WAXD		
			$\bar{\ell}_{DF_N}$ ±30Å	$\bar{\ell}_{DF_w}$ ±30Å	SAED	Cauchy ± 5Å	Gaussian ± 5Å	L±8Å
L	59,000	27	240	270	140	415	290	270
H	200,000	46	340	475	380	450	310	270

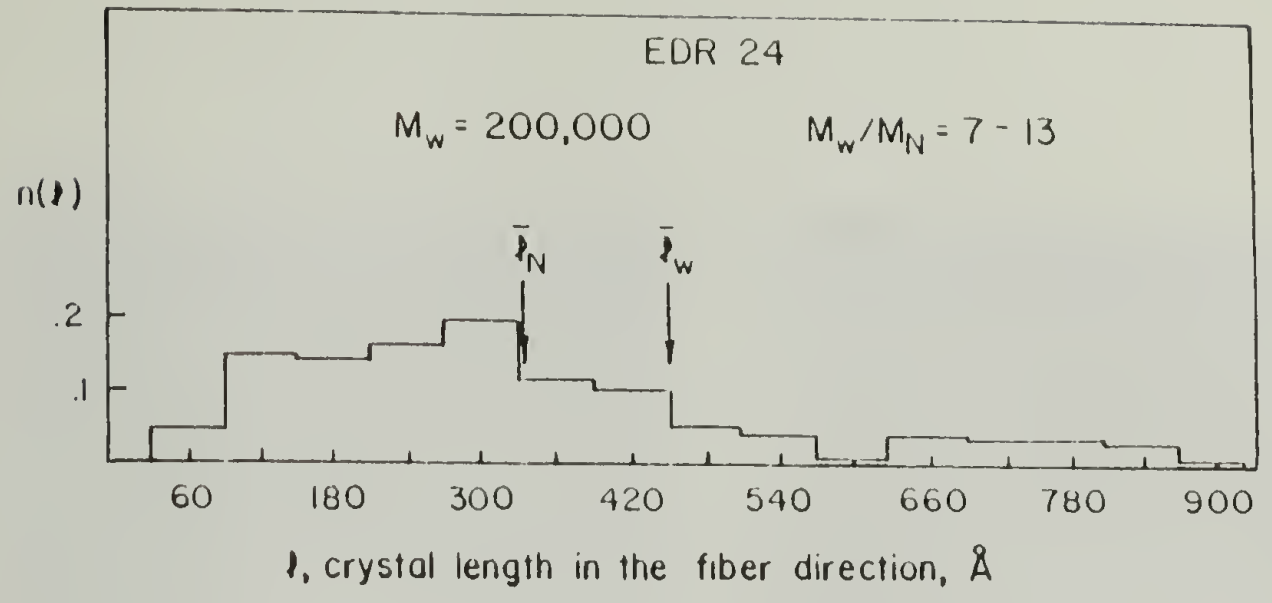

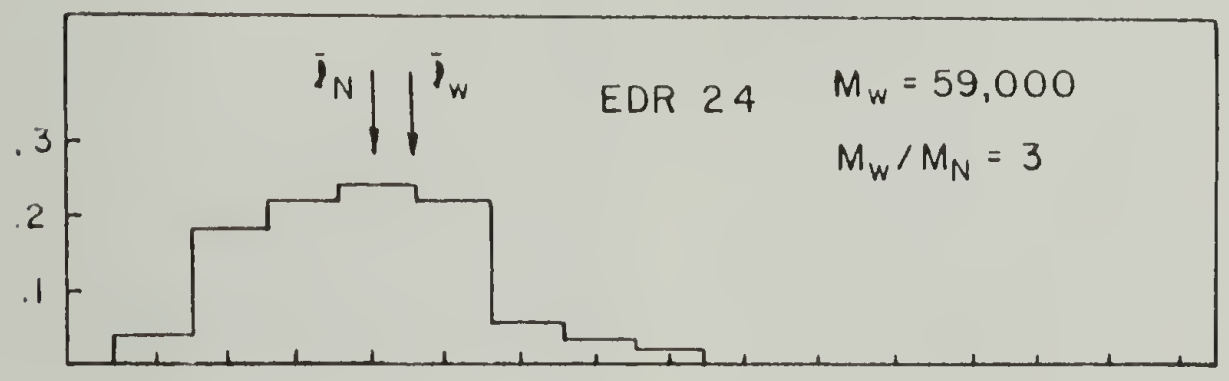

Figure 4.5. Histograms of the fraction of crystals of length l, n(l), plotted vs. length, l as measured by dark field electron microscopy using the 110 and $\bar{2}00$ reflections. The positions of the number average, $\bar{l}_N$, and weight average, $\bar{l}_W$, crystal length are indicated on the histogram.

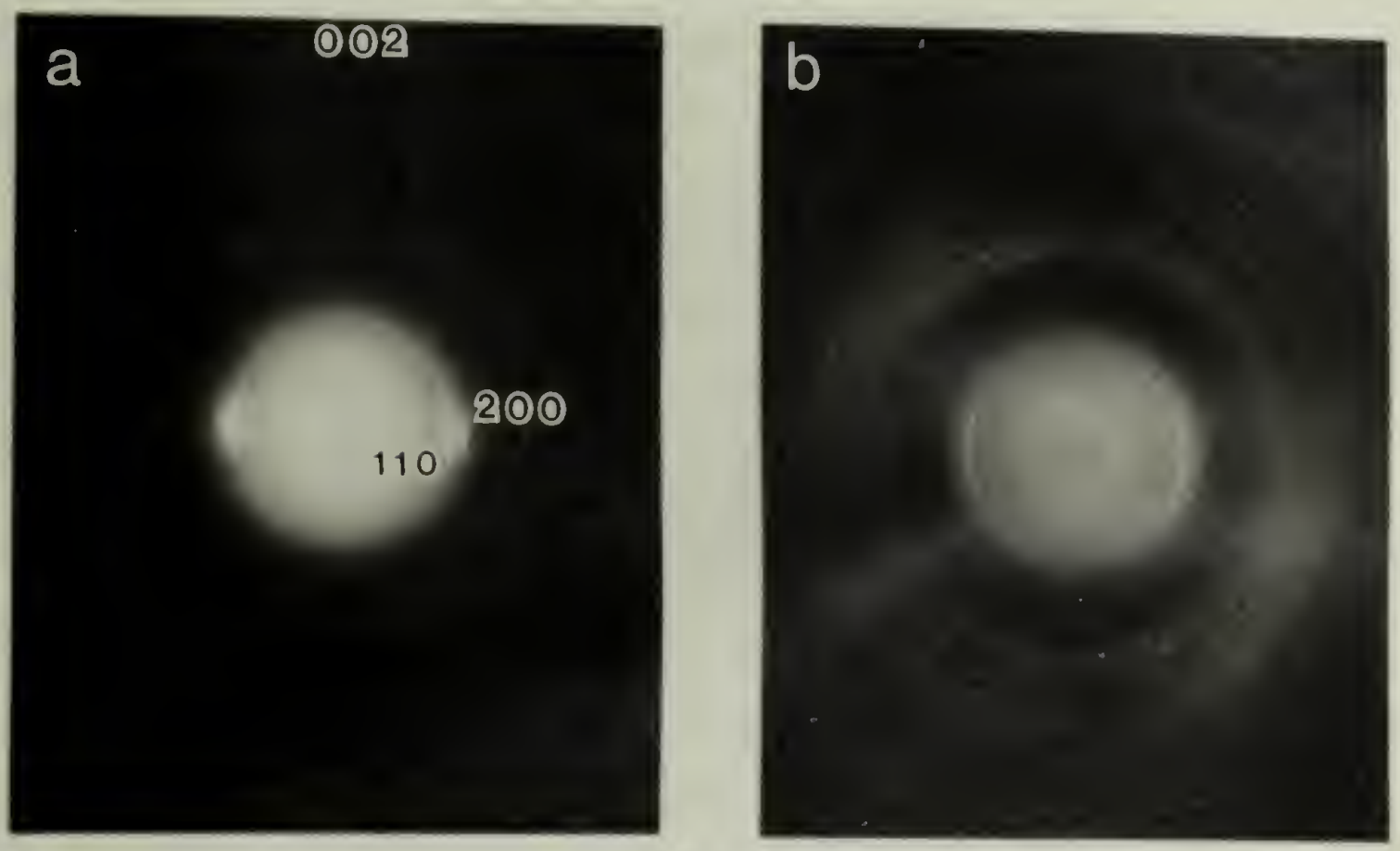

Figure 4.6 Selected area electron diffraction patterns (Central portions photographically dodged to better contrast 110 and 200 reflections): (a) detached fibrils of Sample L and (b) detached high pressure crystallized PE.

sample H are very similar to Fibure 6a. Figure 7a, b shows microdensitometer line profile traces of the 002 reflections. Line breadth analysis using the full width at half maximum, without any peak width corrections, yields an average crystal length of 140 Å along the chain direction for sample L and 380 Å for sample H. Line width variations of different patterns were about $\pm$ 30 Å.

Before interpreting these results, the validity of using our DF imaging and electron diffraction techniques to characterize the crystalline order of fibers must be assessed; in particular the effects of the sample preparation techniques, since fiber elastic bending and distortion of the DF images must be considered.

It has been shown that simple elastic bending of PE single crystals can account for the small crystal size observed by line broadening (87). Diffraction and dark field imaging techniques give a lower limit to crystal size since simple elastic bending of the crystal lattice can reduce the size of the effective diffracting regions. A determination of the content of long crystals must consider the effects of bending on both the 110, 200 and 002 DF images and the line width of the 002 reflection.

The influence of elastic distortion on the observed crystallite size was explored using STEM annular DF. A pair of DF images were taken with the specimen tilted by approximately 1^{o} with respect to the incident beam direction (see

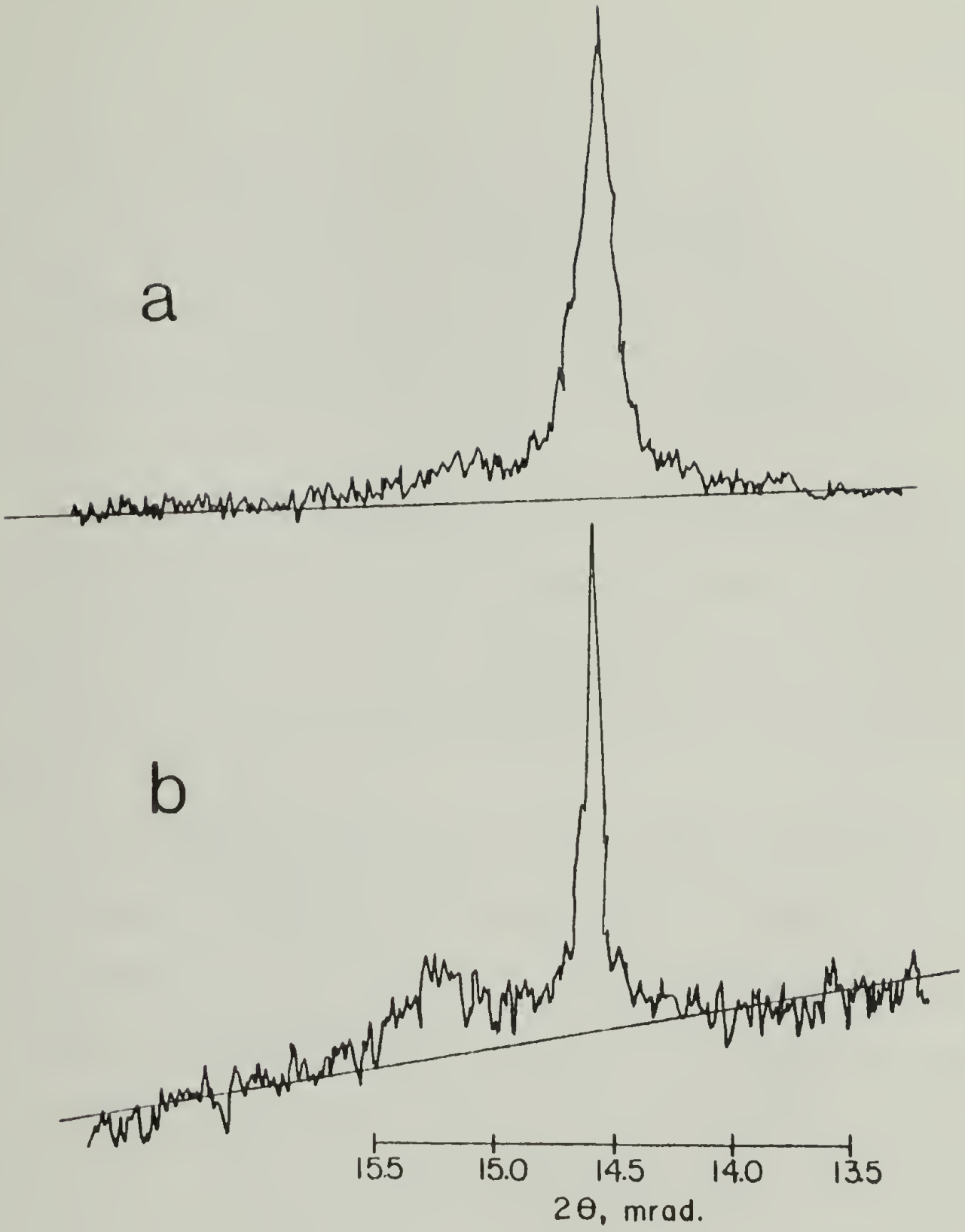

Figure 4.7. Electron diffraction profiles of the (002) reflection: (a) L sample and (b) H sample.

Figure 8).

For accurate comparison of successive pictures of the same area under different conditions, a transparent sheet was used where bright diffracting regions from one picture were marked. The transparent sheet could then be superposed on the tilted micrograph and in that way correspondence or non-correspondence of about several dozen crystals per image was checked.

If some of the fibers were long continuous crystals, the diffracting regions should have translated in unison along the fiber. Instead, the image changes are not correlated with the tilt indicating that only short crystals are present.

A complete series of micrographs over various tilting angles would be required to completely assess all the elastic bending effects, as well as possible presence of large tilt angle kink bands. Because of radiation damage a complete tilt series, in a given area, is not possible. Pairs of DF images have however been obtained for large (35^{o}) tilts as shown in Figure 9 where no systematic correlation is found.

Plastic distortion of any extended chain crystals due to sample preparation does not appear significant for four reasons:

1. When the freeze fracture/detachment replication technique was applied to high pressure crystallized PE, long crystals were observed by DF imaging and

Figure 4.8 Tilt pair of the H sample using STEM annular DF and 1 degree tilt. The two negatives were printed adjacent to each other.

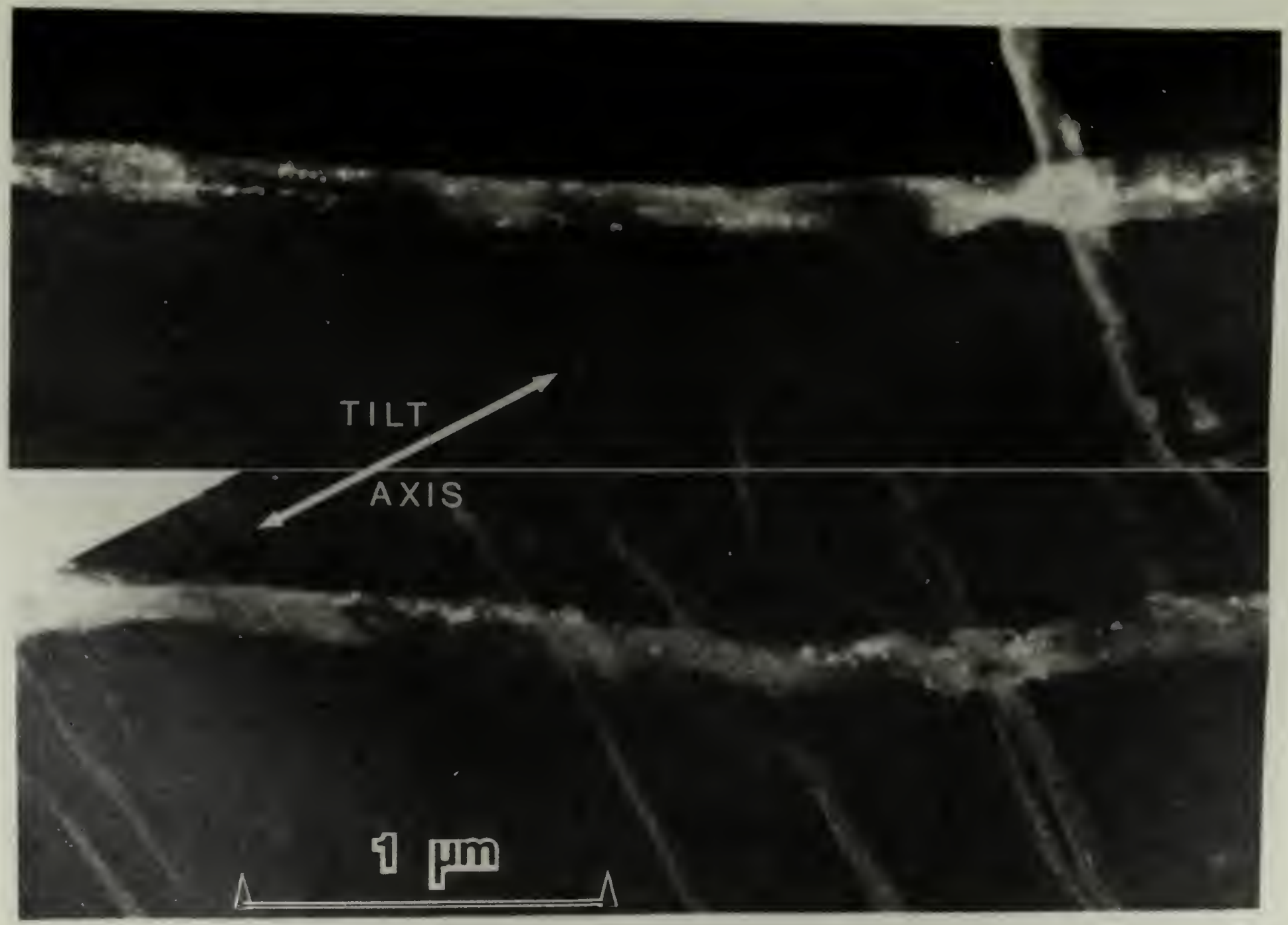

Figure 4.9 Tilt pair of the H sample using STEM annular DF and 35 degree tilt.

electron diffraction line broadening.

2. Since some long crystals have been found in the H sample their absence in the L sample suggests a real effect.

3. Thin fibers dispersed by nitric acid etching showed the same size and orientation of the crystallites as detachment replicated fibers.

4. Dark field imaging with 110, 200 or 002 reflections yields the same crystallite size.

Nitric acid etching has been shown not to change the size of extended chain crystals in high pressure crystallized PE (88) and not to affect the elementary fibrils of solution grown fibrillar PE crystals (89). Since mechanical deformation is not used in preparing the etch fragments and the results from the techniques agree, both methods should be considered valid for revealing the true morphology of solid state extruded PE. Moreover, the 2-point SAXS patterns and WAXD line broadening observed for both molecular weight samples supports the DF microscopy observation that the both samples consist mainly of small crystallites with adjacent intervening non-crystalline regions.

4.2.2 Wide angle x-ray diffraction. The corrected (002) WAXD profiles are shown in Figure 10a and 10b for the L and H samples respectively. Assuming Gaussian peak shapes yields crystal coherence lengths of 290 Å and 310 Å while a Cauchy

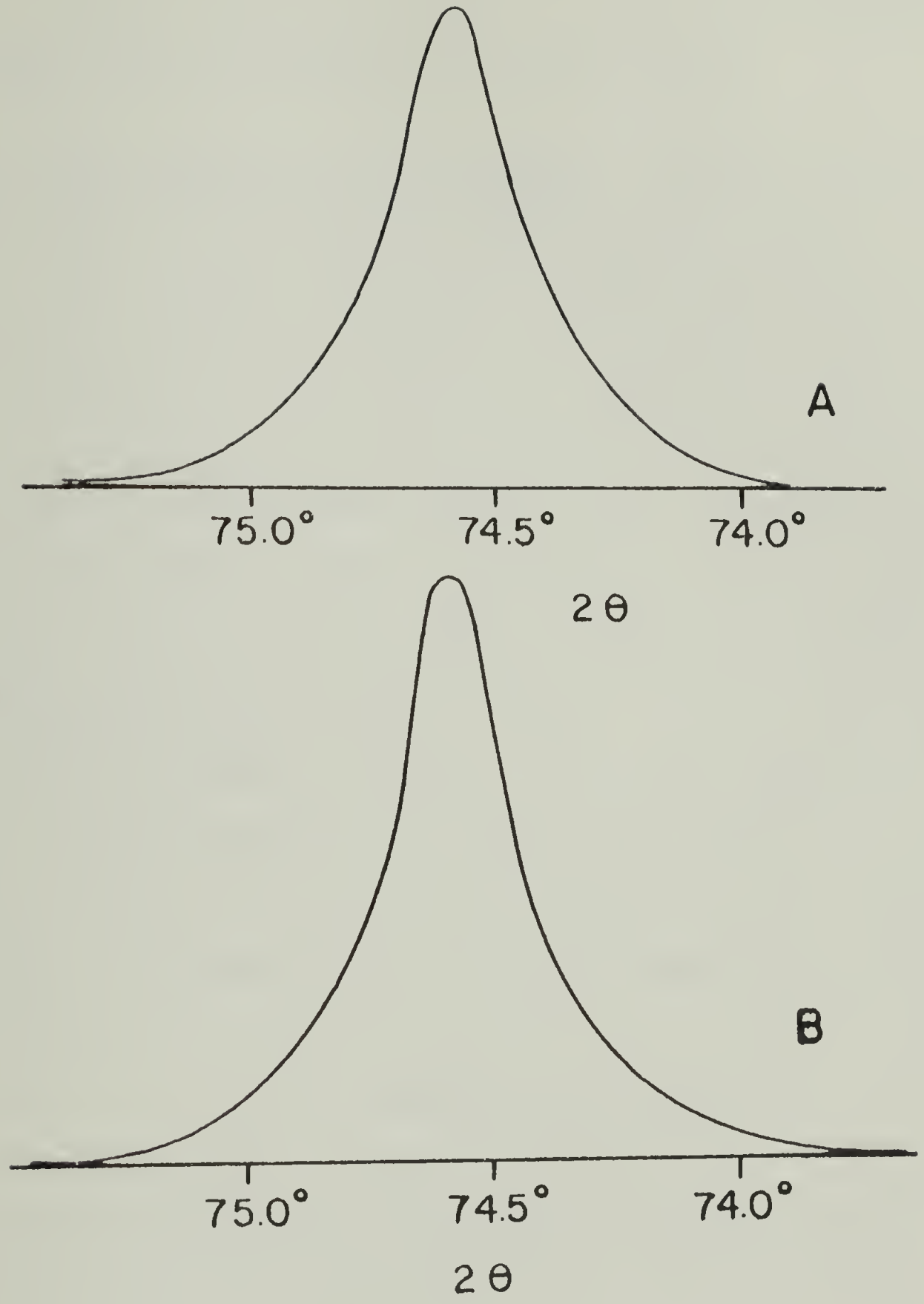

Figure 4.10. Wide angle x-ray diffraction profiles of the (002) reflection: (a) L sample and (b) H sample.

shape gives 415 Å and 450 Å respectively for the L and H samples. These values are given in Table 1 for comparison with the SAED and DF measures of crystal length.

4.2.3 Small angle x-ray scattering. Figure 11a and 11b are small angle x-ray scattering isointensity contour plots for the L and H samples. The data has been background corrected and normalized to the same sample thickness. Each contour line is drawn at twice the intensity of the previous line. The outside line on each sample is for intensity of 128 corrected counts. Both samples show a 2-point pattern of intensity on the meridian that is typically observed for conventionally drawn polymer fibers (90,91). The long period calculated by applying Bragg's law to the position of the peak intensity maximum is approximately 270 Å for both samples. Figure 12 is a plot of intensity vs. 2θ along the meridian. The meridional integral breadth ($\Delta\beta_1$) is given by:

$$\Delta\beta_1 = \frac{2}{I(S_1^*,0)} \int_{S_1^*}^{\infty} I(S_1,0)\,dS_1 \qquad (4.1)$$

The average width of the microfibers may be measured from the integral breadth of the peak in the S_2 direction by:

$$\Delta\beta_2 = \frac{1}{I(S_1^*,0)} \int_{-\infty}^{+\infty} I(S_1^*,S_2)\,dS_2 \qquad (4.2)$$

where $S_1^*,0$ is the position of the intensity maximum.

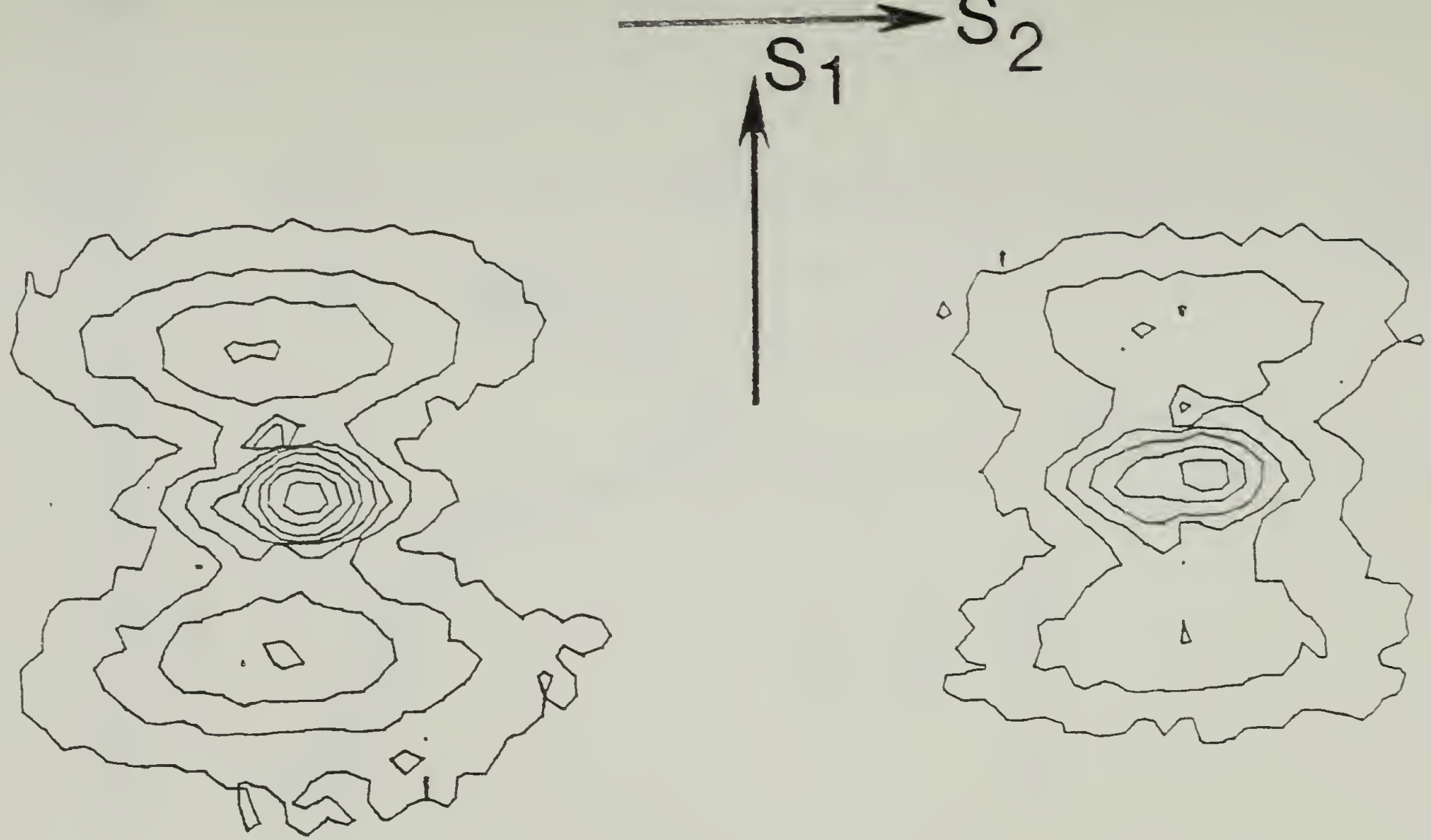

Figure 4.11 Two dimensional isointensity contour plots of the small angle x-ray scattering patterns: (a) L sample, (b) H sample, with the definition of $\underline{S}_1$ and $\underline{S}_2$ directions.

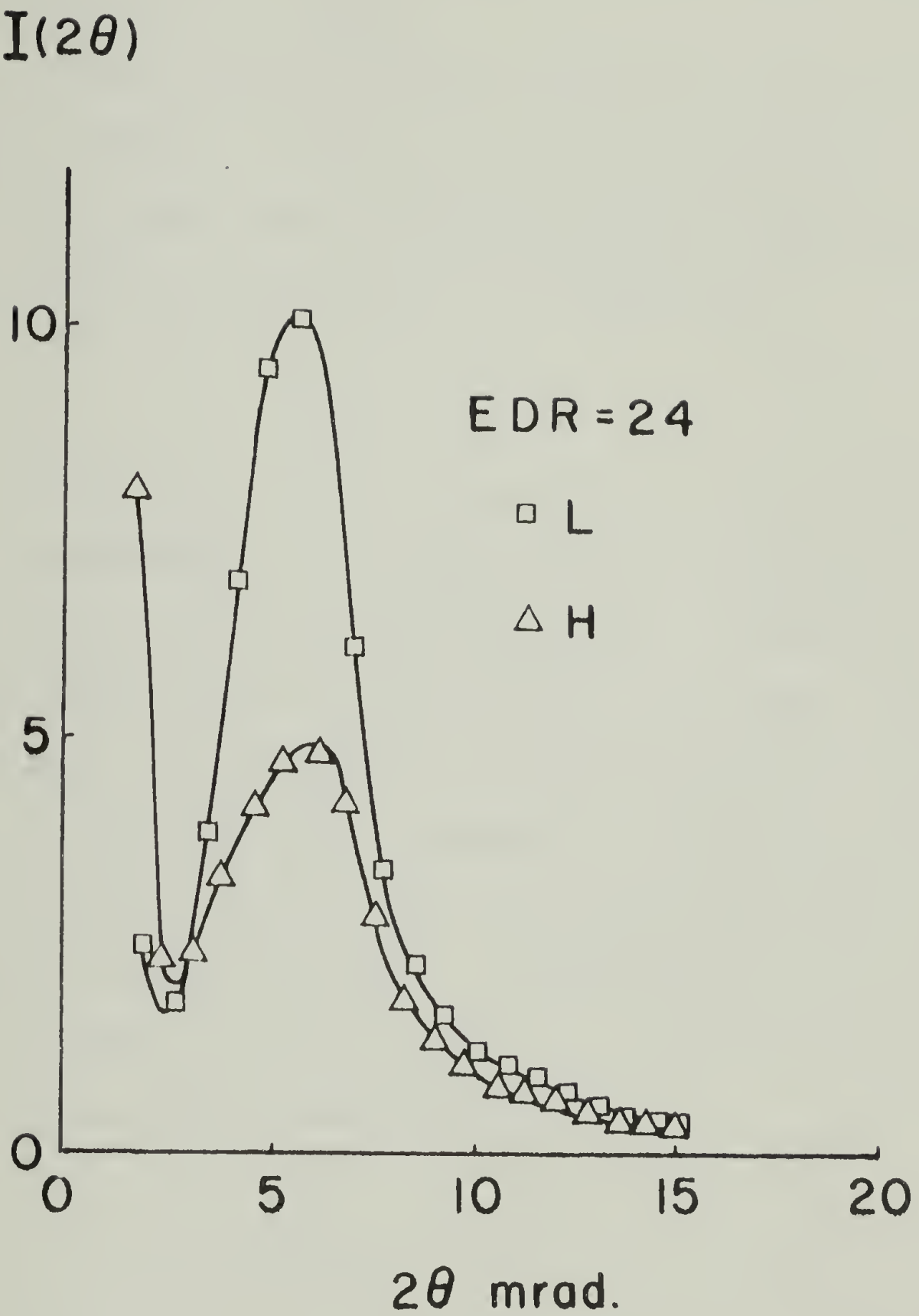

Figure 4.12 Relative small angle scattering intensity versus scattering angle 2θ in the meridial, $S_{\parallel}$, direction for the: (a) L sample and (b) H sample.

For the L sample the integral breadths in the S_1 and S_2 directions are 4.3 and 9.8 mrads. and for the H sample they are 5.9 and 11.7 mrads.

The mean square density fluctuation for a two phase system of crystals of density ρ_c and non-crystalline regions of density ρ_a with sharp interfaces between the phases and volume fraction crystallinity ϕ is given by:

$$\Omega = (\Delta\rho)^2 \phi(1-\phi) \qquad (4.3)$$

where $\Delta\rho = \rho_c - \rho_a$. If ϕ is known we can calculate $\Delta\rho$. However, measurement of ϕ depends on the crystalline and amorphous density being known constants. Differential scanning calorimetry can be used to obtain the weight fraction crystallinity, χ, by assuming a constant heat of fusion for the pure crystalline phase. However, a defect crystalline phase will have a lower density and a heat of fusion less than that of perfect crystals. Conversion of χ to ϕ also requires assumed values of ρ_c and ρ_a. ϕ can be determined from the bulk sample density, ρ;

$$\phi = \frac{\rho-\rho_a}{\Delta\rho} \qquad (4.4)$$

but again ρ_c and ρ_a must be known.

Fischer et al. have addressed these problems for drawn polyethylene (92, 93) and have shown that $\Delta\rho$ can be determined by combining equations 4.3 and 4.4 to give:

$$\Delta\rho = (\Omega + (\rho_c - \rho)^2)/(\rho_c - \rho) \qquad (4.5)$$

Now if ρ_c is assumed approximately constant, $\Delta\rho$ may be calculated from the measured ρ and Ω of the fiber. (Fischer et al. (92,93) have shown that a constant ρ_c is a good assumption since the d_{110} and d_{200} Bragg spacings of polyethylene change only about 0.5% during drawing and annealing). We therefore assume that the crystal density is constant at 0.997 gm/cm^3 (94).

Values of Ω, ρ and $\Delta\rho$ are given in Table 2. $\Delta\rho$ is 0.024 and 0.023 for the L and H samples respectively. The H sample has approximately a 4% lower $\Delta\rho$ than the L sample. The assumption of sharp interfaces between phases, which is inherent in equation 4.3, was experimentally verified by plotting IS^4 vs. S^2 which indicated that the scattered intensity obeyed Porod's law (95) within experimental limits for the L and H samples.

4.3 Discussion

Four methods have been applied to studying crystal size and connectivity to determine which morphological models for the structure of solid state extruded PE are most appropriate. DF electron microscopy was used to directly image the crystalline regions to investigate their distribution of sizes and shapes. Wide angle x-ray and selected area electron diffraction line breadth analysis measures the weight

TABLE 4.2

Sample	$Q(\frac{gm^2}{cm^6})$	ρ $(\frac{gm}{cm^3})$	$\Delta\rho$ (gm/cm^3)
L	1.5×10^{-5}	.974	.024
H	1.2×10^{-5}	.975	.023

average axial crystal size from coherently scattering (002) lattice planes. X-ray diffraction is a volume average over several mm^3 of the bulk sample while electron diffraction averages over a relatively small area circa 50 m in diameter of the detached fibers. SAXS yields the long period of crystals within periodic macrolattices from the low angle peak position while peak breadths indicate relative changes in size and order of the macrolattices. Finally, the density difference between the crystalline and non-crystalline regions can be calculated from the SAXS invariant. All these techniques reveal important information about the fiber microstructure. While differing in the type of average (weight vs. number) and sensitivity a combined synthesis of the observed quantities reveals important measures of crystal order and connectivity via the intervening non-crystalline regions.

The DF, x-ray and electron diffraction measures of crystal length are shown together in Table 1. The SAXS long period of 270Å for both samples is within the range of crystal lengths measured by DF microscopy ($\bar{\ell}_n^{DF}$ = 240Å, $\bar{\ell}_w^{DF}$ = 270Å) for the L sample. The long period for the H sample is less than the DF measurements ($\bar{\ell}_n^{DF}$ = 340Å, $\bar{\ell}_w^{DF}$ = 475Å).

1. We can suggest two reasons for this discrepancy: L_{SAXS} is usually interpreted as the number average crystal thickness, $\bar{\ell}_c$ plus the number average amorphous thickness, $\bar{\ell}_a$. The long period will be

sensitive to the crystal and non-crystal length distribution functions. Crist has reviewed previous model structure calculations and has shown that this interpretation can lead to errors of ± 30% depending on the macrolattice distribution statistics (96).

2. The longer crystals ($\ell > 500$ Å) in the H sample disturb the macrolattice order and hence, broaden the peak without changing the position of the maximum, i.e., do not affect L_{SAXS}. However, all diffracting crystals, without regard to their presence in a macrolattice, are included in calculating $\bar{\ell}_n^{DF}$. Therefore, it is not surprising that $\bar{\ell}_n^{DF} > L_{SAXS}$ for the H sample.

The WAXD coherence lengths are slightly greater than the long period for the Gaussian and Cauchy peaks with the H sample having a slightly greater value in both cases. This is reasonable because WAXD will give a larger value since it is a weight average of the crystal length while the long period is a measure of periodicity in the scattering macrolattices. The electron diffraction coherence length for the H sample (380 Å) is almost 3 times the value for the L sample (140 Å). This could be because of many long crystals which were contributing to the line breadths in the 50 μm areas selected for electron diffraction for the H sample. The low value of

140 Å may be because of distortion during sample preparation since this value is half that obtained by x-ray diffraction (280 Å).

The SAXS peak shapes indicate differences in macrolattice order between the H and L samples. The integral breadth in the $\bar{S}_1$ direction (see Fig. 11) of SAXS patterns from highly oriented macrolattices as in Figures 11a, b may be expressed as (42)

$$\Delta\beta_1 = \frac{\lambda}{L} \left(N^{-2} + \left(\frac{n\delta L}{L}\right) + (n g_1)^4\right)^{1/2} \qquad (4.6)$$

where N is the weight average number of scattering units per macrolattice, δL is the long period fluctuation between different macrolattices, g_1 is the paracrystallinity of the macrolattice in the fiber direction and n is the order of the reflection. Three orders of reflection are required to quantitatively separate the three broadening mechanisms. Since only a weak second order reflection in the $\bar{S}_1$ direction is observed for the H and L samples, the SAXS integral breadths can only be discussed qualitatively.

The 37% increase in $\Delta\beta_1$ on going from the L to H sample represents a decrease in macrolattice perfection. This increase in breadth is consistent with the DF observations since occasional long crystals will reduce the effective macrolattice size, i.e., decrease N and increase the paracrystallinity of the macrolattice, g_1, while a broader distribution of crystal sizes would increase δL.

The integral breadth of the SAXS peak perpendicular to the fibers, $\Delta\beta_2$, can be interpreted in terms of microfibril radii by the equation (97):

$$<R>=\frac{0.52\lambda}{\Delta\beta_2} \tag{4.7}$$

where

$$<R>=\bar{R}^4/\bar{R}^3; \tag{4.8}$$

the ratio between the 4th and 3rd moments of the microfibril radius distribution function. The relatively small 20% increase of $\Delta\beta_2$ for the H sample can be interpreted as a slight thinning of the microfibrils or a slight change in the microfibril width distribution function.

The DF microscopy, electron and x-ray diffraction line breadth measurements and small angle x-ray scattering agree with previous results for drawn fibers indicating that the crystalline regions are small adjacent blocks along the microfibers with intervening non-crystalline regions between them. The major difference in the crystalline component of the microfibrils for the two samples is the broad size distribution for the H sample with a tail of long crystals (see Figure 5).

The structure of the non-crystalline regions along the microfibers is greatly changed during solid state extrusion since $\Delta\rho$ is very much less (0.024 gm/cm^3 for the L sample and 0.023 gm/cm^3 for the H sample) than for undeformed

melt crystallized PE ($\Delta\rho$ is 0.14 gm/cm^3 assuming ρ_c = 1.0 and ρ_a = 0.86 gm/cm^3). The enormous decrease in $\Delta\rho$ for solid state extruded PE indicates that the non-crystalline density has increased since the crystalline density can be assumed nearly constant. The noncrystalline phase density increase is the result of more oriented, hence densely packed, tie molecules. The approximately 20% decrease of the mean squared density fluctuation, corresponding to a 4% decrease in $\Delta\rho$, for sample H over sample L may account for the nearly 40% higher tensile modulus that is observed for the H sample.

Fischer et al. (92,93) have measured $\Delta\rho$ for a series of hot drawn and post-drawn annealed PE fibers using a slit collimation system. The smallest value of $\Delta\rho$ (0.075 gm/cm^3) was found for a fiber drawn to 8X at 80^{o}C at a strain rate of 10 mm/min. with no post-draw annealing. This is a density difference between the crystalline and non-crystalline phases approximately 220% higher than for our high modulus solid state extruded fibers of EDR 24.

Wu, Simpson and Black (43) have recently qualitatively correlated a 10 fold decrease in the total scattered intensity with increasing tensile modulus and strength for a series of hot drawn PE fibers. A combination of microdensitometry and visual observations were used to estimate the intensity of the small angle maximum recorded on film for samples of various draw ratios. This type of estimate is a

poor substitute for the integrated absolute intensity invariant that we have calculated. The absolute invariant allows quantitative comparison of the structure of the important non-crystalline regions for samples of different thermal and mechanical histories.

C H A P T E R V

CHANGES IN MORPHOLOGY WITH EXTRUSION DRAW RATIO

5.1 Introduction

The aim of this chapter is to follow changes in morphology with extrusion draw ratio from EDR 12 to 36. Over this range of draw ratio the tensile modulus increases nearly linearly with EDR significantly past the range of tensile moduli generally achievable by cold drawing. By studying this systematic series of solid state extruded samples changes in crystallite size, orientation and axial connection in the non-crystalline regions can be correlated with the improvement in tensile modulus.

5.2 Results

5.2.1 Moduli. The tensile modulus increases almost linearly with EDR from 10 GPa. at EDR 12 to 40 GPa. at EDR 36 as shown in Table 1.

5.2.2 Differential scanning calorimetry (DSC). The weight percent degree of crystallinity, X, increases with EDR from 73 ± 5 at EDR 12 to 82 ± 5 at EDR 24. The EDR 36 value is 83 ± 5. All melting curves were nearly identical with the

Table 5.1

EDR	Tensile Modulus (Gpa.)	$(gm^2{}^Q/cm^6) \times 10^{-5}$	$\rho (gm/cm^3)$	$\Delta\rho (gm/cm^3)$
12	10	3.90	.968	.030
24	27	1.50	.974	.024
36	40	.11	.975	.022

Table 5.2

	Dark Field		L^{WAXD}		SAXS
EDR	$\bar{\ell}_n \pm 30\text{Å}$	$\bar{\ell}_w \pm 30\text{Å}$	Gaussian	Cauchy $\pm$ 5Å	$L \pm 8\text{Å}$
12	240	270	280	390	340
24	240	270	290	415	270
36	310	390	330	490	245

peak position at 137 $\pm$ 1°C. A typical scan, for the EDR 24 sample, is shown in Figure 1.

5.2.3 Density. Sample densities, ρ, are given in Table 1. They are 0.968, 0.974 and 0.975 gm/cm^3 for EDR's 12, 24 and 36 respectively.

5.2.4 Electron microscopy. Figure 2a is a CTEM BF image showing a typical area of the EDR 12 sample using the detachment replication procedure. The detached PE is oriented in the extrusion direction. Rather thick coarse fibrils are observed which taper to finer fibers at their ends (see arrows A and B in the figure). Many fine microfibrils protrude from the sides and ends of the larger fibril structures (see unlabeled arrows). These protruding microfibrils are approximately 250 to 300 Å in diameter. Thin highly aligned fibers and microfibers 250 to 300 Å in diameter are also visible in this figure.

Figure 2b is a CTEM BF detachment replica micrograph of the EDR 24 sample. There are a number of 0.2-0.3 μm. wide fibrils and fine microfibrils approximately 250 Å wide. The wider fibrils have become more highly aligned and uniform in diameter than the coarse fibrils in the EDR 12 sample. The lower contrast background is from the replica of the fracture surface showing a highly aligned microfiber structure. The microfibers appear to be longer and better aligned in this sample compared with the EDR 12 sample. The

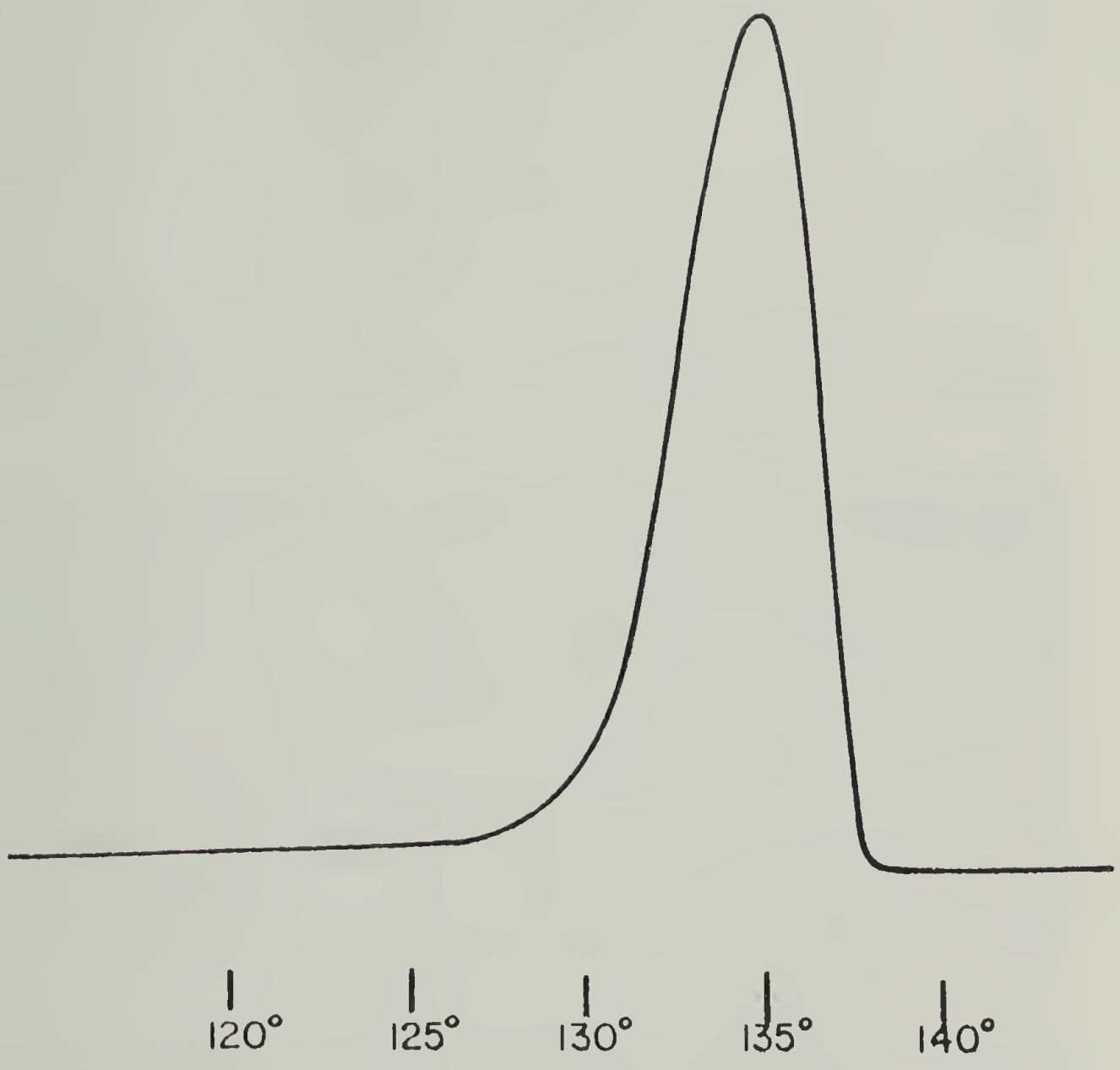

Figure 5.1. DSC scan of the EDR 24 sample. Heating rate was 10^{o}C/minute.

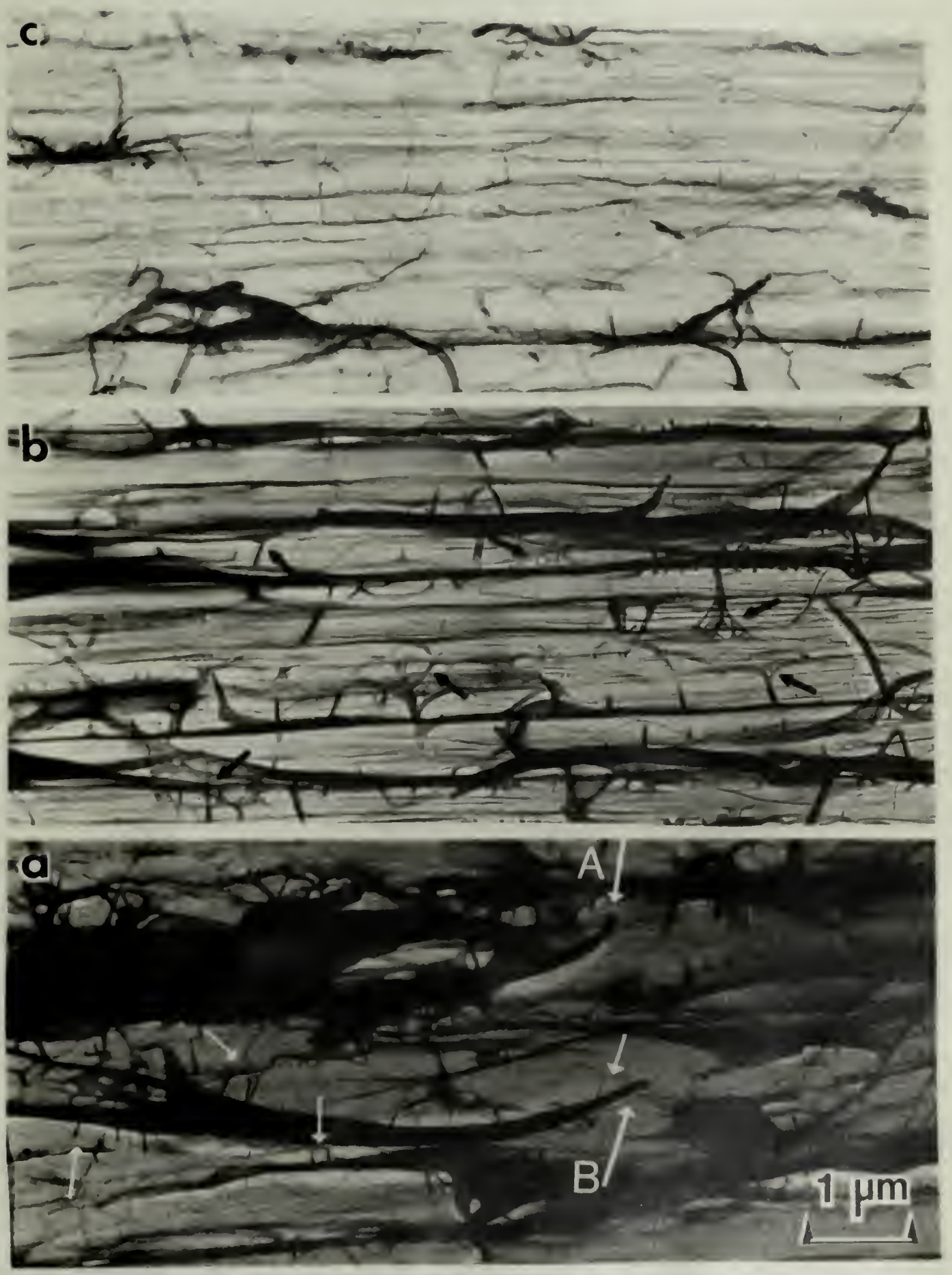

Figure 5.2. Bright field transmission electron micrographs of detachment replicated polyethylene fibers: (a) EDR 12, (b) EDR 24 and (c) EDR 36. The extrusion direction is horizontal.

fibrils form an interconnected network (see regions indicated by arrows) quite similar to microfibril networks recently observed in cold drawn PE(7).

Figure 2c shows the CTEM BF image of the detachment replicated EDR 36 sample. The alignment of the microfiber structures appears to be almost identical to the EDR 24 sample. Generally there appear to be more fine fibrils of 200 Å diameter and less coarse fibrils 0.2 to 0.3 μm wide. The size of the fibrils on these fracture surfaces may depend on the distribution of the weakest lateral connections between the fibers, which break during fracture to reveal the underlying morphology.

Electron diffraction patterns from the detached fibrils of the 12, 24 and 36 EDR samples are shown in figure 3a, b, and c respectively. All the electron diffraction patterns were obtained from areas approximately 50 μm in diameter as defined by the incident beam diameter. The patterns were recorded from areas that were not previously damaged at a electron radiation dose of less than 10% of the dose that destroys sample crystallinity. All the patterns show typical fiber symmetry with narrow arcing of the 002 reflection which indicates that the chain axis is highly oriented in the extrusion direction. The layer lines become more discrete and the 002 orientation increases significantly from the 12 to 24 EDR sample. The orientation of the 36 EDR sample is only slightly greater

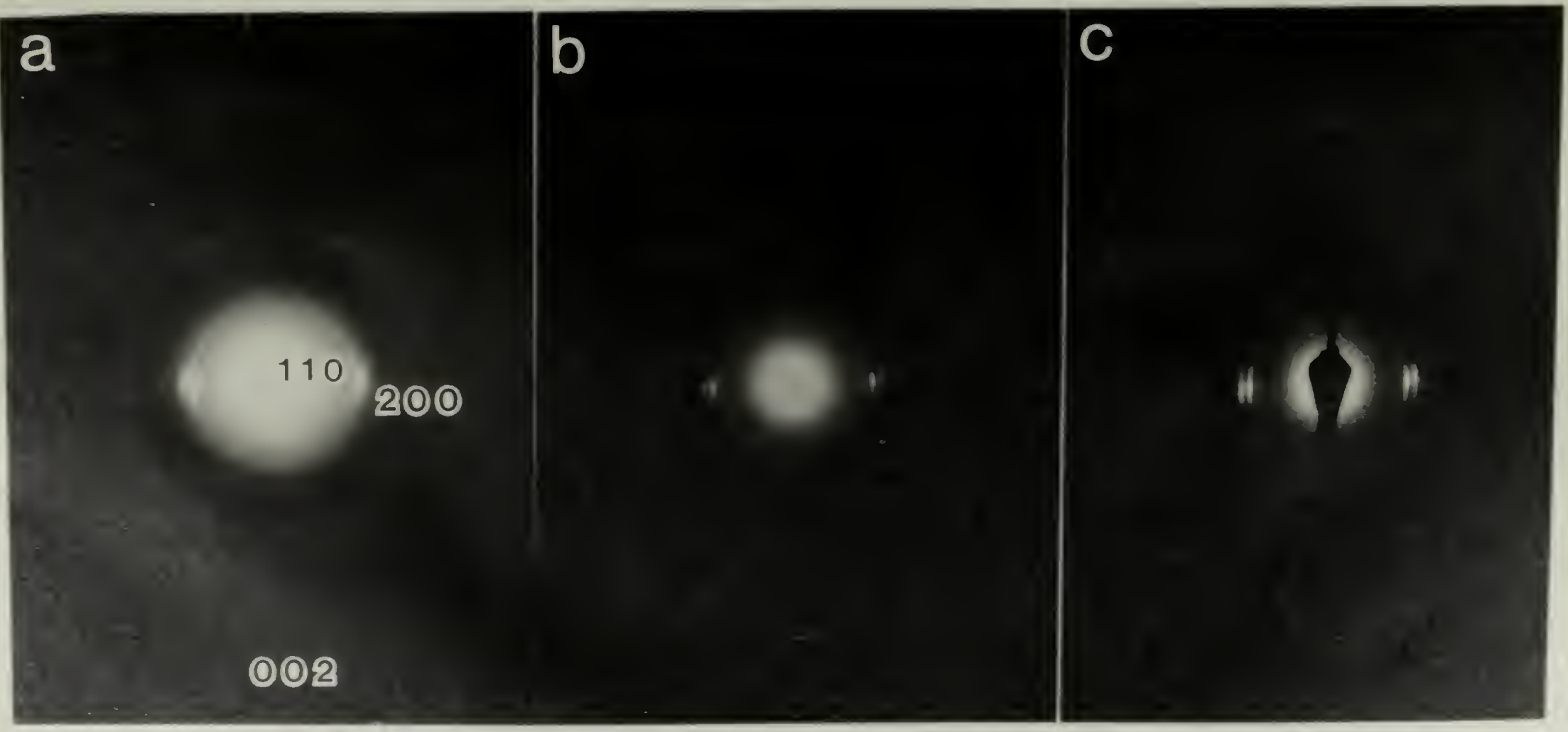

Figure 5.3 Electron diffraction patterns from the detached fibers: (a) EDR 12, (b) EDR 24, and (c) EDR 36.

than that of the 24 EDR sample.

CTEM-DF images of the detached fibers were obtained using the 110 and 200 reflections. A typical image for the 36 EDR sample is shown in Figure 4. Small crystallites the full width of the microfibers occur singly or in sequences with nondiffracting regions approximately 70 Å thick between them. Most of the crystal lengths in the fiber direction range from about 100 to 600 Å. The crystal length distributions were studied quantitatively by measuring the lengths of the sharp, in focus, crystals. The results are shown as crystal length histograms in Figure 5 where the fraction of crystals of length l, n(l), is plotted versus l. Over 100 crystals were counted for each sample. The number average, $\bar{l}_N^{DF}$, and weight average, $\bar{l}_w^{DF}$, crystal lengths are indicated on the figure and summarized in Table 2. The calculations slightly overestimate the average crystal length since small crystals, less than about 50 Å in diameter, are not counted since they are hardly distinguishable from the background at this resolution. The histograms show the crystal length distributions shifting to longer crystals with increasing EDR. The 36 EDR distribution has a tail of long crystals with 900 Å as the longest length measured.

5.2.5 Wide angle X-ray diffraction. Figure 6 shows wide angle X-ray diffraction patterns obtained with the Statton

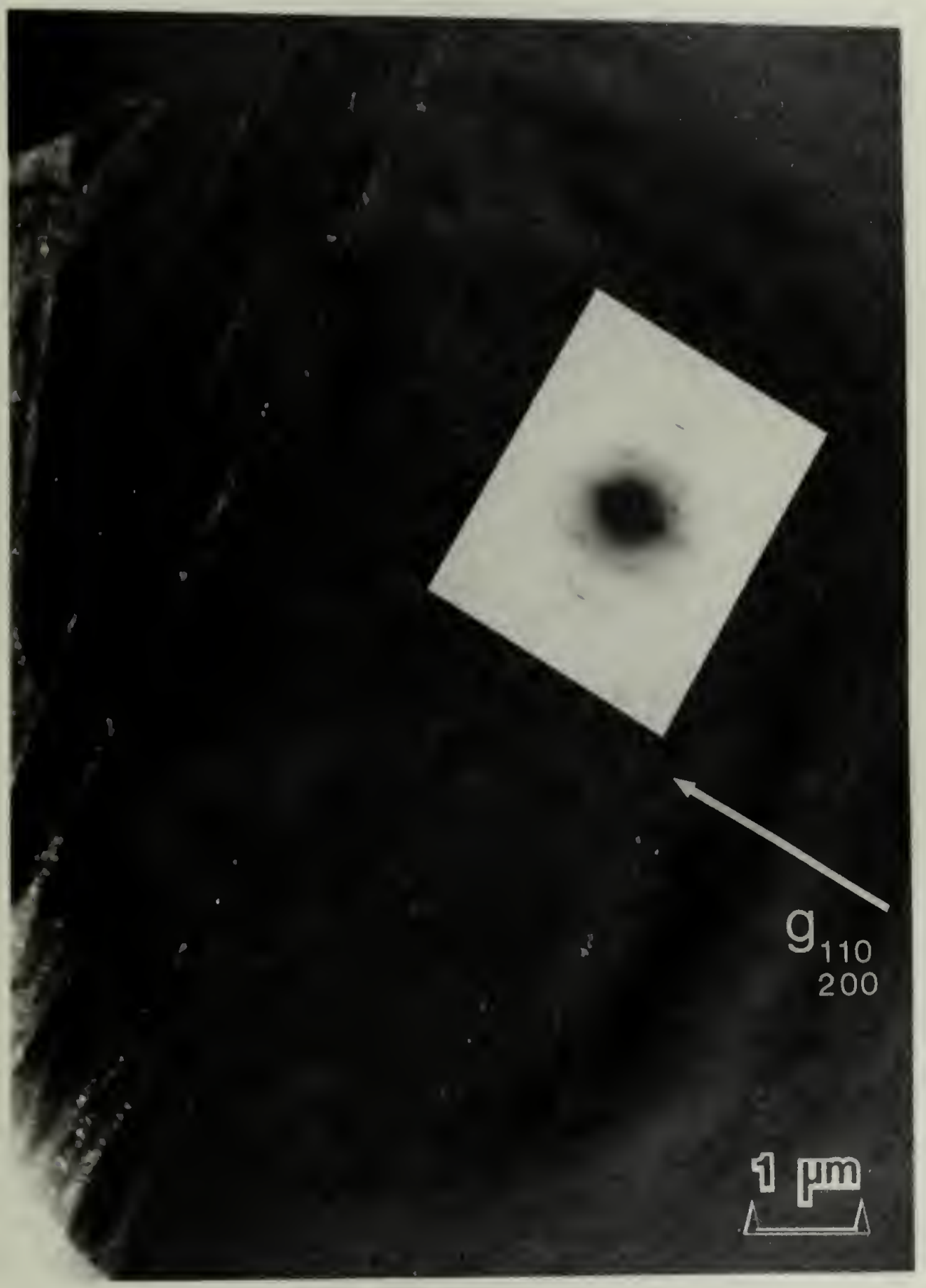

Figure 5.4. Dark field transmission electron micrograph, using the 110 and 200 reflections, of detached fibers of the EDR 36 sample. Inset is the electron diffraction pattern.

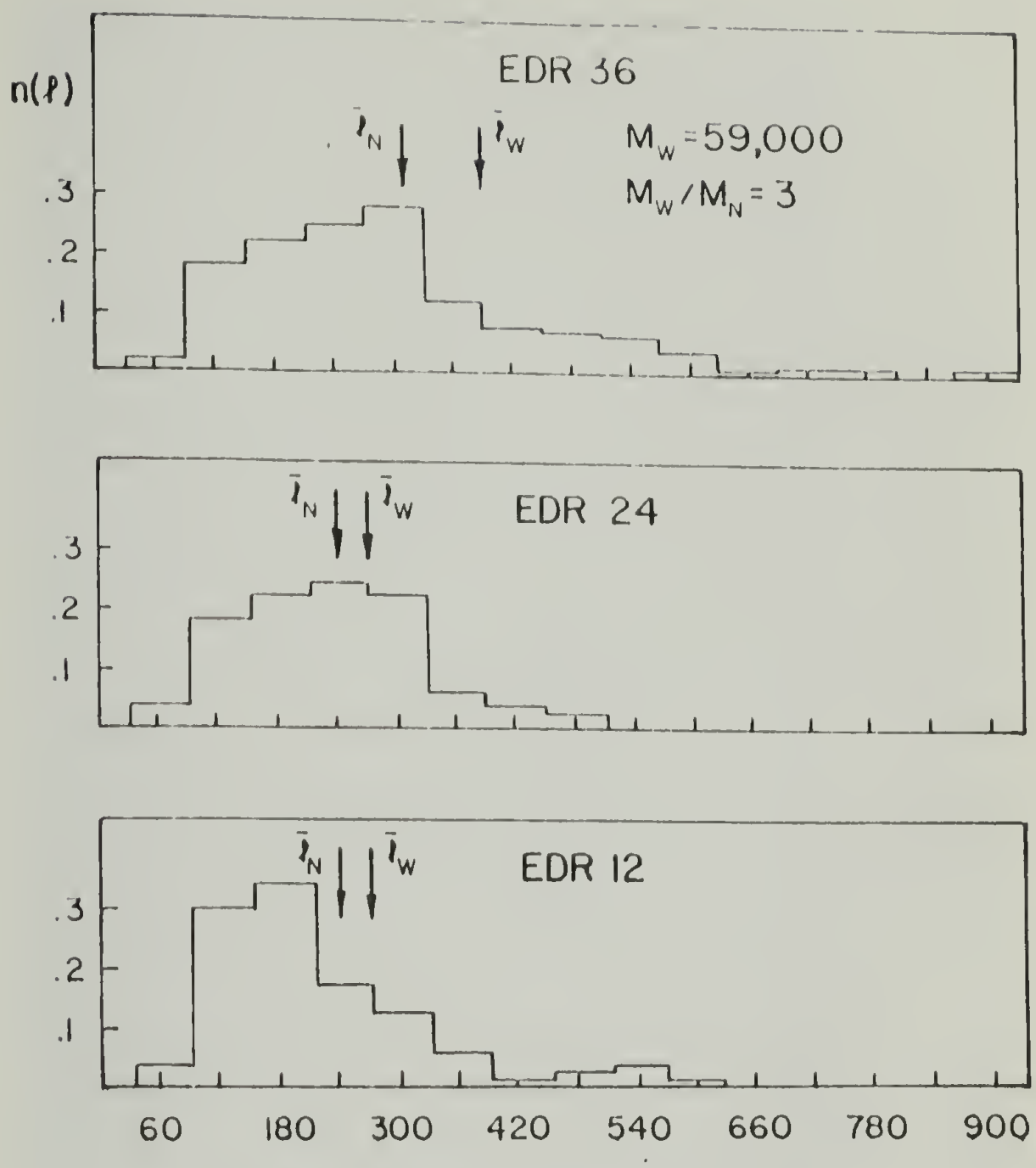

Figure 5.5. Histograms of the fraction of crystals of length l, n(l), plotted vs. length, l as measured by dark field electron microscopy using the 110 and 200 reflections. The positions of the number average, $\bar{l}_N^{DF}$, and weight average, $\bar{l}_W^{DF}$, crystal length are indicated on the histogram.

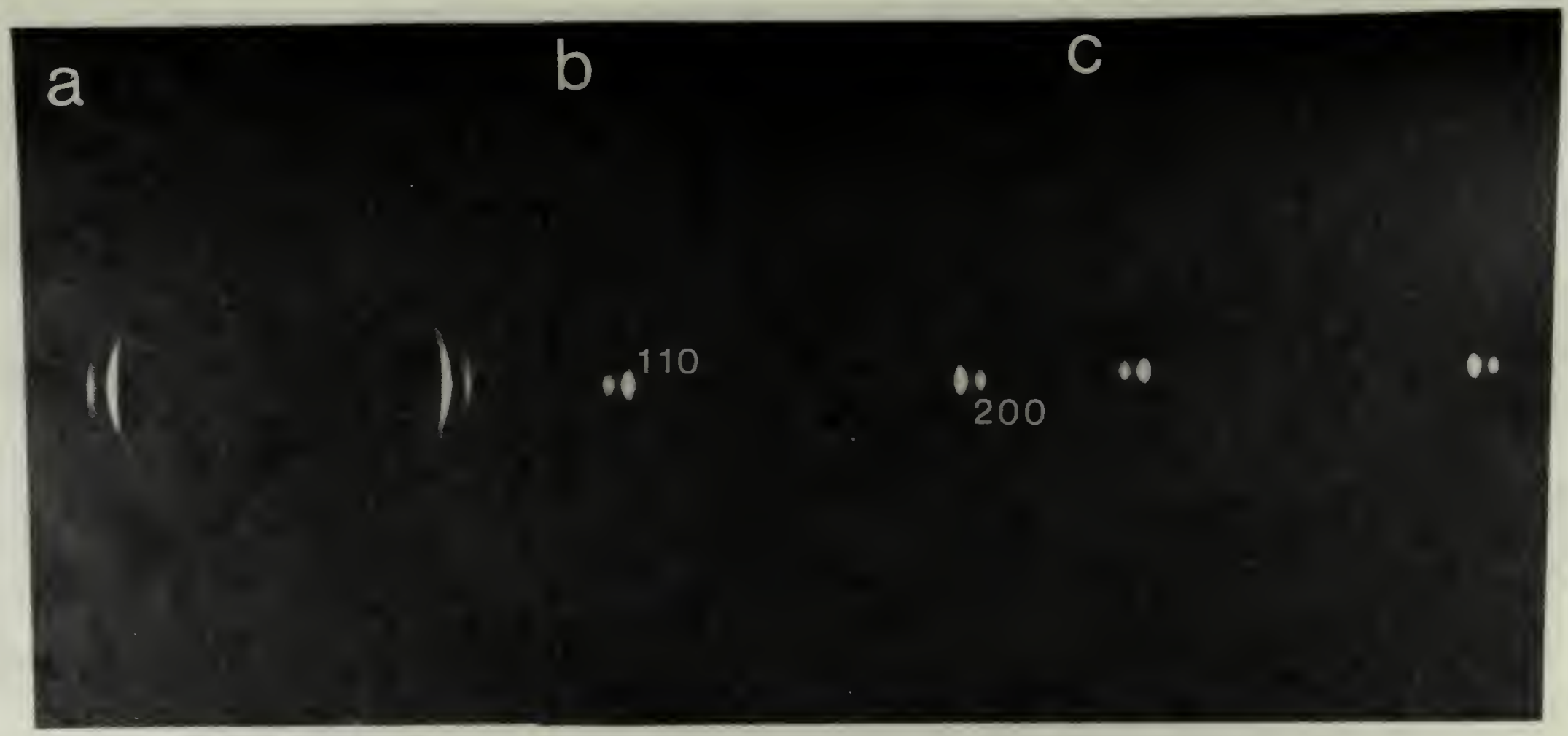

Figure 5.6 Wide angle x-ray diffraction patterns obtained with a Statton camera for: (a) EDR 12, (b) EDR 24 and (C) EDR 36 samples.

camera for the 12, 24 and 36 EDR samples. The orientation was quantized using microdensitometry of the flat plate WAXD patterns. The azimuthal angle of arcing where the intensity of the 200 reflection decreased to half its maximum value was taken as a measure of orientation (98). The angle was 17°, 6° and 5° for the 12, 24 and 36 EDR samples respectively. This increase in orientation agrees with the electron diffraction result that the c-axis orientation increases greatly up to EDR 24 but only slightly thereafter to EDR 36.

Average crystal lengths in the chain direction were calculated from the integral breadth of the (002) reflection for the two possible cases of Gaussian and Cauchy peak shapes. For Gaussian peaks the lengths were 280 ± 5, 290 ± 5 and 330 ± 5Å for the 12, 24 and 36 EDR samples respectively and 390 ± 5, 415 ± 5 and 490 ± 5Å assuming Cauchy peak shapes. These values are compared with the DF measurements in Table 2.

5.2.6 Small angle x-ray scattering. Figure 7 shows the SAXS isointensity contour plots for the 12, 24 and 36 EDR samples. The vectors $\underline{S}_1$ and $\underline{S}_2$ are defined in the figure as parallel and perpendicular to the fiber (extrusion) direction respectively. All samples show 2-point intensity patterns on the meridian. The outer line in each plot is drawn at 128 counts. The other contour lines are drawn at binary increments. The scattering intensity (in relative

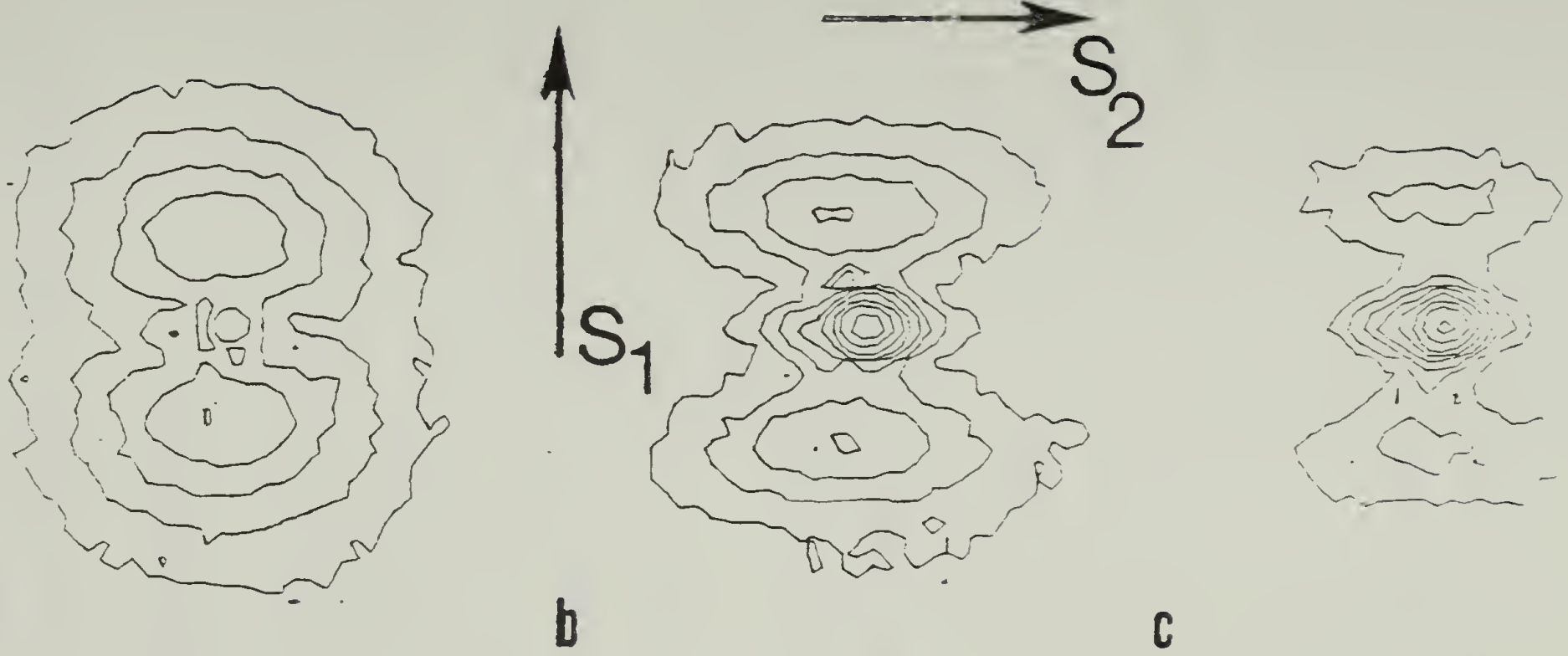

Figure 5.7. Small angle x-ray scattering isointensity contour plots for: (a) EDR 12, (b) EDR 24 and (c) EDR 36 samples. $\underline{S}_1$ and $\underline{S}_2$ indicate directions parallel and perpendicular to the fiber axis respectively.

units) in the meridional direction is plotted vs. scattering angle, 2θ, for all three samples in Figure 8. The intensity decreases with increasing EDR. The long period, L, measured by applying Bragg's law to the position of the peak maximum decreased with increasing EDR as 340, 270 and 245 $\pm$ 8 Å for EDR 12, 24 and 36 respectively.

The SAXS invariant, Q, was measured $(3.9 \pm .2) \times 10^{-5}$, $(1.5 \pm .07) \times 10^{-5}$ and $(1.1 \pm .05) \times 10^{-6}$ gm^2/cm^6 for the EDR 12, 24 and 36 samples respectively. The density difference between the crystalline and non-crystalline regions, $\Delta\rho$, was calculated from Q and the sample density, ρ, using equation 4.5 in section 4.2.3. $\Delta\rho$ is 0.030, 0.024 and 0.022 gm/cm^3 for the 12, 24 and 36 EDR samples respectively. Values of Q, ρ and $\Delta\rho$ are given in Table 1 along with the molecular weights and tensile moduli.

Equation 4 assumes that the interfaces between the two phases are sharp. This was experimentally verified from a plot of ln IS^4 vs. S^2 that had a final slope of zero for large S values (obtained by moving the detector closer to the sample) indicating that the scattered intensity obeyed Porod's law (95) within experimental error.

5.3. Discussion

Figure 9 shows the variations in crystal length, as measured by DF electron microscopy, and SAXS long period with EDR. The DF crystal lengths, $\bar{\ell}_n$, number average and

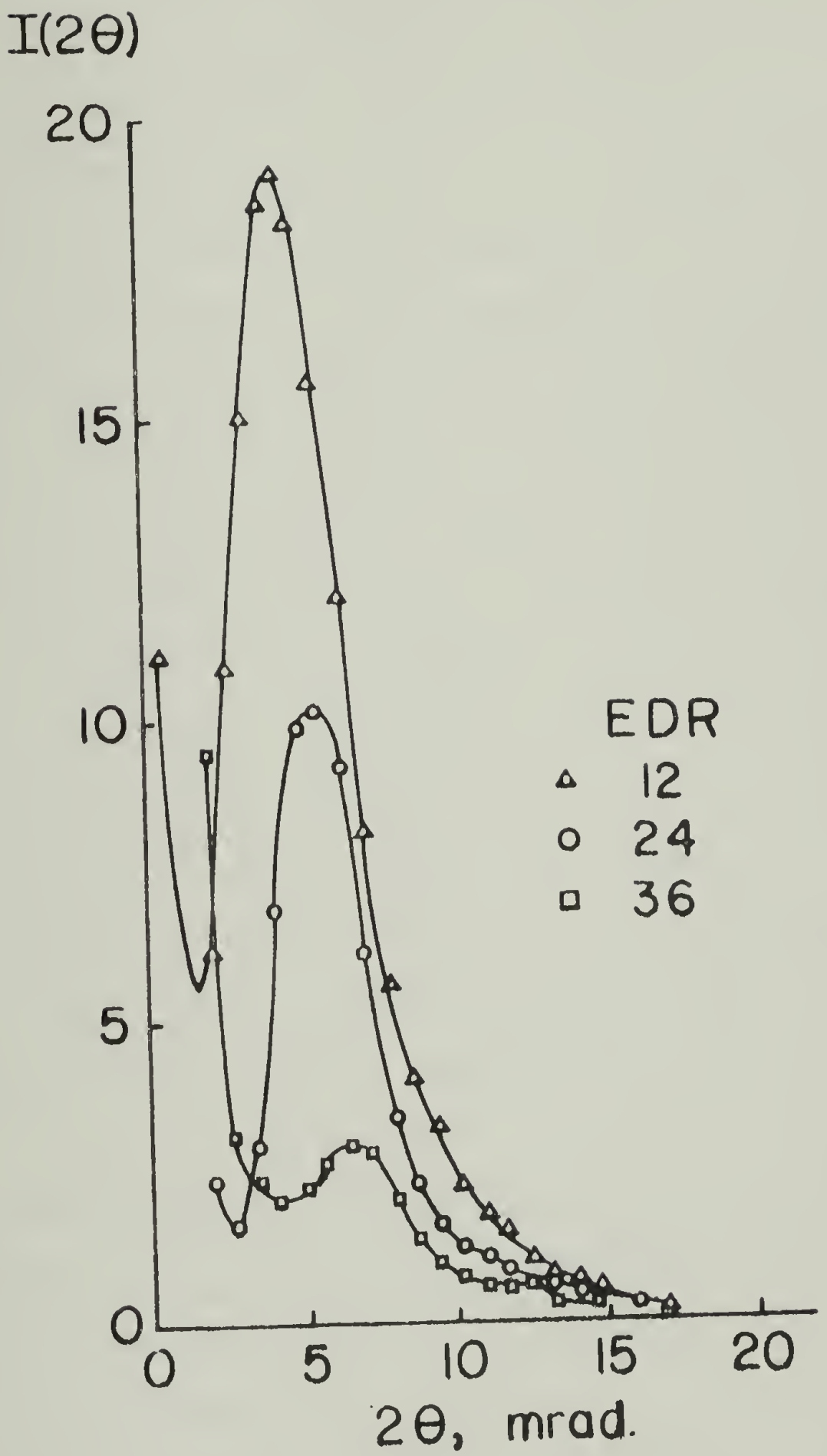

Figure 5.8. Small angle x-ray scattering relative intensity vs. 2θ in the $\underline{S}_1$ direction.

$\bar{\ell}_w$, weight average) and the WAXD crystal coherence length L^{WAXD} (see Table 2) increase with increasing EDR. However, the long period, L^{SAXS}, decreases with increasing EDR. A 70 Å decrease in long period for PE extruded to EDR 30 at 134°C has been reported by Zachariades et al. (35). The weight average crystal length measured by DF equals the long period at EDR 24 where the curves in Figure 9 cross. Since the degree of crystallinity increases with EDR this effect can be interpreted as crystals growing at the expense of the noncrystalline regions. The crystal length distribution, as measured by DF microscopy, develops a tail of long crystals at EDR 36. These long crystals would not be reflected in the long period, since SAXS is an average over the crystals that form periodic macrolattices. However all the crystals are accounted for in the DF and WAXD coherence length measurements. Therefore the periodic crystals could be moving closer together as other crystals lengthen.

Figure 9 also shows the changes in integral breadth of the SAXS maximum in the S_1 direction, $\Delta\beta_1$, and S_2 directions, $\Delta\beta_2$, with EDR. $\Delta\beta_2$ increases proportionately with EDR indicating that the microfibrils are thinning with increasing EDR (see equations 4.7 and 4.8). This correlates with the BF electron microscopy observations of more fine microfibrils and fewer coarse fibrils with increasing EDR. $\Delta\beta_1$ decreases slightly with increasing EDR

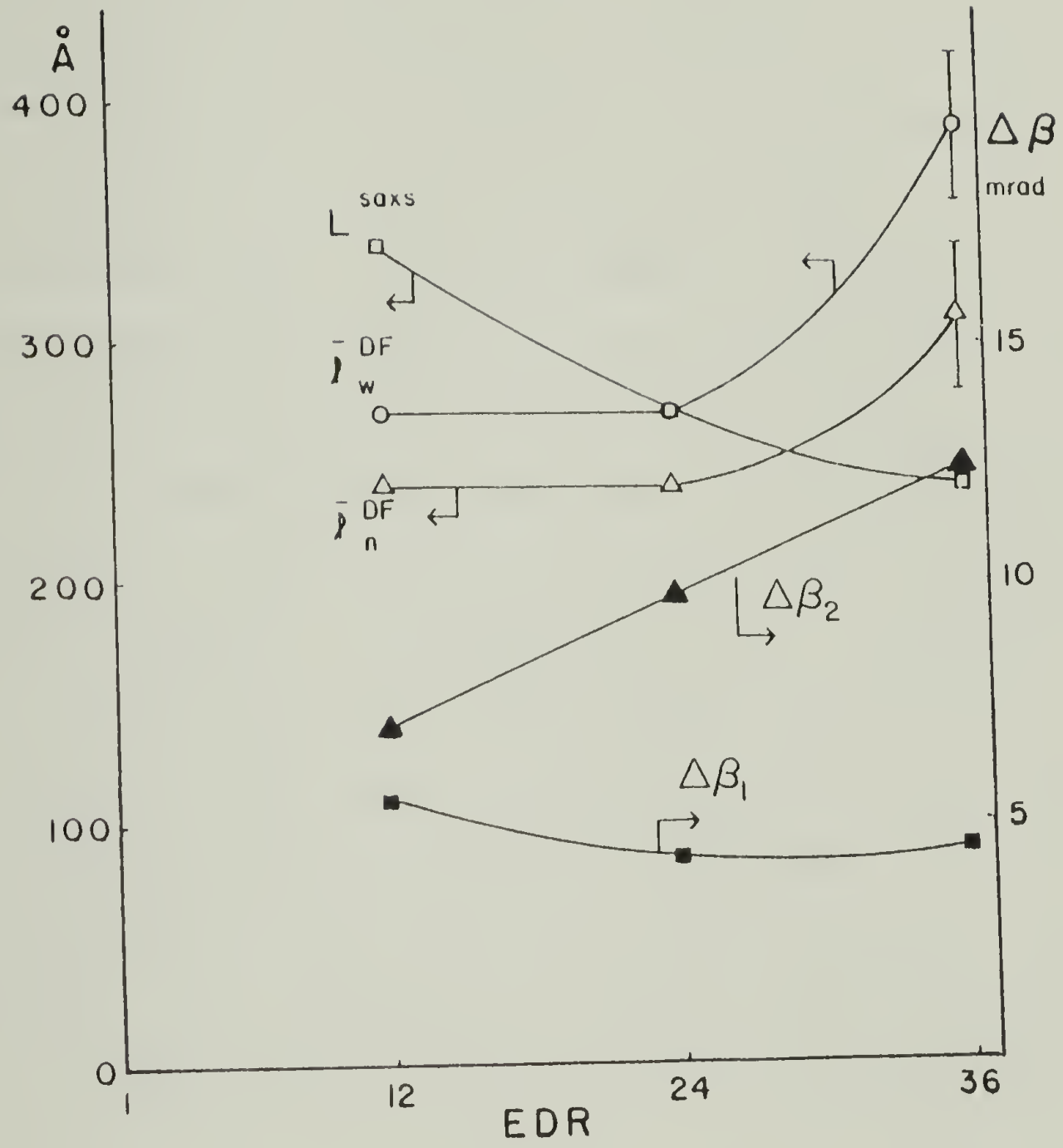

Figure 5.9. Long period, L^{saxs}, and dark field crystal length ($\bar{l}_N^{DF}$, number average and $\bar{l}_W^{DF}$, weight average) variation with EDR. Variation of SAXS peak integral breadths, $\Delta\beta_1$ and $\Delta\beta_2$, with EDR.

indicating a slight perfection of the microfibril macrolattice with greater EDR. However, the effects of size, distortion and fluctuations of the macrolattices cannot be resolved since they all contribute to $\Delta\beta_1$ (see section 4.3).

Figure 10 is a plot of $\Delta\rho$ versus EDR. $\Delta\rho$ decreases with increasing EDR. Since the density of the crystals remains constant the density of the non-crystalline regions is increasing as the EDR increases. The increase in non-crystalline density arises from closer packing of the taut tie molecules, which connect the crystallites, as they become more oriented. $\Delta\rho$ decreases as 0.030, 0.024 and 0.022 gm/cm^3 for the EDR 12, 24 and 36 samples respectively. While Wu et al. (43) did not actually calculate an invariant they noted that the area under the SAXS peaks of hot drawn PE decreased with increasing draw ratio at constant drawing temperature. This decrease by a factor of 7.6 correlated with a 32x increase in tensile modulus from draw ratio 6 to 25.

All these values are much less than the values Fischer et al. (92,93) have reported for PE drawn to 15x at 70°C and 8x at 80°C at the rate of 10 mm/min. $\Delta\rho$ was 0.082 gm/cm^3 for a sample they drew to 15x at 70°C. They determined this using the equation:

$$\Delta\rho = \frac{(\rho-\rho a)^2 + Q}{\rho-\rho a} \qquad (5.1)$$

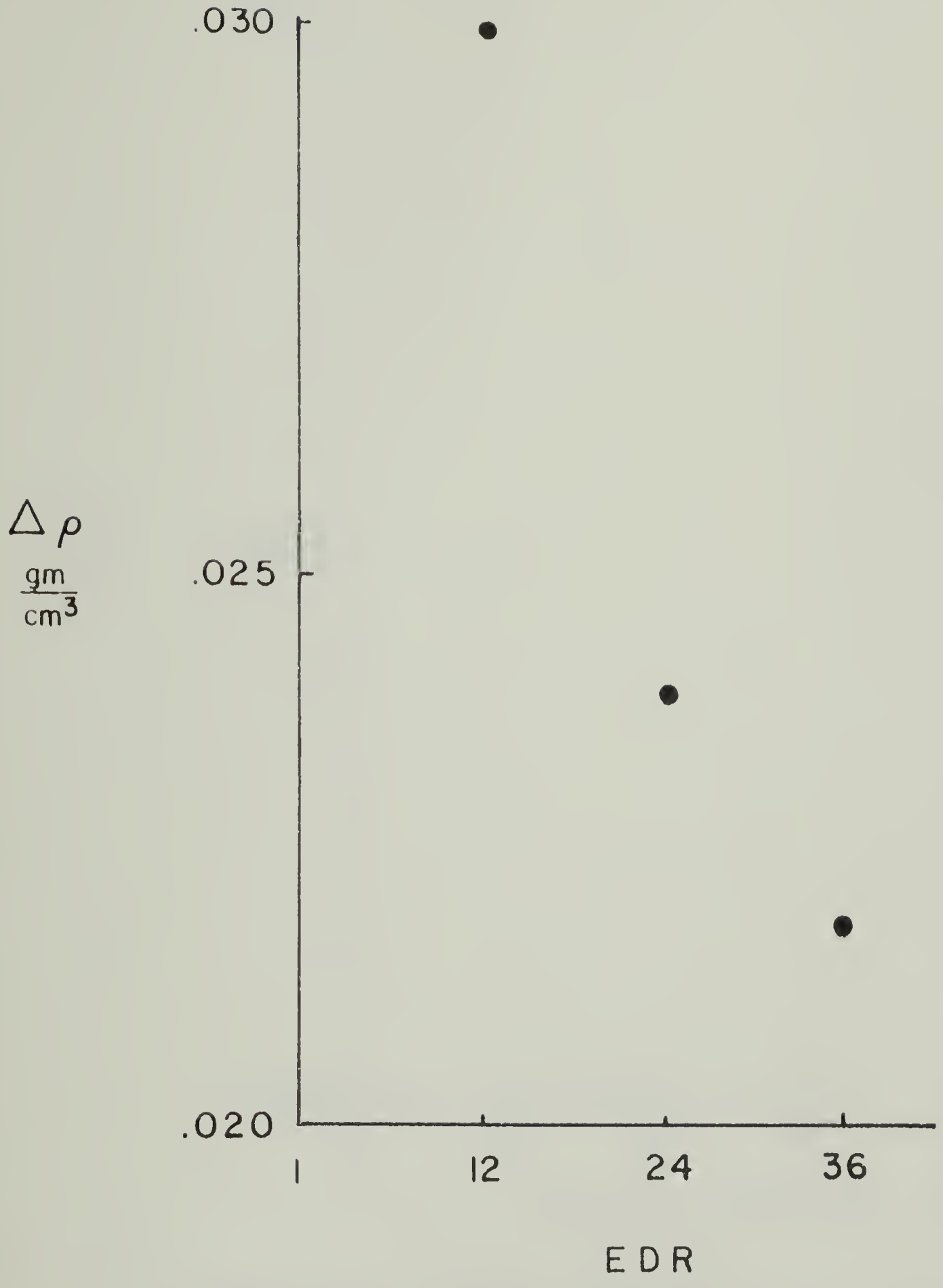

Figure 5.10. Density difference, $\Delta\rho$, between the crystalline and non-crystalline regions as a function of EDR.

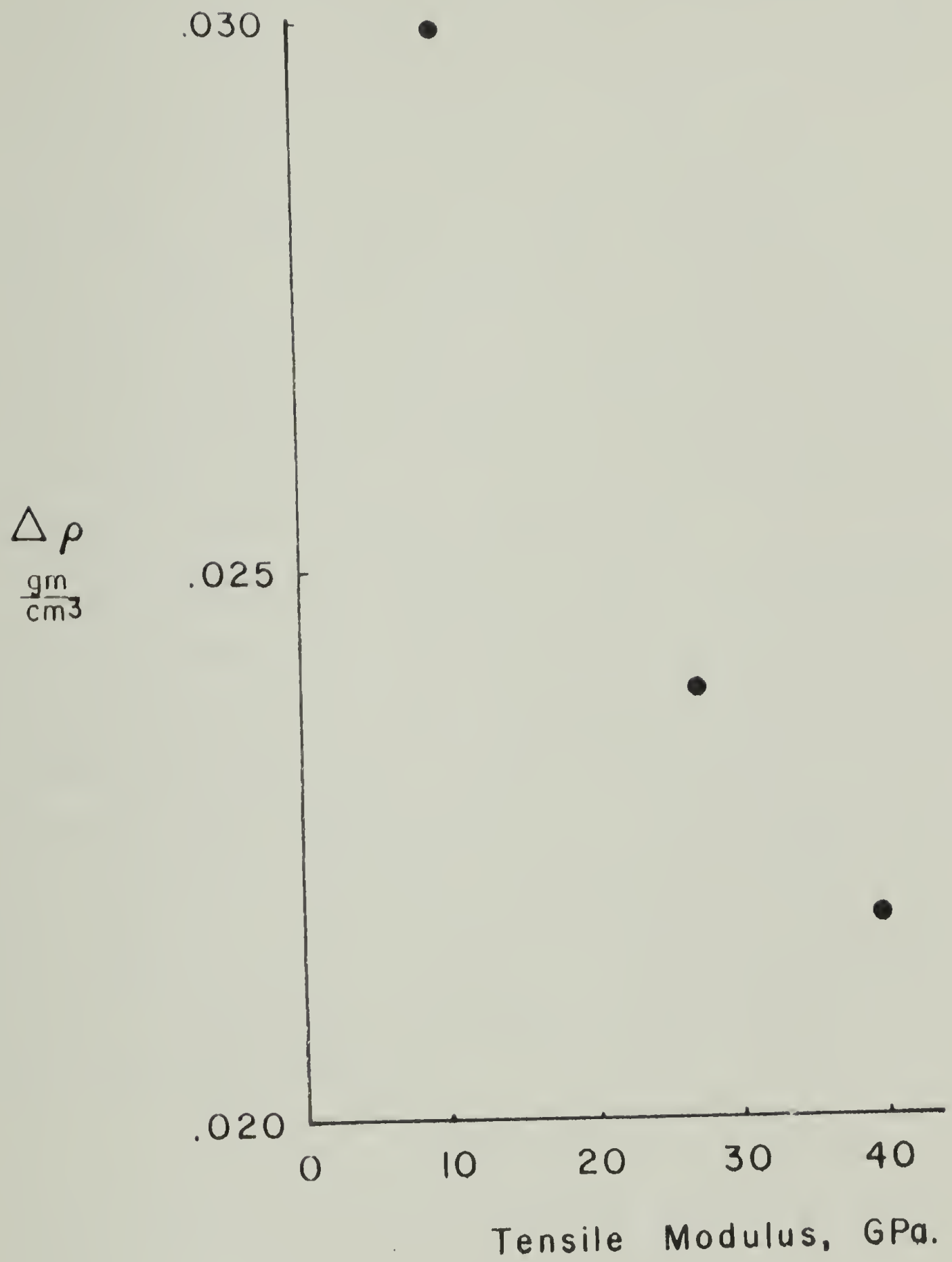

Figure 5.11. Density difference, $\Delta\rho$, between the crystalline and non-crystalline regions as a function of sample tensile modulus.

Where ρ_a was determined from changes in the peak position of the first amorphous halo. Equation 5.1 can be obtained by combining equations 4.3 and 4.4.

This value of $\Delta\rho$ is approximately 170% greater than our EDR 12 sample value of $\Delta\rho$ and 270% greater than the EDR 36 sample. If the Fischer et al. (92) values of ρ and Q and the value of ρ_c which we used (0.997 gm/cm^3) (94) are used to recalculate the density difference, $\Delta\rho$ decreases to 0.065 gm/cm^3. This is still 120% and 200% greater than for our EDR 12 and 36 samples respectively.

These large decreases in $\Delta\rho$ from the drawn samples indicate that the solid state extrusion process may be much more efficient in highly orienting and densifying the noncrystalline phase which provides the important axial connectivity along the microfibrils. The systematic decrease in $\Delta\rho$ with draw ratio as the tensile modulus increases (see Figure 11) is decisive evidence of the role of the taut tie molecules that axially connect the crystallites along the microfiber.

C H A P T E R VI

THE ROLE OF ANNEALING IN DRAWING AND EXTRUSION

6.1 Introduction

The aim of this chapter is to answer the question: are solid state extruded samples equivalent to cold drawn samples that have undergone post-draw annealing? This is addressed by studying the changes in structure, mechanical properties and shrinkage behavior that occur during annealing. These changes are observed for four samples of the same draw ratio, 9X, and molecular weight (M_w = 200,000 and M_w/M_n = 7 - 13) as a function of annealing conditions at constant temperature, 120°C. The samples are: 1) cold drawn at room temperature, 2) cold drawn at room temperature and then annealed for five minutes with fixed ends (cold drawn-annealed-fixed), 3) cold drawn at room temperature and then annealed with free ends for five minutes (cold drawn-annealed-free) and 4) solid state extruded. The annealed samples have the same residence time, five minutes, at the annealing temperature as for the solid state extruded sample.

Two other samples of draw ratio 9 were also studied for comparison but only by SAXS and WAXD. These were a

cold drawn sample annealed for 1 minute with free ends and a hot drawn sample prepared at 120°C.

6.2 Results

6.2.1 Tensile moduli. The tensile moduli of the samples are given in Table 1. Moduli were measured after storing the samples for at least 1 month after preparation. This was long enough to eliminate any uncertainty from modulus increase on storage after annealing as has been reported by Keller et. al. (25). The cold drawn, cold drawn-annealed-fixed and solid state extruded sample all have approximately the same tensile modulus of 8 GPa. while the modulus of the cold drawn-annealed-free sample decreased to 2.5 GPa.

6.2.2 Shrinkage. The shrinkage behavior of the cold drawn, cold drawn and annealed-fixed and solid state extruded samples on heating below T_m is shown in Figure 1. The cold drawn sample starts to shrink at 60°C and shrinks a total of almost 15% before melting. The same sample after annealing with fixed ends and the solid state extruded sample do not start to shrink until 120 to 125°C, approximately the annealing temperature. Their total shrinkage is slightly less than 10%.

Table 6.1

Sample	Modulus GPa	DSC Weight Fraction Crystallinity	Density gm/cm^3
Cold Drawn	8.8 ± 1	.65	.956
Annealed Free, 5 min.	2.5 ± 1	.70	.963
Annealed Fixed, 5 min.	8.0 ± 1	.65	.964
Solid State Extruded	8.1 ± 1	.70	.966

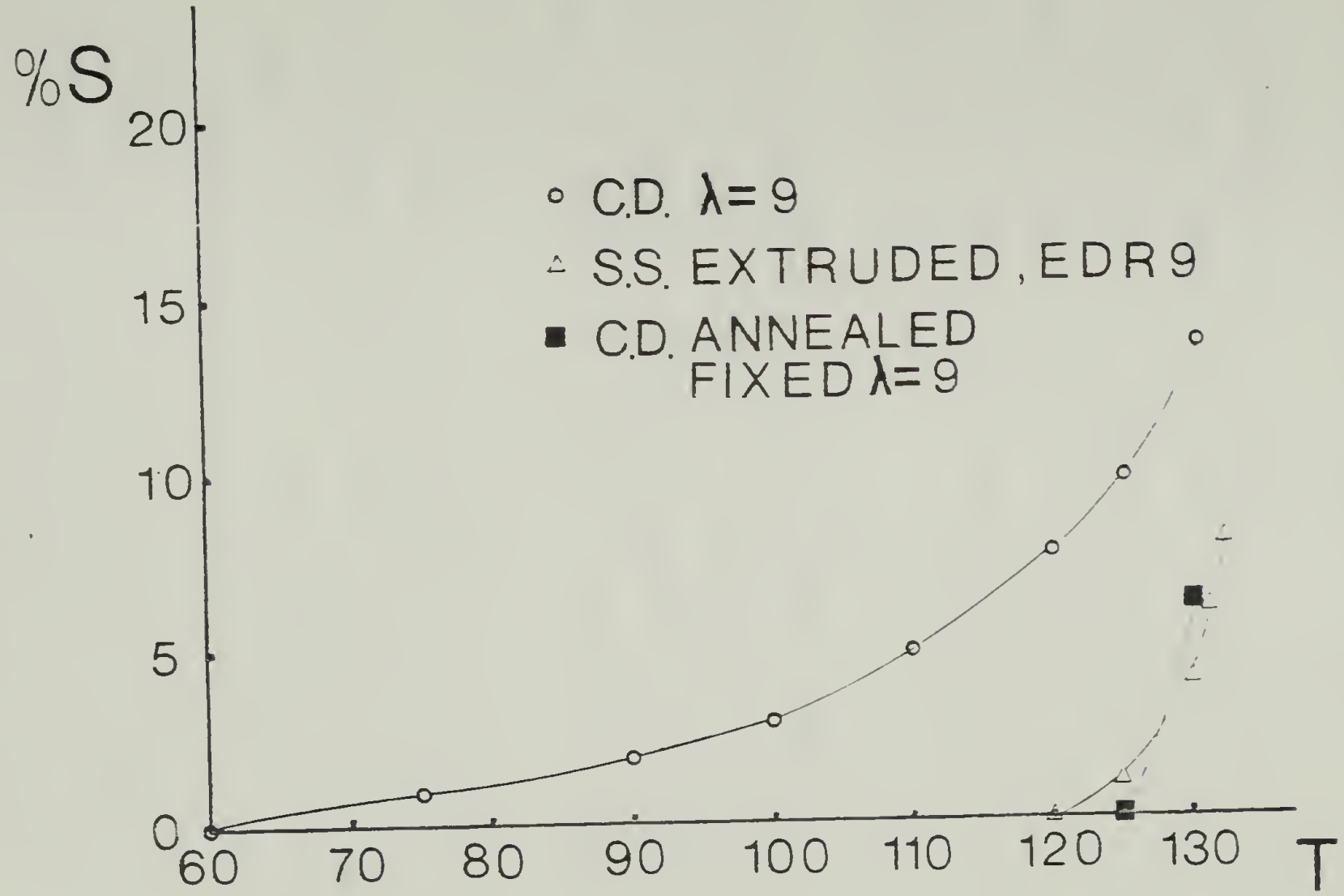

Figure 6.1 Percent shrinkage at constant temperature for cold drawn, cold drawn and annealed with fixed ends and solid state extruded sample.

6.2.3 Differential scanning calorimetry (DSC). The weight fraction degree of crystallinity, χ, is given in Table 1. All samples had the same melting peak temperature 136 ± 1°C. All DSC scans showed the same shape. A typical scan, for the solid state extruded sample is shown in Figure 6.2.

6.2.4 Density. Sample densities are given in Table 1. Samples were drawn at the slow rate of 2 mm/min. to minimize void formation. All samples were optically transparent indicating that an appreciable number of voids are not present and influencing the density values (see calculations in Appendix III).

6.2.5 Electron microscopy. The BF images of all 4 samples are very similar showing a structure of well oriented microfibrils typically several hundred Å wide with interconnectivity and branching that has previously been observed (see Section 5.2.4).

A selected area electron diffraction pattern and 110-200 CTEM-DF image of EDR 9 solid state extruded sample are shown in Figure 3. This figure is representative of all 4 samples showing the well oriented fiber pattern with the DF microscopy showing the microfibrils consisting of small adjacent crystallites 100 to 400 Å long. The differences in structure become more apparent when the crystal size distributions are compared quantitatively as histograms of the number of crystals of length ℓ, $n(\ell)$, vs.

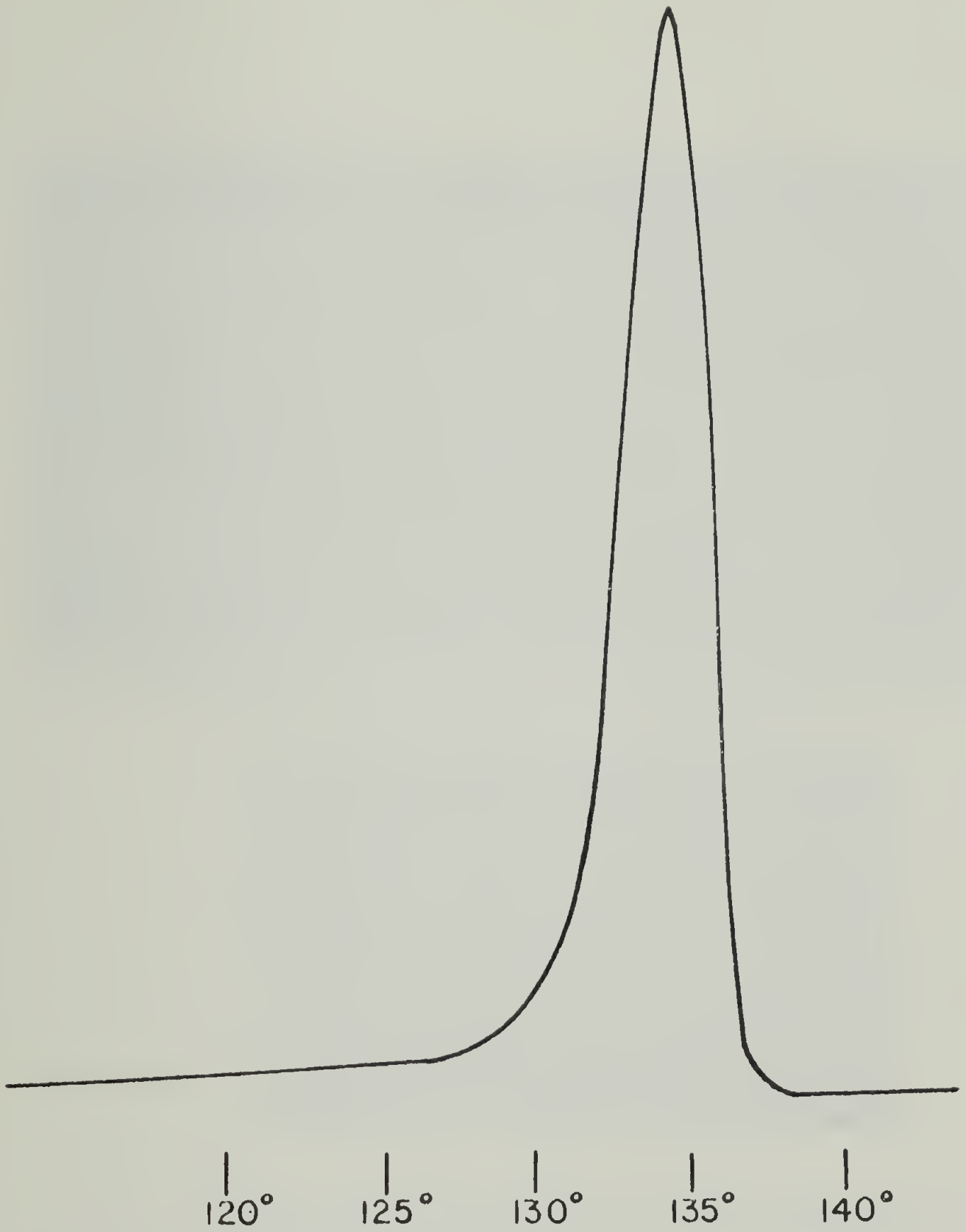

Figure 6.2 DSC scan for the cold drawn sample annealed with fixed ends. The heating rate was 10° C/min.

Figure 6.3 Selected area electron diffraction pattern and 110-200 CTEM dark field image of the solid state extruded sample of EDR 9.

length l in Figure 4. The crystal sizes are shorter and the distributions narrower than for the higher draw ratio solid state extruded samples discussed in Chapters IV and V. The cold drawn sample has the shortest crystals and annealing this sample with fixed or free ends shifts the distribution to longer crystals. The solid state extruded sample has a distribution similar to the annealed samples.

6.2.6 Wide angle X-ray diffraction. Figure 5 shows the wide angle X-ray diffraction patterns obtained with the Statton camera for the cold drawn, cold drawn-annealed, and solid state extruded samples. The cold drawn and cold drawn-annealed-fixed samples show the least and nearly equal arcing of the 110 and 200 reflections indicating the greatest c-axis orientation in the draw direction. The sample annealed with free ends shows some loss of orientation from the cold drawn sample. The solid state extruded sample shows the poorest orientation of these 6 samples.

Crystal lengths in the chain direction, L^{WAXD}, were calculated for 2 cases assuming Gaussian and Cauchy peak shapes. The values are shown in Table 2.

6.2.7 Small angle X-ray scattering. SAXS intensity countour plots are shown in Figure 6 for the cold drawn, cold drawn-annealed, solid state extruded and hot drawn samples. The cold and hot drawn samples exhibit two-point patterns. The cold drawn sample has a strong equatorial

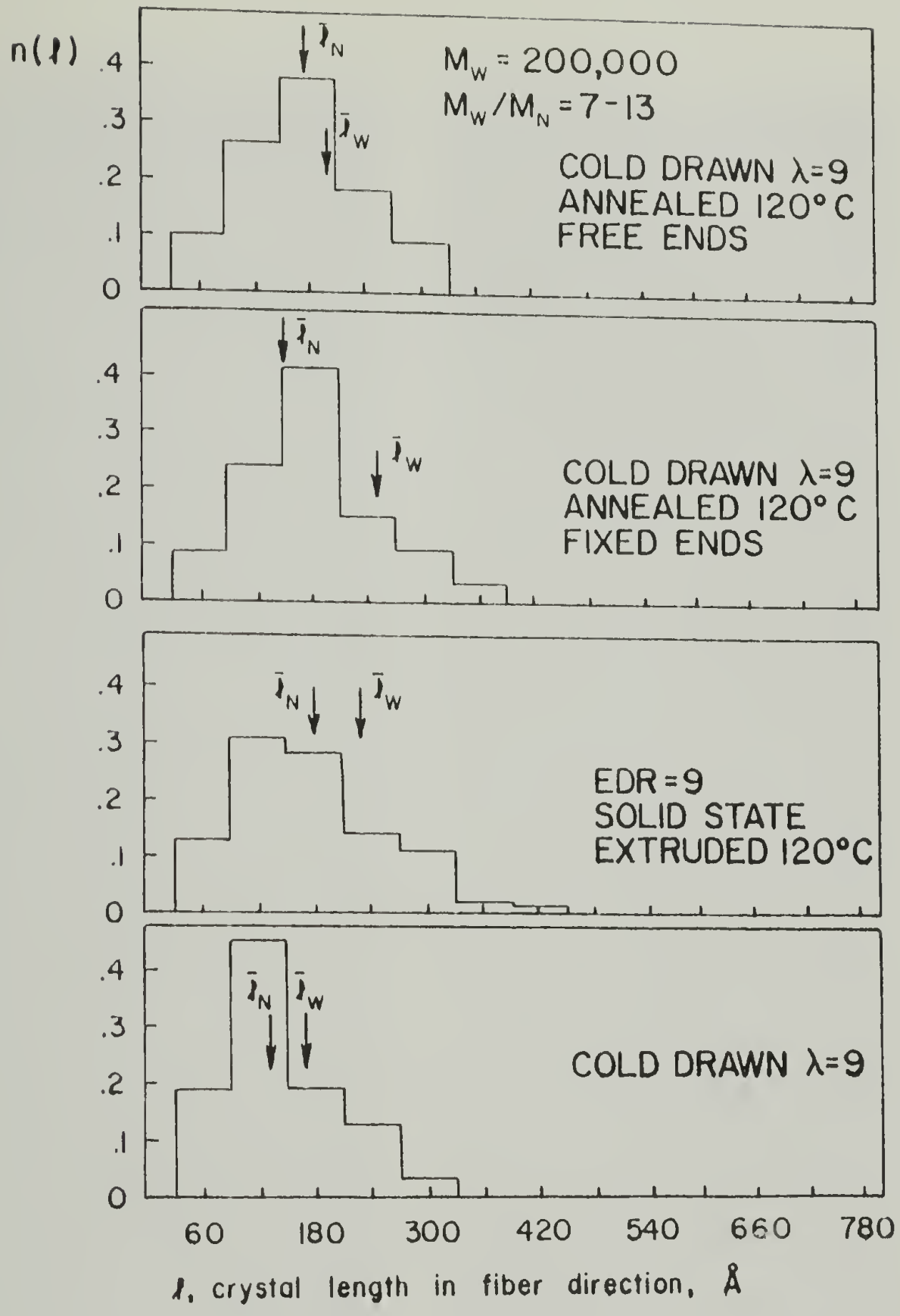

Figure 6.4. Histograms of the fraction of crystals of length l, n(l), plotted vs. length, l, as measured by dark field electron microscopy using the 110 and 200 reflections. The positions of the number average, $\bar{l}_N^{DF}$, and weight average, $\bar{l}_W^{DF}$, crystal length are indicated on the histogram.

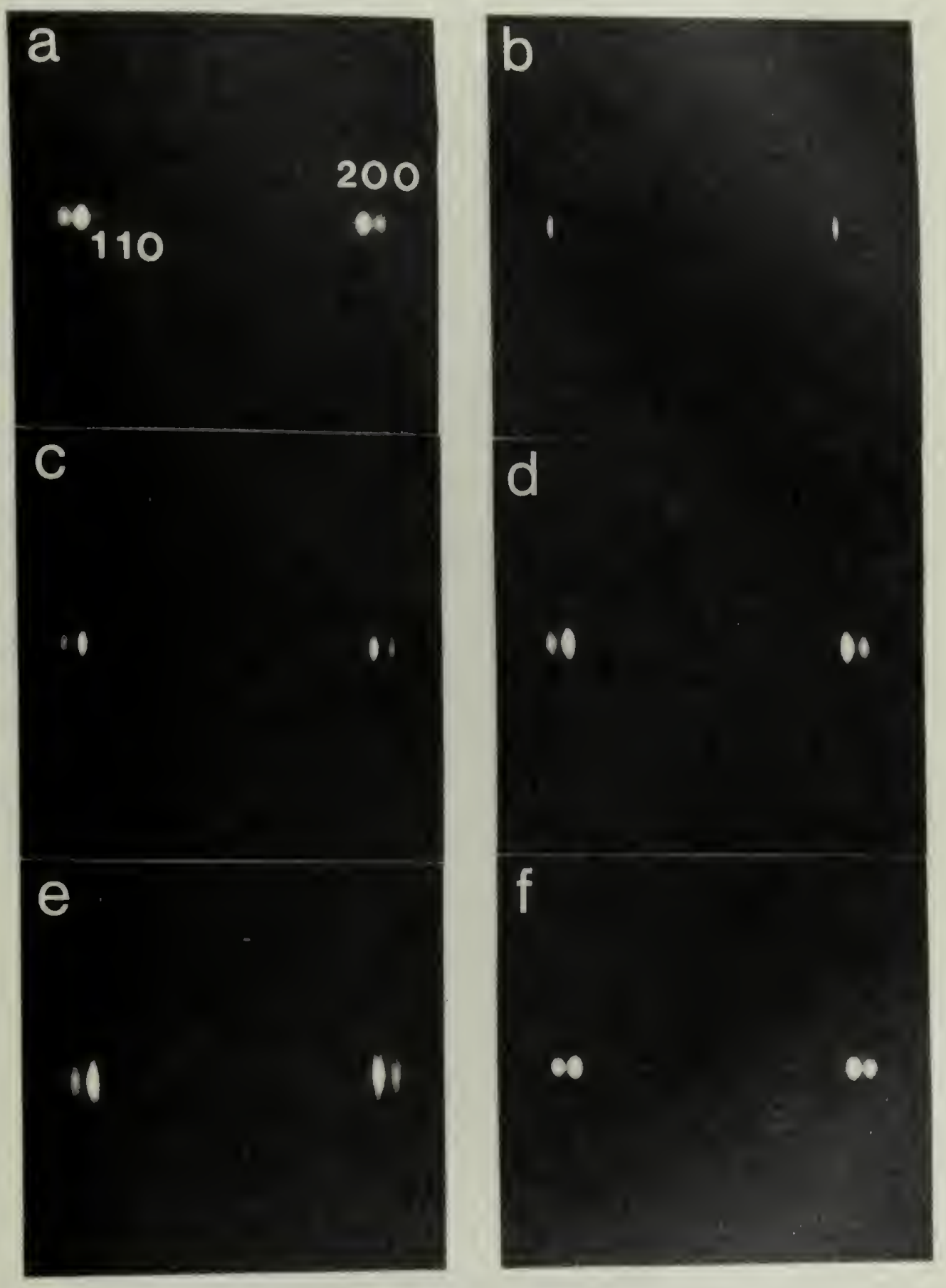

Figure 6.5 WAXD patterns obtained with a Statton camera for: (a) cold drawn, (b) hot drawn, (c) cold crawn-annealed-free-1 min., (d) cold drawn-annealed-free-5 min., (e) solid state extruded and (f) cold drawn-annealed-fixed-5 min.

Table 6.2

Sample	L^{WAXD}		SAXS L, long period ± 8A
	Gaussian ± 5A	Cauchy ± 5A	
Cold Drawn	190	240	190
Annealed Free, 1 min.	220	280	160
Annealed Free, 5 min.	260	350	320
Annealed Fixed, 5 min.	230	310	285
Hot Drawn	280	380	320
Solid State Extruded	230	305	290

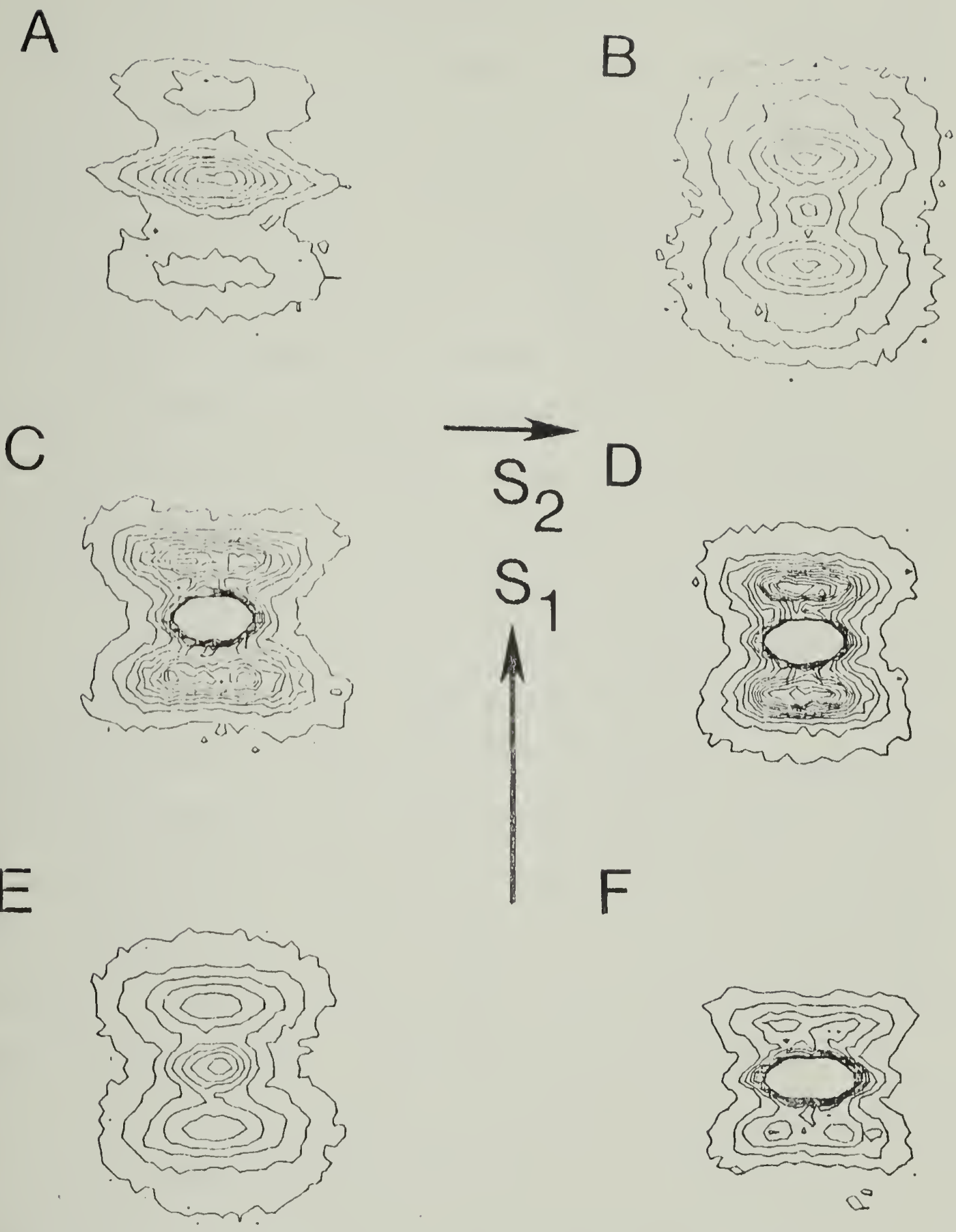

Figure 6.6 SAXS isointensity contour plots for: (a) cold drawn, (b) hot drawn, (c) cold drawn-annealed-free-1 min., (d) cold-drawn-annealed-free-5 min., (e) solid state extruded and (f) cold drawn-annealed-fixed-5 min. $\underline{S}_1$ and $\underline{S}_2$ denote directions parallel and perpendicular to the fiber axis.

streak through the origin which indicates some long narrow microvoids parallel to the fiber direction (99) while the hot drawn sample is nearly free of such void scattering. Annealing the cold drawn sample with free ends for 1 minute caused splitting of the two-point pattern to a four-point pattern. After annealing for 5 minutes, the four-point pattern changes to a two-bar pattern. This is possibly a two-point pattern combined with a remnant of the four-point pattern. However, annealing with fixed ends for 5 minutes results in a clear four-point pattern. The solid state extruded sample has a two-point pattern.

The long periods, L, of the 6 samples are given as a function of residence time at 120°C in Figure 7 and are compared with the values of L^{WAXD} in Table 2. The residence times correspond to the post draw annealing time for the cold drawn samples that were annealed and to the residence time at 120°C for the hot drawn and solid state extruded samples. The cold drawn sample (zero annealing time) has a long period of 190Å. Annealing for 1 minute with free ends causes a 16% shrinkage of L to 160 $\pm$ 8 Å. On continued annealing with free ends for a total of 5 minutes, L increases to 320Å. The hot drawn sample also shows a long period of 320Å. The annealed-fixed and solid state extruded samples of 5 minute residence time have slightly smaller long periods of 285Å and 290Å respectively.

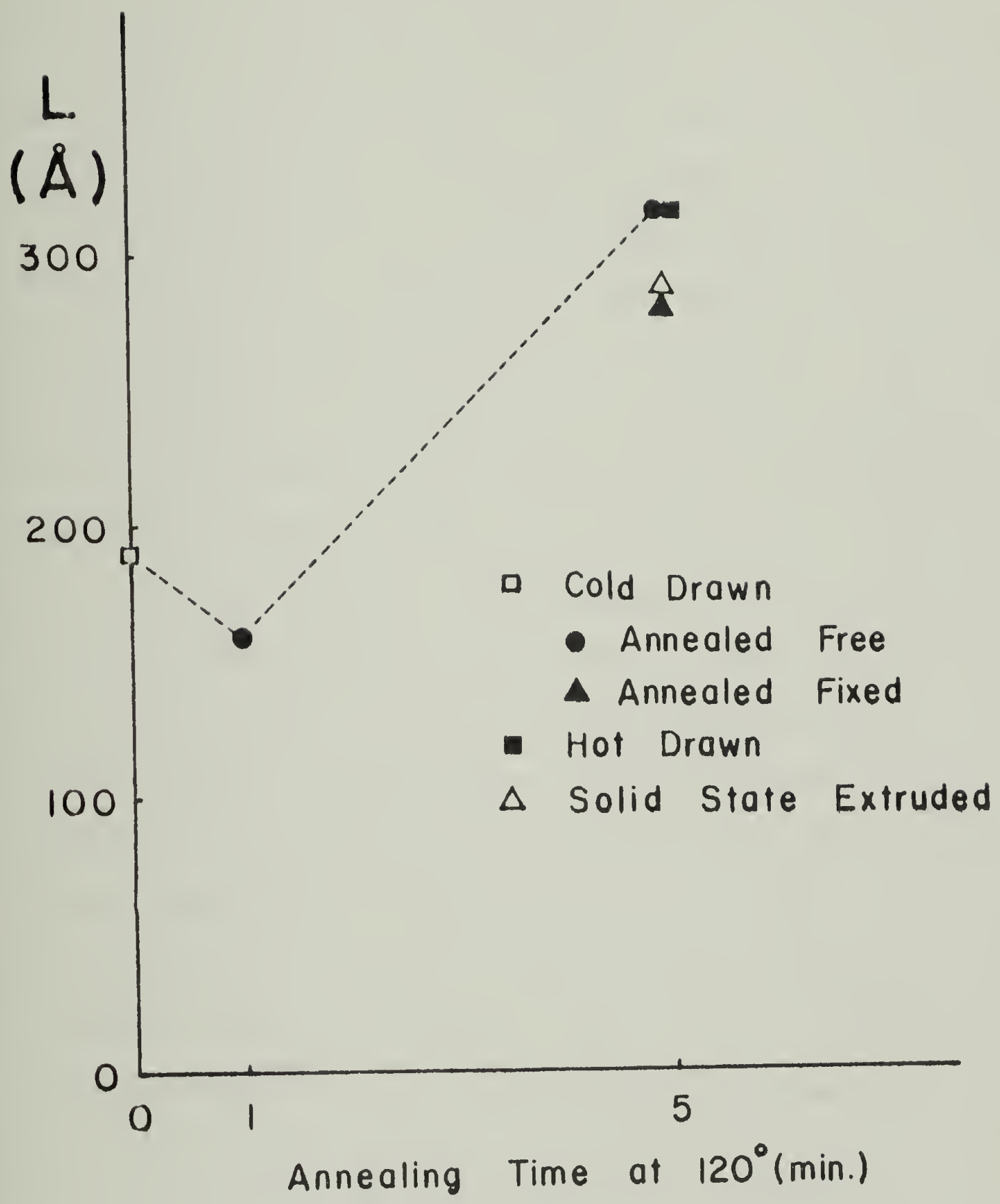

Figure 6.7. SAXS long period, L, as a function of sample residence time at 120°C.

Figure 8 shows the changes in integral breadth, $\Delta\beta_1$, of the SAXS peak along the fiber axis as a function of time at 120°C. The definition of the directions, S_1 and S_2, in which $\Delta\beta_1$ and $\Delta\beta_2$ are measured is shown in Figure 5 following Crist (44,45). The hot drawn sample has the smallest value of $\Delta\beta_1$ indicating the greatest perfection of the macrolattice along the microfibril direction. The hot drawn sample is followed by the solid state extruded sample, cold drawn-annealed with free ends and cold drawn-annealed with fixed ends in order of increasing $\Delta\beta_1$.

The changes in SAXS integral breadth perpendicular to the fiber axis, $\Delta\beta_2$, are shown in Figure 9 as a function of time at 120°C. $\Delta\beta_2$ is inversely proportional to microfiber width. The cold drawn sample has the largest $\Delta\beta_2$ (16.8 mrad.), hence the finest microfibers while the hot drawn sample has the smallest $\Delta\beta_2$ (7.2 mrad.) and the widest microfibers. The $\Delta\beta_2$ of the cold drawn-annealed-free sample shows an anomalous behavior. The lateral integral breadth first decreases to 10.2 mrad. after annealing for 1 minute as the two-point pattern of the cold drawn sample splits to a four-point pattern, indicating a widening of the microfibers as the crystals tilt. Then after 5 minutes of annealing, $\Delta\beta_2$ increases to 12.2 mrad. as the pattern changes to a two-bar type. This final $\Delta\beta_2$ should not be interpreted to mean that the microfibrils have become thinner

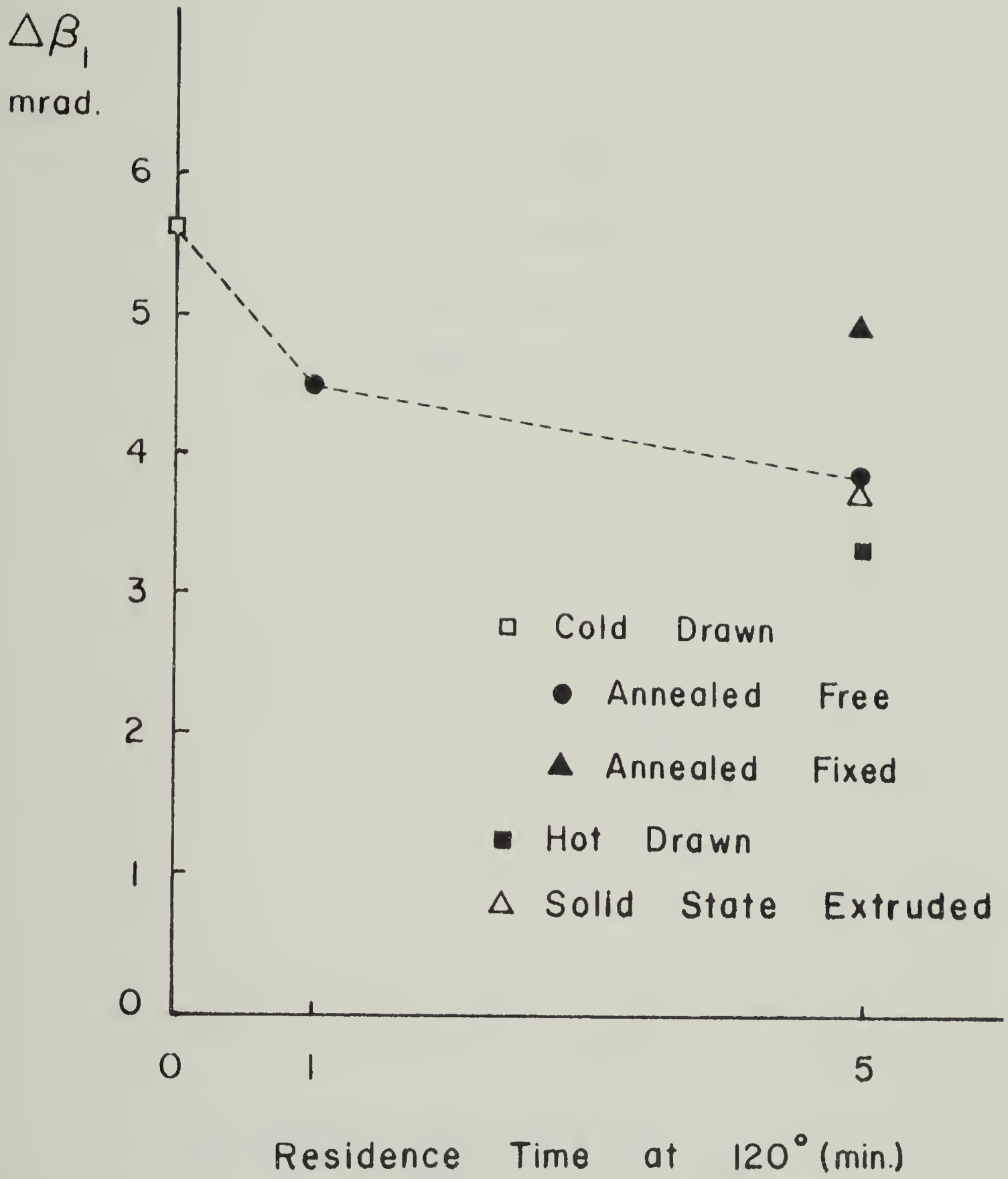

Figure 6.8 SAXS integral breadth parallel to the fiber axis, $\Delta\beta_1$, as a function of sample residence time at 120° C.

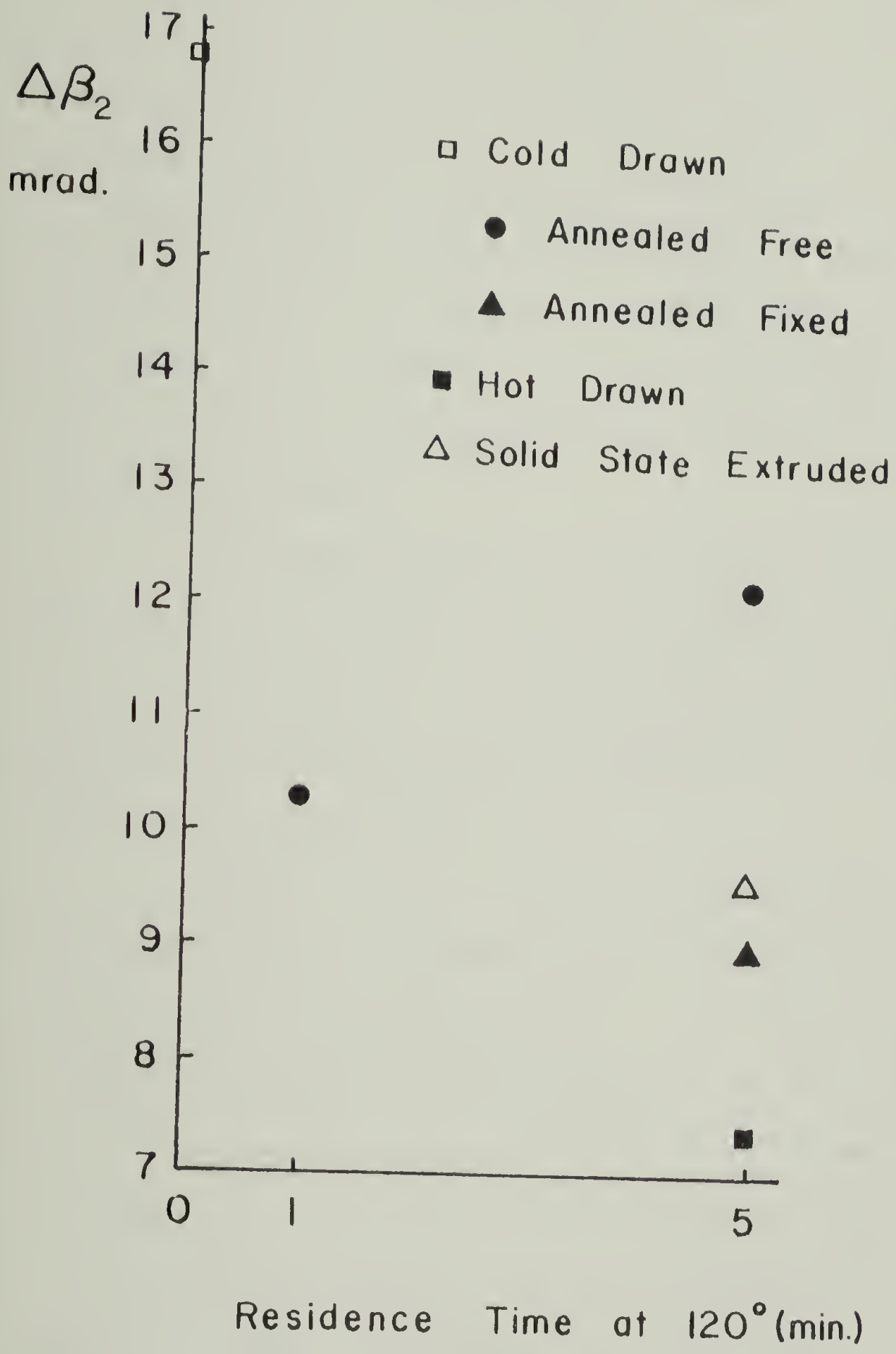

Figure 6.9 SAXS integral breadth perpendicular to the fiber axis, $\Delta\beta_2$, as a function of sample residence time at 120° C.

with annealing but is probably due to the overlapping of a residual four-point with a new two-point pattern to give a broad two-bar pattern. The peak profile changes are shown in three dimensional plots of intensity versus detector position in Figure 10a, b and c for the respective annealing times of 0, 1 and 5 minutes. The microfibers of the solid state extruded and cold drawn sample annealed with fixed ends have similar width with $\Delta\beta_2$ of 9.6 and 9.0 mrad. respectively.

The SAXS invariant, Q, and the density difference between the crystalline and non-crystalline phases, $\Delta\rho$, are given in Table 3. $\Delta\rho$ was calculated from Q and ρ using equation 4.5 as described in section 4.2.3 with ρ_c assumed constant at 0.997 gm/cm^3 (94).

Fischer et al. (92,93), as discussed in section 4.3, reported that $\Delta\rho$ increased from 0.075 gm/cm^3 to 0.101 gm/cm^3 after annealing at 120°C for 1 hour with free ends a sample that was initially drawn to 8X at 80°C. These calculations are based on the invariant and a ρ_a estimated by changes in position of the WAXD amorphous halo with drawing. Fischer's density difference for the 8X sample is about 70% greater than the $\Delta\rho$ for our cold drawn sample of 9X and 130% greater than the value for the solid state extruded sample of EDR 9.

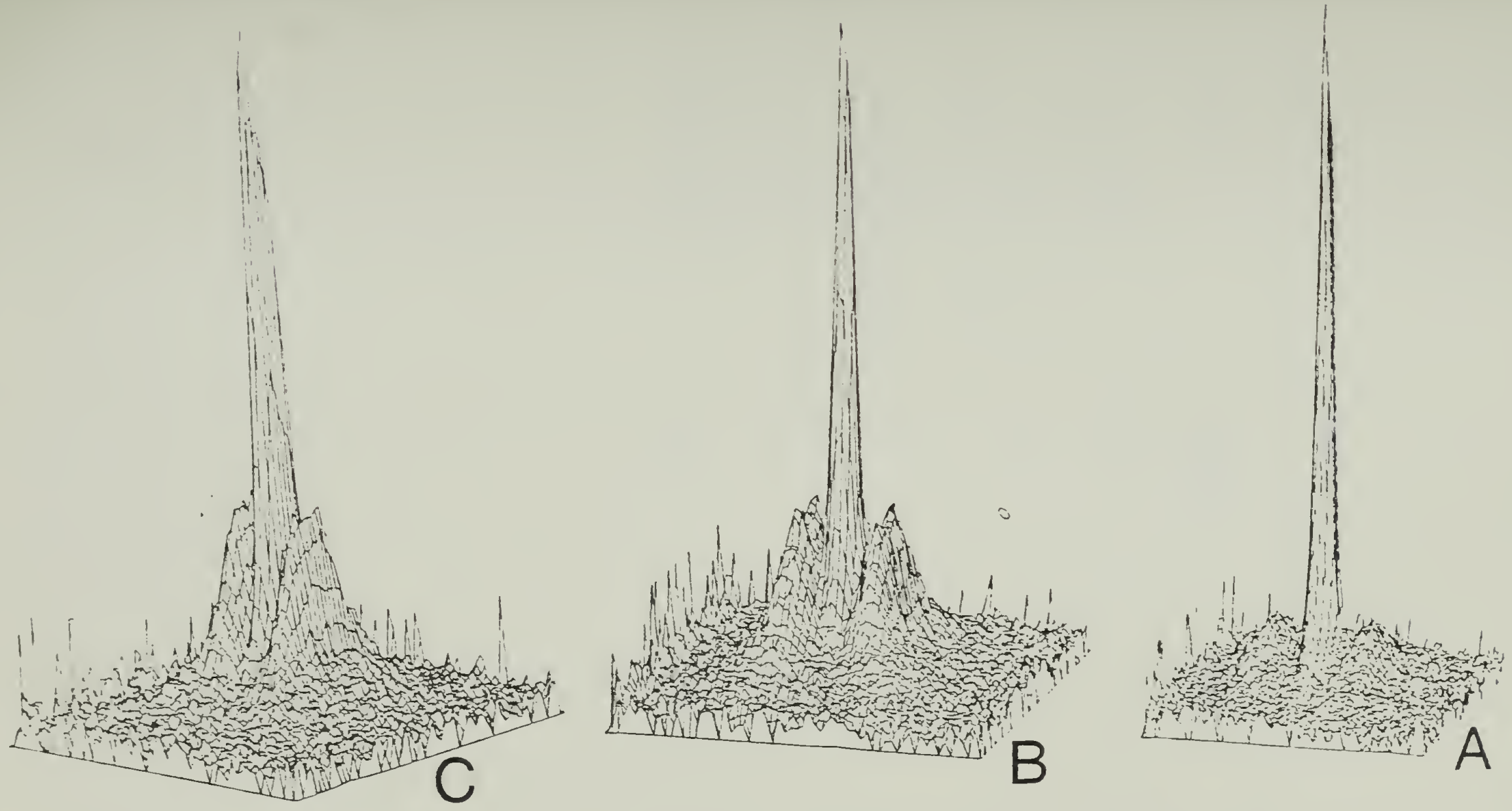

Figure 6.10 Three dimensional SAXS intensity plots of the cold drawn sample annealed with free ends for: (a) 0 minutes, (b) 1 minute and (c) 5 minutes.

Table 6.3

Sample	$\Omega\left(\frac{gm^2}{cm^6}\right)$ x 10^{-5}	$\rho\left(\frac{gm}{cm^3}\right)$	$\Delta\rho\left(\frac{gm}{cm^3}\right)$
Cold Drawn	9.6	.956	.043
Annealed Free, 1 min.	8.2	.963	.036
Annealed Free, 5 min.	6.1	.964	.035
Annealed Fixed, 5 min.	5.2	.963	.036
Hot Drawn	9.6	.965	.035
Solid State Extruded	3.1	.966	.032

6.2.8 Birefringence. Birefringence values are given in Table 3. Even the highest value (4.68×10^{-2} for the solid state extruded sample of EDR 9) is somewhat less than the limiting value of 6.2×10^{-2} obtained when PE is solid state extruded to draw ratios greater than 15 (35).

6.3 Discussion

Electron microscopy and small angle X-ray scattering firmly establish that the microfibrils in these samples consist of alternating crystalline and non-crystalline regions.

The changes in the shrinkage behavior and tensile moduli with annealing are indicative of the changes occuring in the structure of the non-crystalline regions. The macroscopic shrinkage of the cold drawn sample annealed free for 1 minute (15%) nearly equals the long period shrinkage, 16%. One minute is a sufficiently short annealing time so that the taut tie molecules can shrink, moving the crystalline blocks that they are connected with closer together, without the crystals thickening to a new fold period (90, 91). The decrease in modulus from 8 GPa. to 2.5 GPa. is probably due to the relaxation of the taut tie molecules.

The 27% decrease in $\Delta\beta_2$ on annealing the cold drawn sample with free ends for 5 minutes indicates a slight thickening of the microfibers. These decreases in $\Delta\beta_2$ and increases in the long period L^{WAXD} and DF crystal lengths on

annealing indicates that the crystals are growing in all directions.

The cold drawn sample annealed with fixed ends and the solid state extruded sample (both having the same modulus as the cold drawn sample hence approximately the same density of tie molecules connecting crystallites) do not shrink on heating, until just before the melting point. Such "non-shrinkable" tie molecules must be thin "crystalline bridges" that connect adjacent crystalline blocks as envisioned by Ward et. al. (23). These crystalline bridges are probably thinner than 50 Å since they cannot be observed by DF electron microscopy and only need to constitute a few percent of the non-crystalline regions to yield a tensile modulus of 8 GPa. (see the calculations in Chapter I).

The structure of these tie molecules that axially connect the crystals via the non-crystalline region is reflected in the SAXS invariant, Q, which can be used to calculate the density difference between the crystalline and non-crystalline regions, $\Delta\rho$. Figure 11 shows the change in $\Delta\rho$ as a function of residence time at 120°C for all 6 samples. While both the crystalline density and the non-crystalline density may change with temperature and deformation history the results of Fischer et. al. (92,93) show that nearly all of the observed changes in $\Delta\rho$ are due to changes of ρ_a. Therefore decreases in $\Delta\rho$ can be interpret-

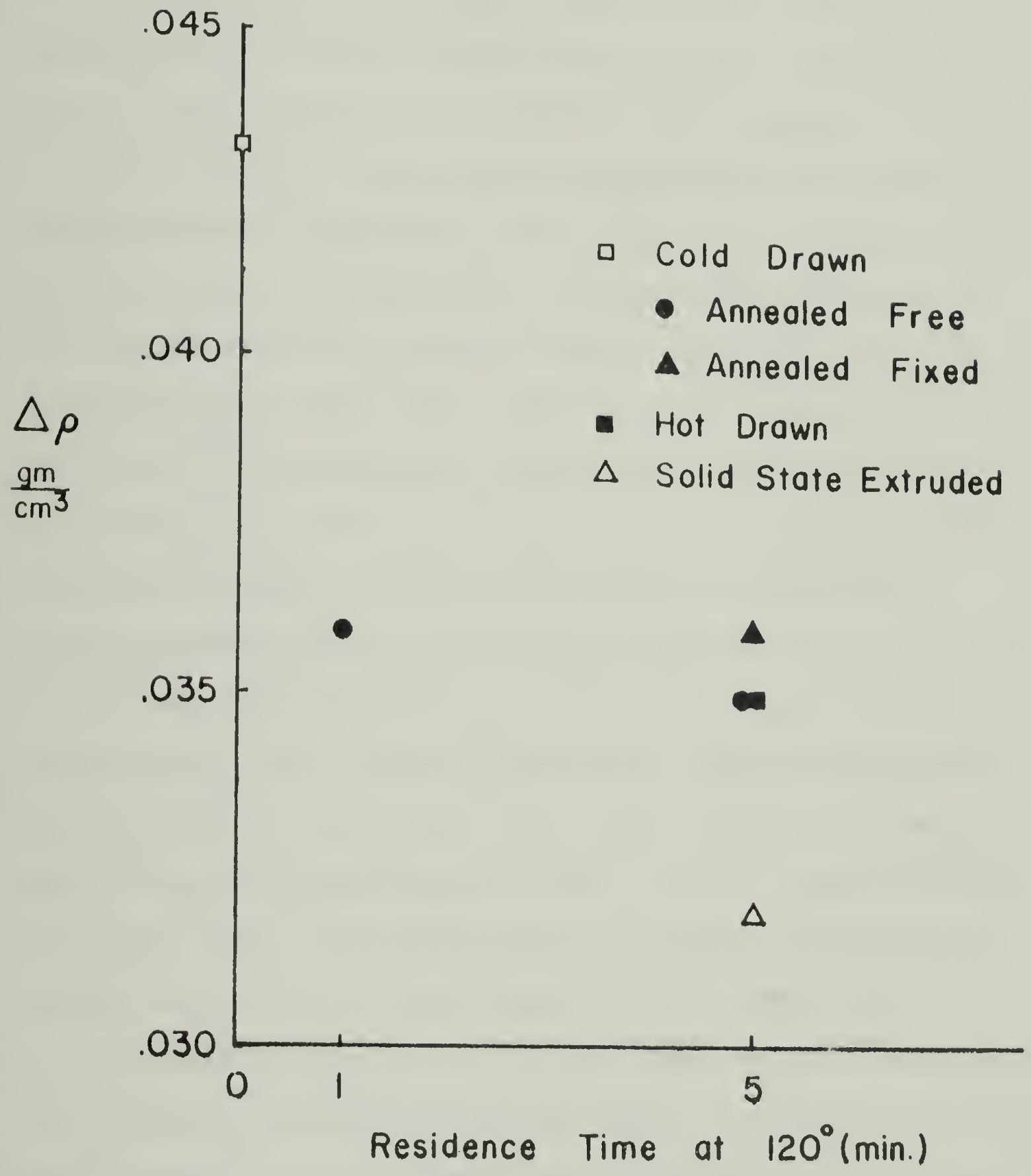

Figure 6.11. Density difference, $\Delta\rho$, between the crystalline and non-crystalline regions as a function of sample residence time at 120°C.

ed as representing an increase in the non-crystalline density. The decrease of $\Delta\rho$ for the cold drawn sample after annealing with fixed or free ends indicates that the density of the non-crystalline regions has increased. This supports the idea that crystalline bridges form from taut tie molecules on annealing with fixed ends. However, the density of the non-crystalline regions also increases for the sample annealed with free ends to slightly less than for annealing with fixed ends. The non-crystalline density may increase during annealing as the chains refold to increase the long period, but with a loss of the load bearing tie molecules between the crystals since the modulus has dropped substantially on annealing from 8.0 GPa to 2.5 GPa. It is also possible that ρ_c is different when the annealing is performed with free or fixed ends since the stresses on the crystals in the latter case might affect void healing. The hot drawn sample has the same $\Delta\rho$ as the sample annealed with free ends. The solid state extruded sample has the lowest value of $\Delta\rho$. Its higher non-crystalline density, than the other samples of the same draw ratio and residence time, and its thermal stability against shrinkage strongly suggest that at least some of the taut tie molecules are arranged as crystalline bridges.

The differences in Q between the samples are much greater than the differences in $\Delta\rho$. This is because equation 4.5 is fairly insensitive to Q. Q for the solid state

extruded sample (3.1×10^{-5} gm^2/cm^6) is about one third of Q for the hot drawn (9.6×10^{-5} gm^2/cm^6) and one half of the cold drawn-annealed-free (6.1×10^{-5} gm^2/cm^6) sample.

The amorphous orientation function, f_a, can be calculated from the birefringence using the Hermans-Stein equation (34) (equation 1.4) if the c-axis orientation function, f_c, is known. We have not calculated f_a since we were not able to determine f_c accurately for these samples and because of large uncertainties associated with f_a that occur for highly oriented samples. These uncertainties occur for four reasons.

1. The amorphous birefringence, Δn_a, decreases to approach the crystal birefringence, Δn_c, as f_a approaches 1. This is because of the internal field effect as the amorphous packing approaches that of a crystal. Thus Δn_a is not independently known.
2. There is a large error in subtracting the two terms close in value in the Stein equation, Δn_t and $\Delta n_c \phi$.
3. ϕ is not accurately known since pure phases properties are inappropriate for calculating ϕ from the density or heat of fusion of the fibers.
4. Δn_c may depend on crystal thickness for very thin crystals.

However the solid state extruded sample has the highest birefringence, $(4.68 \pm .03) \times 10^{-2}$, and the lowest $\Delta\rho$ strongly suggesting it has the highest amorphous orientation and density.

The sample long periods, L, and the crystal lengths measured by WAXD, L^{WAXD}, are very close in value with L usually between the limits of the Gaussian and Cauchy peak shape calculation of L^{WAXD}. They also correspond with the crystal lengths measured by DF microscopy. If crystalline bridges are formed from taut molecules by annealing as advocated by Peterlin (13) according to Ward's Model (23,26) they are not numerous enough or properly distributed to cause the 002 lattice planes in adjacent crystal blocks to scatter coherently.

If cold drawn samples are annealed with fixed ends they are equivalent to solid state extruded samples, of the same draw ratio, in shrinkage behavior and tensile modulus. The only significant differences in morphology are detectable by SAXS.

C H A P T E R VII

CONCLUSIONS AND EXTENSIONS

The results of chapters IV, V and VI demonstrate that the combined techniques of electron microscopy and wide and small angle X-ray scattering elucidate structural differences that correlate with the tensile properties of drawn and solid state extruded polyethylene. Electron microscopy and the large meridional breadth of the SAXS maxima indicate that all these samples from draw ratio 9 to 36 have a distinct microfibrillar structure. The clear 2 and 4 point SAXS patterns observed for these samples which range in tensile modulus from 2.5 to 46 GPa. shows that the microfibrils consist primarily of alternating crystalline and non-crystalline regions. The use of WAXD line broadening to determine the weight average crystal length, SAXS to determine the long period and electron microscopy to observe the crystal size distribution is a much more comprehensive approach to studying the crystallites and their axial connectivity than using the results of a single technique.

The differences between the various drawn, annealed and solid state extruded samples have primarily been in the crystal length and its distribution, microfiber widths and

the density difference between the crystalline and non-crystalline phases. Solid state extrusions to draw ratios of 24 and greater produces much broader crystal size distributions than drawn and solid state extruded samples of draw ratio 9 (compare Figures 5.5 and 6.4) with tail components of long crystals. The microfiber width varies with draw ratio and drawing temperature. However at the same extrusion temperature finer fibrils are found in the higher draw ratio and higher modulus samples. The SAXS invariant is an important measure of axial connectivity between the crystals since it is proportional to the square of the density difference between the crystalline and non-crystalline regions. Q decreases significantly as the tie molecules connecting the adjacent crystallites within the microfibers become more highly oriented and denser packed, hence increasing the tensile modulus.

7.1 Effect of Molecular Weight

Samples of the same 24 EDR but of different molecular weights (M_w = 59,000 and 200,000), extruded at the rates of 20 and 0.6 mm/min. respectively. The samples are the same in preparation except for the 270% difference in M_w and the rate of extrusion. Continuous long crystals are not a general component since they are only a small (6% over 500 Å, up to 3,800 Å long) for the 200,000 M_w sample. The model proposed by Ward et al. (23,26), where the tie

molecules in hot drawn PE are arranged as thin crystalline bridges that axially connect the crystalline blocks, is not appropriate for solid state extruded PE. A sufficiently high concentration of uniformly distributed crystalline bridges would cause the 002 lattice planes of the rather small (circa 250 Å) blocks to scatter coherently as in Ward's results where the WAXD coherence length is about twice the SAXS long period. Crystalline bridges would increase the density of the non-crystalline regions as we have observed. However, the discrepancy between the SAXS long period and the WAXD crystal coherence length for the solid state extruded samples arises because of the broad distribution of crystal lengths, observed directly by DF electron microscopy, since the crystal coherence length is a weight average measure of length. This does not eliminate the possibility of any crystalline bridges in our samples since a few thin isolated bridges might only cause the crystal blocks to scatter coherently in the vicinity of the bridge because of elastic bending. These isolated bridges would be below the limit of DF imaging resolution for PE.

The large decrease of $\Delta\rho$ for these extruded fibers versus isotropic melt crystallized samples supports the taut tie molecules connecting adjacent crystalline blocks in Peterlin's model (5).

In this study we have extensively examined the

structure of two solid state extrudates of different molecular weight. The principle differences in structure that result in the higher molecular weight PE's 70% higher tensile modulus (46 vs. 27GPa.) are:

1. The higher M.W. sample has a longer average crystal length and a small tail component of very long crystals (up to 3,800 Å) observed by DF electron microscopy.
2. The non-crystalline regions of the higher M.W. sample contain more taut tie molecules, which result in the 4% lower value of $\Delta\rho$ than for the L sample, as indicated by the SAXS invariant.

7.2 Morphological Changes with EDR

Electron microscopy and the SAXS line breadth indicate that the microfibers thin as they are drawn during extrusion. As the microfibers thin the density and orientation of the non-crystalline regions along the microfibers increases. This may occur because the material from the outside of the thinning microfibers is transformed into oriented taut tie molecules which increase the non-crystalline density and the elastic modulus by providing more and/or effective load bearing connections as Peterlin has advocated (5, 12, 13). The length of the crystals increases with EDR, as shown by DF electron microscopy and WAXD line breadth, as the microfibrils thin and become stiffer.

The taut tie molecules created in the solid state extrusion process do not cause the 002 lattice planes in adjacent crystal blocks to scatter coherently as would be the case for crystalline bridges (see Ward's model (23) in Figure 1.4). The SAXS long period represents the crystal plus non-crystal thickness in the periodic macrolattices. However the WAXD coherence length, L^{WAXD}, is a weight average of the entire crystal size distribution. The difference between the long period (245 Å) and the L^{WAXD} (330 Å for Gaussian and 490 Å for Cauchy peak shapes) for the EDR 36 sample does not indicate crystalline coherence larger than individual crystallites since L^{WAXD} corresponds with the weight average crystal length (390 Å) measured directly by DF electron microscopy.

7.3 The Role of Annealing

Chapter VI examined the role of annealing in fiber formation for samples of the same draw ratio, 9X, but produced by cold drawing, cold drawing with post-draw annealing, hot drawing and solid state extrusion. All these samples had a microfibrillar morphology. The distribution of crystallite lengths was similar for all samples and much narrower than high draw ratio samples examined in Chapters IV and V (compare Figures 4.5 and 5.5 to Figure 6.4) with a 100% smaller average crystal length. The SAXS long period was predominantly a function of the draw or

annealing temperature. The increase in thermal stability of the cold drawn sample after annealing with fixed ends indicates that it, and the solid state extruded sample, have non-shrinkable taut tie molecules. The cold drawn, cold drawn-annealed with fixed ends and solid state extruded samples have about the same tensile modulus (8 GPa.). Thus approximately the same number of tie molecules are created during the different drawing processes. The modulus decreases for the cold drawn sample when annealed with free ends (from 8 to 2.5 GPa.) since the taut tie molecules can relax during annealing. The low value of $\Delta\rho$ for the solid state extruded sample indicates that an equivalent number of taut tie molecules are arranged with denser packing than in the other sample. While the average crystallite size of the cold drawn sample increases with annealing the tie molecules connecting these crystals do not become sufficiently crystalline and/or numerous to increase the WAXD coherence length much greater than the SAXS long period or the crystal length observed by DF electron microscopy.

These samples of 9X draw ratio show that rather different morphologies can result in the same tensile moduli.

7.4 Possible Extensions

This thesis has revealed new insight into the structure and properties of drawn PE and extruded high

modulus PE. The techniques and approaches developed can now be applied to a greater range of samples and processing conditions. Particularly interesting would be a greater range of molecular weights and narrow molecular weight distributions for hot drawn and solid state extruded samples of the same draw ratio. The study of the role of extrusion rate and residence time also needs more fundamental study.

Several extensions of the experimental techniques and analysis are also possible to compliment these methods of studying fiber structure and deformation. These are:

1. Fourier analysis of wide angle X-ray peak shapes can be used to separate crystal strain and size effects. This will be useful in determining if the crystalline density is decreased by defects during drawing as Fischer et al. (92,93) have suggested. This will also permit a better assessment of the crystalline bridge model of Ward et al. (23,26).
2. Wide and small angle X-ray diffraction measurements under stress (using in house facilities and equipment presently being assembled at Oak Ridge National laboratories) can be used to quantify microfibril deformation. Comparisons of the long period strain, crystal lattice strain and invariant for different samples can

separate shearing of microfibrils during deformation from affine extension within the microfibril structure.

3. Fourier Transform infrared measurements of amorphous orientation would be a useful addition to the invariant in studying the connectivity of the crystals via the non-crystalline regions.
4. Longitudinal Acoustic Mode (LAM) Raman spectroscopy may provide another useful measure of the crystallite length in highly drawn polyethylene and reveal the structure of the tie molecules.
5. Independent measurements of χ, weight fraction crystallinity, by wide angle X-ray diffraction might provide an additional degree of crystallinity to compare with the value obtained by DSC.
6. Modulus measurements of samples that have been partially shrunk by heating to various temperatures below the melting point might indicate differences in the thermal stability of the tie molecules of different processing origin.

REFERENCES

1. K. Sakaoku and A. Peterlin, "Deformation of Extremely Thin Polyethylene Films," Makromol. Chem., 142, 227 (1967).

2. R. G. Scott, "A Study of the Crystalline Structure of Synthetic Fibers by Dark Field Electron Microscopy," J. Poly. Sci., 57, 405 (1962).

3. A. Peterlin and G. Meinel, "Small-Angle X-Ray Diffraction Studies of Plastically Deformed Polyethylene, III. Small Draw Ratios," Makromol. Chem., 142, 227 (1971).

4. H. Kohi, A. Peterlin and P. H. Geil, "Polyethylene Single Crystals, 1. Deformation," J. Appl. Phys., 35, 1599 (1964).

5. A. Peterlin, "Plastic Deformation of Polymers with Fibrous Structure," Coll. and Polym. Sci., 253, 809 (1975).

6. P. B. Bowden and R. J. Young, "Review: Deformation Mechanisms in Crystalline Polymers," J. Mater. Sci., 9, 2034 (1974).

7. P. M. Tarin and E. L. Thomas, "An Electron Microscopy Study of the Microfibrillar Structure of Deformed Polyethylene Spherulites," Polym. Eng. and Sci., 18, 472 (1978).

8. P. M. Tarin and E. L. Thomas, "The Role of Inter and Intra-links in the Transformation of Folded Chain Lamellae into Microfibrils," Polym. Eng. and Sci., 19, 1017 (1979).

9. A. Peterlin, "Crystalline Character in Polymers," J. Polym. Sci., C9, 61 (1965).

10. M. Takayanagi, K. Imada and T. Kajiyama, "Mechanical Properties and Fine Structure of Drawn Polymers," J. Polym. Sci., C15, 263 (1966).

11. G. Wobser and S. Blasenbrey, "Struktur-und Konformat ionsberechnung in Polymeren, II. Idealkristall und Defektzustand Von Polyathylen," Kolloid Z.-Z. Polym., 241, 985 (1970).

12. A. Peterlin, "Elastic Modulus and Strength of Fibrous Material," Polym. Eng. and Sci., 19, 118 (1979).

13. A. Peterlin, "Drawing and Annealing of Fibrous Material," J. Appl. Phys., 48, #10 (1977).

14. A. G. Gibson, J. S. Holt and P. S. Hope, "Factors Affecting Stress Transmission in Crystalline Polymers," J. Polym. Sci., Polym. Phys. Edn., 17, 1375 (1979).

15. P. Barham and A. Keller, "A Criterion for Distinguishing Between Polymer Fibers of Fundamentally Different Origin," J. Polym. Sci., (Letters), 13, 197 (1975).

16. K. Neki and P. H. Geil, "Deformation of Drawn Annealed Polyethylene," J. Macromol. Sci. (Phys). B9(1), 71 (1974).

17. K. Sakaoku and A. Peterlin, "Surface Replicas of Drawn Polyethylene. II. Annealing of Cold Drawn Samples with Different Draw Ratios," J. Macromol. Sci., (Phys), B1(1) 103 (1967).

18. D. M. Bigg, "A Review of Techniques for Processing Ultra-High Modulus Polymers," Polym. Eng. and Sci., 16, 725 (1976).

19. P. J. Barham and A. Keller, "A Study on the Achievement of High-Modulus Polyethylene Fibers by Drawing," J. Mater. Sci., 11, 27 (1976).

20. J. M. Andrews and I. M. Ward, "The Cold Drawing of High Density Polyethylene," J. Mater. Sci., 5, 411 (1970).

21. G. Capaccio and I. M. Ward. "Ultra-High-Modulus Linear Polyethylene Through Controlled Molecular Weight and Drawing," Polym. Eng. and Sci., 15, 219 (1975).

22. D. Meier and Jarecki, "Ultrahigh Modulus Polyethylene, III. Effect of Drawing Temperature on Void Formation and Modulus," J. Polym. Sci., Polym. Phys. Edn., 17, 1611 (1979).

23. J. Clements, R. Jakeways and I. M. Ward, "Lattice Modulus and Crystallite Thickness Measurements in Ultra-high Modulus Linear Polyethylene," Polymer, 19, 639 (1978).

24. C. J. Frye, I. M. Ward, M. G. Dobb and D. J. Johnson, "Direct Measurement of Crystallite Size Distribution in Ultra-High Modulus Polyethylene," Polymer, 20, 1310 (1979).

25. R. G. C. Arridge, P. J. Barham and A. Keller, "Self-Hardening of Highly Oriented Polyethylene," J. Polym. Sci., C15, 389 (1977).

26. J. Clements, R. Jakeways and I. M. Ward, "A Study of the Effects of Annealing on the Mechanical Stiffness and Structure of Ultra-high Modulus Linear Polyethylene," Polymer, 20, 295 (1979).

27. T. Kanamoto, E. S. Sherman and R. S. Porter, "Extrusion of Polyethylene Single Crystals," Polymer Journal, 11, 497 (1979).

28. T. Kanamoto, A. E. Zachariades and R. S. Porter, "Deformation Profiles in Solid State Extrusion of High Density Polyethylene, 11, Polymer Journal, 307 (1979).

29. N. Capiati, S. Kojima, W. Perkins, and R. S. Porter, "Preparation of an Ultra-Oriented Polyethylene Morphology," J. Mater. Sci., 12, 334 (1977).

30. G. Capaccio, A. G. Gibson and I. M. Ward, "Drawing and Hydrostatic Extrusion of Ultra-High Modulus Polymers," Ultra high Modulus Polymers, A. Ciferri and I. M. Ward, Eds., Appl. Sci. Publishers, Ltd., England (1978).

31. K. Imada, T. Yamamoto, K. Shigematsu and M. Takayanagi, "Crystal Orientation and Some Properties of Solid-State Extrudate of Linear Polyethylene," J. Mater. Sci., 6, 537 (1971).

32. K. Nakayama and H. Kanetsuna, "Hydrostatic Extrusion of Solid Polymers, Part 5, Structure and Molecular Orientation of Extruded Polyethylene," J. Mater. Sci., 10, 1105 (1975).

33. Ibid., "Plastic Deformation of High Density Polyethylene During Hydrostatic Extrusion," J. Mater. Sci., 12, 1477 (1977).

34. R. S. Stein, "The X-Ray Diffraction, Birefringence, and Infrared Dichroism of Stretched Polyethylene. II. Generalized Uniaxial Crystal Orientation," J. Polym. Sci., 31, 327 (1958).

35. A. E. Zachariades, W. R. Mead and R. S. Porter, "Recent Developments in Ultramolecular Orientation of Polyethylene by Solid State Extrusion," Ultra-High Modulus Polymers, A. Ciferri and I. M. Ward, Eds., Appl. Sci. Publishers, Ltd., England (1978).

36. E. S. Clark and L. S. Scott, "Superdrawn Crystalline Polymers: A New Class of High-Strength Fiber," Polym. Eng. and Sci., 14, 682 (1974).

37. M. P. C. Watts, A. E. Zachariades and R. S. Porter, "Shrinkage as a Measure of the Deformation Efficiency of Ultra-Oriented High Density Polyethylene," to be published, J. Mater. Sci.

38. N. E. Weeks, S. Mori and R. S. Porter, "Morphology of Ultradrawn Polyethylene, 1. Nitric Acid Etching Plus Gel Permeation Chromatography," J. Polym. Sci., Polym. Phys., 13, 2031 (1975).

39. R. S. Porter, N. E. Weeks, N. J. Capiati and R. J. Krzewki, "Concerning the Negative Thermal Expansion for Extended Chain Polyethylene," J. Therm. Anal., 8, 547 (1975).

40. N. J. Capiati and R. S. Porter, "Dimensional Changes in Ultradrawn Polyethylene," J. Polym. Sci., C15, 1427 (1977).

41. A. Peterlin and R. Corneliussen, "Small-Angle X-Ray Diffraction Studies of Plastically Deformed Polyethylene. II. Influence of Draw Temperature, Draw Ratio, Annealing Temperature and Time," J. Poly. Sci., A-2, 6, 1273 (1968).

42. G. R. Strobl and N. Muller, "Small-Angle X-Ray Scattering Experiments for Investigating the Validity of the Two-Phase Model," J. Polym. Sci., Polym. Phys. Ed., 11, 1219 (1973).

43. W. Wu, P. G. Simpson, and W. B. Black, "Morphology and Tensile Property Relations of High Strength/High-Modulus Polyethylene Fiber," J. Polym. Sci., Polym. Phys. Edn., 18, 751 (1980).

44. R. J. Matyi and B. Crist, "Small-Angle X-Ray Scattering by Poly(ethylene Terephthalate) Fibers, J. Macromol. Sci.-Phys., B16(1) 15, 1979.

45. R. J. Matyi and B. Crist, "Small-Angle X-Ray Scattering by Nylon 6," J. Poly. Sci., Polym. Phys. Edn., 16 1329 (1978).

46. A.E. Zachariades, P.D. Griswold and R.S. Porter, "Ultra-drawing of Thermoplastics by Solid State Coextrusion Illustrated with High Density Polyethylene," Polym. Eng. and Sci., 19, 441 (1979).

47. B. Ke, "Characterization of Polyolefins by Differential Thermal Analysis," J. Polym. Sci., 42, 15 (1960).

48. D.C. Bassett, "Surface Detachment from Polyethylene Crystals" Phil. Mag., 6, 103 (1961).

49. P. Geil, in Polymer Single Crystals, Wiley Interscience, New York, 1963.

50. R.P. Palmer and A.J. Cobbold, "The Texture of Melt Crystallized Polyethylene as Revealed by Selective Oxidation," Makromol. Chem., 74, 174 (1964).

51. A. Keller and R.J. Willmouth, "Lattice Orientation Within Strirring Induced Crystals of Polyethylene", Macromol. Sci., (Phys.), B6, 539 (1972).

52. D. Grubb, "Review, Radiation Damage and Electron Microscopy of Organic Polymers," J. Mater. Sci., 9, 1715 (1974).

53. E.L. Thomas, S.L. Sass and E.J. Kramer, "Diffraction Contrast Study of the Defect Structure of Polyethylene Single Crystals," Phil. Mag., 30, 335 (1974).

54. B.J. Spit, "Gold Decoration Applied to Polymers," J. Macromol. Sci-Phys., B2, 45 (1968).

55. K. Shimamura, "Electron Microscopical Investigation of Internal Structure of Polyethylene Fibers," J. Macromol.. Sci.-Phys., B16(2), 213 (1979).

56. H. Hoehn, R.C. Ferguson and R.R. Hebert, "Effect of Molecular Weight on High Pressure Crystallization of Linear Polyethylene. I. Kinetics and Gross Morphology," Polym. Eng. Sci., 18, 457 (1978).

57. R.W. Hendricks, "The ORNL 10-meter Small-Angle X-Ray Scattering Camera," J. Appl. Cryst., 11, 15 (1978).

58. V. Luzzati, "Interpretation des Mesures Absolues de Diffusion Centrale des Rayons X en Collimation Ponctuelle ou Lineaire: Solutions de Particules Globulaires et de Batonnets," Acta Cryst., 13, 939 (1960).

59. P.H. Hermans and A. Weidinger, "Absolute Measurements of X-Ray Scattering at Low Angles in Crystalline Polymers," Makromol. Chem., 39, 67 (1960).

60. W.A. Rachinger, "A Correction for the $\alpha_1\alpha_2$ Doublet in the Measurement of Widths of X-ray Diffraction Lines," J. Sci. Instrum., 25, 254 (1948).

61. H.P. Klug and L.E. Alexander, X-Ray Diffraction Procedures for Polycrystalline and Amorphous Materials, John Wiley and Sons, London (1974).

62. A.R. Stokes and A.J.C. Wilson, "A Method of Calculating the Integral Breadths of Debye-Scherrer Lines: Generalization to Non-Cubic Crystals," Proc. Camb. Phil. Soc., 40, 197 (1944).

63. A.W. Agar, F.C. Frank and A. Keller, "Crystallinity Effects in the Electron Microscopy of Polyethylene," Phil. Mag., 4, 32 (1959).

64. E.L. Thomas and D.G. Ast, "Image Intensification and the Electron Microscopy of Radiation Sensitive Polymers," Polymer, 15, 37 (1974).

65. J. Langmore, J. Wall and M.S. Issacson, "The Collection of Scattered Electrons in Dark Field Electron Microscopy," Optik, 38, 335 (1973).

66. M.G.R. Thomson, "Resolution and Contrast in the Conventional and the Scanning High Resolution Transmission Electron Microscopes," Optik, 39, 15 (1973).

67. A. Engel, J. DuBouchet and E. Kellenberger, "Low Dose Scanning Transmission Electron Microscopy of Biological Specimens," Scanning Electron Microscopy Proceedings (I.I.T. Research Institute, Chicago), Vol. 1, 377 (1977).

68. J.M. Cowley and A.Y. Au, "Image Signals and Detector Configurations for STEM," Scanning Electron Microscopy Proceedings," (I.T.T. Research Institute, Chicago), Vol. 1, 53 (1978).

69. A. Rose, "Phase Contrast in Scanning Transmission Electron Microscopy," Optik, 39, 416 (1979).

70. L.E. Thomas, D.J. Humphreys, W.R. Duff and D.T. Grubb, "The Diffraction Dependence of Electron Damage in a High Voltage Electron Microscope," Rad. Eff., 3. 89 (1971).

71. D.T. Grubb and G.W. Groves, "Rate of Damage of Polymer Crystals in the Electron Microscope: Dependence on Temperature and Beam Voltage," Phil. Mag., 24, 815 (1971).

72. E.L. Thomas and S.L. Sass, "On the Orthorhombic to Hexangonal Phase Transformation in Polyethylene Single Crystals," Makromol. Chem., 164, 333 (1973).

73. A. Rose, "Television Pickup Tubes and the Problem of Vision," Adv. Electron., 1, 131 (1948).

74. M. Isaacson, D. Johnson and A.V. Crewe, "Electron Beam Excitation and Damage of Biological Molecules. Its Implications for Specimen Damage in Electron Microscopy," Radiat. Res., 55, 205 (1973).

75. A. Agar, "The Measurement of the Thickness of Thin Carbon Films," Brit. J. Appl. Phys., 8, 410 (1957).

76. K.H. Herrmann, D. Krahl and V. Rindfleish, "Use of TV Image Intensifiers in Electron Microscopy," Siemens Forsch. Entwickl. Ber., 1, 167 (1972).

77. A. Low, D. Vesley, P. Allan and M. Bevis, "An Investigation of the Microstructure and Mechanical Properties of High Density Polyethylene Spherulites," J. Mater. Sci., 13, 711 (1978).

78. R.H. Geiss, "STEM Electron Diffraction from 30Å Diameter Areas," Developments in Electron Microscopy and Analysis, ed. J.A. Venables, Academic Press, New York, (1976).

79. K. Kobayashi and K. Sakaoku, "Irradiation Changes in Organic Polymers at Various Accelerating Voltages," Lab. Invest., 14, 1097 (1965).

80. Y. Talmon and E.L. Thomas, "Temperature Rise and Sublimation of Water From Thin Frozen Hydrated Specimens in Cold Stage Microscopy," Scanning Electron Microscopy Proceedings (I.I.T. Research Institute, Chicago), Vol. 1, 265 (1977).

81. W. Kossel and G. Molenstadt, "Elektroneninterferenzen im Konvergenten Bundel," Ann. Physik, 36, 113 (1939).

82. E.L. Thomas, "Diffraction Contrast of Fold Domain Boundaries in Polyethylene Single Crystals," J. Mat. Sci., 12, 234 (1977).

83. E.L. Thomas, "Electron Microscopy of Radiation Sensitive Polyethylene Crystals," Developments in Electron Microscopy and Analysis, ed. J.A. Venables, Academic Press, New York (1976).

84. H.D. Keith, F.J. Padden and R.G. Vadimsky, "Intercrystalline Links: A Critical Evaluation," J. Appl. Phys., 42, 4585 (1971).

85. M.P.C. Watts, A. Zachariades, R.S. Porter, and R. Farris, to be published.

86. A. Zachariades, Personal Communication.

87. J.R. White, "Bending Contribution to Line-Broadening in Polymer Diffraction," J. Polym. Sci., Polym. Phys. Ed., 16, 387 (1978).

88. A. Schonfeld and W. Wilke, "Determination of crystallite size and lattice distortions in extended chain polyethylene and their change after oxydative degeneration," Kolloid Z.-Z. Polym., 250, 496 (1972).

89. A. Zwijnenburg, P.F. van Hutten, A.J. Pennings and H.D. Chanzy, "Longitudinal Growth of Polymer Crystals from Flowing Solutions, V. Structure and Morphology of Fibrillar Polyethylene Crystals," Colloid and Polym. Sci., 256, 729 (1978).

90. E.W. Fischer and G.F. Schmidt, "Long Periods in Drawn Polyethylene," Angew. Chem. Int. Ed., 1, 488 (1962).

91. R. Corneliussen and A. Peterlin, "The Influence of Temperature on the Plastic Deformation of Polyethylene," Makromol. Chem., 105, 193 (1967).

92. E.W. Fischer, H. Goddar and G.F. Schmidt, "Röntgenkleinwinkeluntersuchungen zur Struktur der fehlgeordneten Bereiche in verstreckten Polyäthylen," Makromol. Chem., 118, 144 (1968).

93. E.W. FIscher, H. Goddar and G.F. Schmidt, "Determination of Degree of Crystallinity of Drawn Polymers by Means of Density Measurements," J. Polym. Sci., A-2, 7, 37 (1969).

94. P. Zugenmaier and H.J. Cantow, "Ein einfaches Verfahren zur Indizierung von Rontgenweitwinkel-Reflexen von Substanzen mit Orthorhombischer Elementarzelle," Kolloid Z.-Z. Polym., 230, 229 (1969).

95. G. Porod, "Die Rontgenkleinwinkelstreuvng von dichtgepackten Kolloiden Systemen," Kolloid Z.-Z. 124(2), 83 (1951).

96. B. Crist, "Small-Angle X-Ray Scattering of Semicrystalline Polymers. I. Review of Existing Models," J. Polym. Sci., Polym. Phys. Edn., 2, 635 (1973).

97. B. Crist, "Microfibril Dimensions from Small-Angle X-Ray Scattering," J. Appl. Cryst. 12, 27 (1979).

98. S. Krimm and A.V. Tobolsky, "Quantitative X-ray Studies of order in amorphous and crystalline polymers. Scattering from various polymers and a study of the glass transition in polystyrene and polymethylmethacrylate," Textile Res. J., 21, 805 (1951).

99. M.G. Dobb, D.J. Johnson, A. Majeed and B.P. Saville, "Microvoids in Aramid-type fibrous polymers," Polymer, 20, 1284 (1979).

APPENDIX I

RESIDENCE TIME DURING SOLID STATE EXTRUSION

The residence time, τ, for polymer to pass from position a to b in the conical die (see Figure 1.5) is:

$$\tau = \int_{a}^{b} d\tau = \int_{x=a}^{x=b} dx/V(x) \qquad (1)$$

where V(x) is the velocity. Assuming non-compressive volumetric flow:

$$V(x)R^2(x) = V_t r^2 \qquad (2)$$

where V_t is the velocity at the die exit (extrusion rate). For a die of entrance diameter Ra and semi-angle θ,

$$R(x) = Ra - x \tan \theta \qquad (3)$$

$$EDR(x) = \left(\frac{Ra}{R(x)}\right)^2 = \frac{Ra^2}{(Ra - x \tan \theta)^2} \qquad (4)$$

$$\tau = \int_{x=a}^{x=b} \frac{R^2(x)\, dx}{V_t r^2}$$

$$= \frac{1}{-3V_t r^2 \tan \theta} \left[(Ra - x \tan \theta)\right]_{x=a}^{x=b} \qquad (5)$$

Using equation (4), τ can be expressed in terms of limits of extrusion draw ratio:

$$\tau = \frac{Ra^3}{-3V_t r^2 \tan\theta} \left[\frac{1}{EDR(x)^{3/2}} \right]_{EDR_a}^{EDR_b} \qquad (6)$$

for the 9X die, $2\theta = 20°$, $L = 12.5$ mm, $V_t = 18$ mm/min.

$$\tau = \frac{79.1}{V_t} \left(\frac{1}{1^{3/2}} - \frac{1}{9^{3/2}} \right) + \frac{L}{V_t}$$

$$= 4.39 + 69.4 = 5.08 \text{ minutes.}$$

APPENDIX II

INVARIANT COMPUTER PROGRAM

```
$NOP
$EXE SED

*C MODCOMP SOURCE EDITOR       DATE  08/01/80  09:03:31        PAGE   1

ASS SI USL
POS UMASS
LALL
LIST

*C MODCOMP SOURCE EDITOR       DATE  08/01/80  09:03:31        PAGE   1
```

```
 1        PROGRAM UMASS
 2  C *** PROGRAM TO CALCULATE THE INTEGRATED INTENSITY FOR A
 3  C *** TWO POINT SAXS PATTERN.
 4  C ***
 5  C *** VERSION A.02 AUGUST 1,1980   ***********
 6        DIMENSION IDATA(64,64),DAT(64,64)
 7        REAL MR,IO,LAMBDA,MK1,MK2
 8        INTEGER ANS(3),HEDREC(100)
 9        COMMON/DATA/IDUM1,IDUM2,MM,NN,IDATA
10        COMMON/HEADER/HEDREC
11        COMMON/MANAGE/MAXREC,MXWRDS,LU,IDEM
12        EQUIVALENCE (CPM,HEDREC(60)),(TM,HEDREC(52)),(DIST2,HEDREC(62))
13        EQUIVALENCE (CX,HEDREC(42)),(CY,HEDREC(44))
14        EQUIVALENCE (TIME,HEDREC(36))
15        DEFINE FILE 21(4480,200,L,NXTREC)
16        LU = 21
17        MAXREC = 4480
18        MXWRDS = 100
19        IDEM = 4100
20        PI = 4.0*ATAN(1.0)
21        LAMBDA = 1.5417E-08
22        ECONST = 7.94E-26
23        WRITE(6,10)
24     10 FORMAT(' ENTER DATA SET SEQUENCE NO. (16)')
25        READ(5,11) ISEQ
26     11 FORMAT(I6)
27        NERR = 0
28        CALL FETCH(ISEQ,NERR)
29        IF(NERR .EQ. 0) GO TO 20
30        GO TO 10
```

```
      20 WRITE(6,800) (HEDREC(I)
  800 FORMAT(1H ,' INVARIANT MOMENTS FOR ',15A7)
      WRITE(6,900) (HEDREC(I),I =1,10)
  900 FORMAT(10X,' TITLE : ',20A2)
      WRITE(6,12) IM,CPM,DIST2,LX,LY
   12 FORMAT(1H ,' THE SAMPLE TRANSMISSION = ',F8.3/
     X' THE CHANNELS PER MM = ',F8.3/
     X' THE SAMPLE-DETECTOR DISTANCE = ',F8.1/
     X' THE CENTER OF PATTERN : X = ',F8.2/
     X'                         Y = ',F8.2)
      WRITE(6,15)
   15 FORMAT(1H ,' ENTER SPECIMEN THICKNESS IN CM(F8.2) ')
      READ(5,30) TS
   30 FORMAT(F8.2)
      WRITE(6,55)
   55 FORMAT(1H ,' ENTER THE INCIDENT INTENSITY IN CPS(E8.3)')
      READ(5,60) IO
   60 FORMAT(E8.3)
      WRITE(6,62)
   62 FORMAT(1H ,' ENTER THE CENTER OF THE PATTERN: CX & CY(2F8.3)')
      READ(5,70) CX,CY
      WRITE(6,65)
   65 FORMAT(1H ,' ENTER ORIGIN LIMITS IN MRAD IN X- & Y-DIR.(2F8.3)')
      READ(5,70) MR1,MR2
   70 FORMAT(2F8.3)
      WRITE(6,80)
   80 FORMAT(1H ,' ENTER THE BACKGROUND TDS COUNTS')
      READ(5,81) B
   81 FORMAT(F5.2)
      MR = 1000.0/(CPM*DIST2)
      DS = 1.0/(CPM*LAMBDA*DIST2)
      SUM = 0.0
      TOTAL = 0.0
      MM = 64
      NN = 64
      DO 290 J= 1,NN
      DO 280 I = 1,MM
      X = FLOAT(I)
      Y = FLOAT(J)
      X1 = ABS(MR*(CX    X))
      Y1 = MR*(CY - Y)
```

```
72          IF(ABS(XI) .LE. MKI .AND. ABS(YI) .LE.  0K. ) GO TO 280
73          THETA = SQRT(XI**2 + YI**2)/1000.0
74          DAT(I,J) = FLOAT(IDATA(I,J))    E
75          IF(DAT(I,J) .LE. 0.0) DAT(I,J)    0.0
76          S = 2.0*SIN(THETA)/LAMBDA
77          SINA = SIN(ATAN(ABS(YI/XI)))
78          SUM    SUM + (DAT(I,J)*XI*(DS**2)/(LAMBDA*1000.))
79          IDTAL  = IDTAL + IDATA(I,J)
80      280 CONTINUE
81      290 CONTINUE
82          WRITE(6,300)
83      300 FORMAT(' DO YOU WANT TO DISPLAY ALL 4096 DATA POINTS?')
84          READ(5,350) ANS
85      350 FORMAT(3A1)
86          IF(ANS(1) .EQ. 'Y') GO TO 920
87          IF(ANS(1) .EQ. 'N') GO TO 940
88      920 WRITE(6,950) ((IDATA(I,J),I=1,MM),J=1,NN)
89      950 FORMAT(10(2X,I8))
90      940 WRITE(6,910) TOTAL
91      910 FORMAT(' THE TOTAL = ',E15.6)
92          Q = 3.13E-18*SUM/(10*TIME*TM*(IS**2))
93          WRITE(6,1000) Q
94     1000 FORMAT(1H ,' THE INVARIANT Q = ',E15.4,' DMS**2/CM**6')
95          STOP
96          END
EXIT
$AVR C1 4
$END DO
$
```

APPENDIX III

VOID SCATTERING

It is possible to estimate the void volume fraction, ϕ_v, by combining the two and three phase models. For the two phase model:

$$Q = (\rho_c - \rho_a)^2 \phi(1 - \phi) \tag{1}$$

where Q is calculated by equation 2.2 neglecting the void and zero order scattering at the origin. For the three phase model:

$$Q' = (\rho_c - \rho_a)^2 \phi_c \phi_a + (\rho_c - \rho_v)\phi_c \phi_v + (\rho_a - \rho_v)^2 \phi_a \phi_v \tag{2}$$

where $\rho_v = 0$ and Q' is calculated including the void scattering. Since

$$\Delta Q = Q' - Q, \tag{3}$$

combining equations (1), (2) and (3) yields

$$\phi_v = \frac{\Delta Q}{\rho_c^2 \phi_c + \rho_a^2 \phi_a} \tag{4}$$

Since the void fraction is small we can assume:

$$\phi_c \simeq \phi \tag{5}$$

$$\phi_a \simeq 1 - \phi \tag{6}$$

Since $Q' \simeq 1.1Q$ for most of the samples, ΔQ, and hence ϕ_v, is highest for the cold drawn sample ($Q = 9.6 \times 10^{-5}$). Combining equations (4), (5), and (6) and using the values in Tables 6.1 and 6.2 gives a value of 1×10^{-5} for the void volume fraction. This very low value for the cold drawn sample is an upper bound and indicates that the assumptions of equations (5) and (6) are valid. Therefore the void concentrations in these samples are very small and do not affect the density measurements and invariant calculations.